Karlsruhe Institute of Technology

Multiscale modelling of mesoscopic behaviour in soft matter systems

Zur Erlangung des akademischen Grades eines

Doktors der Naturwissenschaften (Dr. rer. nat.)

von der KIT-Fakultät für Physik
des Karlsruher Instituts für Technologie (KIT)

angenommene
Dissertation

von

M.Sc. Ka Chun Chan

Tag der mündlichen Prüfung: 21.07.2023
Referent: Prof. Dr. Wolfgang Wenzel
Korreferent: Prof. Dr. Jörg Schmalian

Abstract

Soft matter modelling has a wide range of applications, such as polymer additive manufacturing, organics electronics, and biomolecular engineering. Many physical properties and phenomena of soft matter are determined by interactions and processes at a wide range of length and time scales. Therefore, it is challenging for theoretical models to simulate processes involving features from multiple scales. To reach the mesoscopic scales for soft matter behaviour, coarse-grained models have been developed to accelerate the atomistic models by projecting out the relevant degrees of freedom, allowing coverage of a wider range of scales. However, due to the lack of a formalism to capture the dynamics and anisotropy of the system, conventional coarse-grained model shows significant errors in dynamical properties and inconsistent soft matter behaviour.

In this thesis, a generalised systematic formalism for coarse-graining is presented. The Mori-Zwanzig formalism provides a dynamically-guided projection to construct a mesoscopic system directly from the underlying microscopic system. Moreover, the Gay-Berne functional is introduced to describe the anisotropic effect of the pairwise interactions at mesoscopic level. The performance of the model is demonstrated by comparing it to other coarse-grained models using benzene as an example, which shows significant improvement in both static and dynamical properties. For application, crystallization of pentacene is studied by treating pentacene molecule as ellipsoidal particle. Furthermore, a modified atomistic model and a modified continuum model are employed to simulate mesosopic behaviour of polymers in electrospinning and electro-optical poling, demonstrating mesoscopic modelling from the atomistic and continuum limits.

Contents

1. Introduction

Soft condensed matter is indispensable and ubiquitous in our daily life. Polymers, colloids, liquid crystals, and other materials that are structurally altered by thermal or mechanical energy in the magnitude of thermal fluctuations are all considered to be soft matter[1]. Soft matter has recently been the basis for many novel technological developments, including 3d printing[2], organic electronics[3], chip fabrication[4], and biomedical applications[5]. The main feature that sets soft matter apart from conventional condensed matter is that it exhibits strong self-organizing properties, which involve processes over a wide range of scales in both length and time[6]. Soft matter behaviour, such as order-flow coupling in liquid crystals[7] and entanglement in polymer rheology[8], is originated by molecular interactions and exhibits phenomena on macroscopic lab scale. In order to study the behaviour of soft matter, access to the intermediate mesoscopic scale is necessary. However, it is challenging for theoretical models to simulate processes involving features from multiple scales.

In general, there are two main types of theoretical models for material simulations: particle-based models and grid-based models. Particle-based model is a model that tracks each particle individually through the simulation. One of the most prevalent particle-based models is molecular dynamics (MD)[9], in which each particle in the simulation corresponds to an atom. The interaction between particles is described by a forcefield[10, 11], which is typically extracted from the quantum mechanical calculations or experimental data. The particle-based model is effective for studying phenomena at the molecular level, but the computational cost increases drastically with the number of particles, making it infeasible to simulate systems beyond the microscopic scale. On the other hand, the grid-based models, also known as continuum models (CM)[12], divide the material space into many grid points with local material properties. The bulk material properties are described by continuous functions derived from physical laws. However, in continuum model, the

molecular interactions are neglected as it is assumed that each grid has a large number of atoms in thermal equilibrium.

To enable computational models accessible to the mesoscopic scale, the coarse-grained (CG) method[13, 14] has been developed by simplifying the atomistic details of MD simulations. As a result, the computational complexity is drastically reduced, making it feasible to simulate systems with larger length and time scales. The CG model has been applied to study macromolecular systems, such as protein folding[13, 15], complex polymer structure formation[16], and self-assembly of amino acids[17]. Additionally, different approaches have been developed to simulate the dynamical behaviour of various mesoscopic problems. For example, dissipative particle dynamics[18, 19] has been applied to study polymer melts[20] and red blood cells dynamics[21], multi-particle collision dynamics [22, 23] is employed to simulate shear flow of star polymers[24], and lattice Boltzmann method[25] is used to model the flow in porous media[26]. Every model has unique features and limitations, particularly in terms of the spatio-temporal scale. Therefore, selecting the right model for a specific problem necessitates knowledge of both the model and the system of interest.

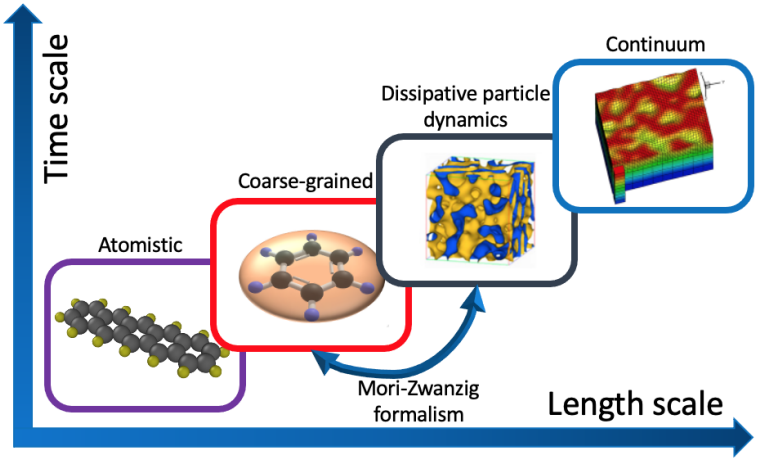

Figure 1.1.: Schematic diagram of theoretical models in a multiscale hierarchy.

1.1. Objective of the thesis

The objective of this thesis is to develop a computational model for the simulations of various mesoscopic phenomena in soft matter. The length- and time-scale of different models are shown in fig.(1.1), where the atomistic model operates on microscopic scale (10^{-9}m - 10^{-7}m) and the continuum model operates on macroscopic scale (>10^{-5}m). Mesoscopic models, such as the coarse-grained (CG) approach and dissipative particle dynamics (DPD), enable the simulations of the intermediate mesoscopic scale, which lies between the micro- and macro-scopic scales. The CG model and the DPD model are both particle-based models employing a pseudo particle approach, but they are derived from different theoretical backgrounds: the CG model is constructed from the microscopic model by eliminating irrelevant degrees of freedom[13], whereas the DPD model considers fluid elements as particles to relate the macroscopic non-Newtonian flow properties of fluids[19]. As a result, they are applied to different mesoscopic problems. For example, the CG model is employed to study macromolecular systems, such as protein folding[15], and the DPD model is used to study the dynamics of polymer solutions, i.e. rheology[27]. However, due to the lack of a general formalism of coarse-graining, both models show deficiencies in mesoscopic modelling, in which the CG model shows significant errors in long-time dynamical properties, and the DPD model lacks the chemical descriptions of the systems[28].

The Mori-Zwanzig(MZ) formalism[29, 30] is an order reduction technique for theoretical models that provides a systematic formalism for performing coarse-graining. Based on the framework of the DPD model, the MZ formalism projects out the collective variables and maps the dynamics of the atomistic system to a mesoscopic system[31]. As a result, the MZ formalism bridges the gap between the CG model and the DPD model and inherits the features of both models, in which the chemical descriptions of the atomistic system are captured and the dynamical properties are consistently reproduced.

In this thesis, the formulation of the MZ approach for the DPD model is presented, where the forcefield is constructed from the underlying atomistic model. One key result of this work is the development of an anisotropic DPD model via the MZ formalism (AMZDPD). While most CG models use a spherical representation, many molecules, especially those with ring structures, cannot be accurately approximated by a sphere. In order to better approximate the geometric shape of atomic clusters in coarse-graining, the

Gay-Berne potential was developed to describe non-spherical clusters using an ellipsoidal representation [32, 33]. The AMZDPD model presented here employs the ellipsoidal representation and follows the MZ formalism, resulting in a significant improvement in the dynamical properties. In addition, the AMZDPD model is applied to model the crystallization of pentacene in this work. Crystallization of organic molecules is a mesoscopic process in which molecules spontaneously form ordered aggregates via self-assembly[34]. It is an important process for fabricating high-quality organic thin films in organic electronics[35]. By using the AMZDPD model, the pentacene molecules self-assemble to form brick-wall structure at the CG level, demonstrating its ability to simulate mesoscopic behaviour in soft matter.

Apart from the AMZDPD model, two other models, i.e. the atomistic MD and the continuum model, are presented to simulate two other mesoscopic phenomena in this thesis: 1) In the 3d printing with electrospinning approach, the deposition of nanofiber is determined by the charge dissipation inside polymer[36]. To study the underlying mechanism of the electrospinning fiber deposition, a trapped state of charge carrier is introduced to the continuum model in order to simulate the deposition behaviour of charged polymeric fiber during electrospinning. 2) Poling is a process to align the dipolar functional groups and activate the non-linear optical effect of the electro-optical (EO) materials in chip fabrication for optical devices[37]. A virtual system, where the polymer chain is divided into oligomers and functional sidechains, is employed to study the poling process using atomistic MD simulations.

1.2. Outline of the thesis

Mesoscopic modelling is a challenging topic in material modelling as it needs to describe features from multiple scales, ranging from the molecular to the macroscopic level. Even with the most powerful computer, the explanation of mesoscopic phenomena by quantum mechanics or macroscopic laws is restricted due to the constraints of theoretical models. As a result, mesoscopic schemes are essential for overcoming the barrier of accessing the complex intermediate mesoscopic scale. With the development of these schemes, the mesoscopic models can be applied to and facilitate advancements in a wide range of fields. To present a comprehensive study of mesoscopic modelling, this thesis is organized as follows:

- **Chapter(2)** briefly introduces the theoretical foundations of different computational models used in material simulations, including the atomistic molecular dynamics, coarse-grained model, dissipative particle dynamics, and continuum model. The technical aspects, features, and limitations of these models are discussed to provide a general overview for mesoscopic modelling.
- **Chapter(3)** presents a detailed formulation of a dynamically consistent coarse-grained approach for mesoscopic modelling. This chapter introduces the Mori-Zwanzig formalism for coarse-graining a molecular system and provides a detailed parameterization procedure for constructing an anisotropic mesoscopic forcefield using benzene as an example. A comparison between the AMZDPD model and other CG models in terms of static and dynamical properties is also presented, demonstrating the performance of the AMZDPD model in mesoscopic modelling.
- **Chapter(4)** presents three different examples of the mesoscopic schemes applied to soft matter phenomena. The first example studies the crystallization of pentacene using the AMZDPD model in order to investigate its ability in mesosocpic modelling by simulating the crystallization process with anisotropic particles. The second example investigates the charged fiber deposition in electrospinning using the continuum model, revealing how residue charges in polymer determine the mechanical behaviour of the fiber deposition. The third example employs the atomistic MD to study the poling process in EO materials, examining the effects of linkers, poling temperature, and poling field on poling. With these three examples, this chapter demonstrates how mesoscopic modelling assists in material research.
- **Chapter(5)** summarizes the mesoscopic simulations for soft matter and provides an outlook on the development of mesoscopic modelling.

2. Theoretical Background

Many material phenomena, particularly in soft matter, exhibit important features at multiple scales in space and time. However, each model operates at a different scale. To enable modelling of phenomena at multiple scales, multiscale modelling is developed to bridge the gap between models with different scales. A typical method for connecting models is to parameterize one model using another, as presented in fig.(2.1). When a model is parameterized by a lower resolution model, this is called the "top-down" approach. On the contrary, when a model is parameterized by a higher resolution model, this is known as the "bottom-up" approach. As a result, the model can inherit features from the connecting model through model parameterization.

In this chapter, the fundamental concepts of theoretical models for material modelling at different scales are introduced in ascending order, as shown in

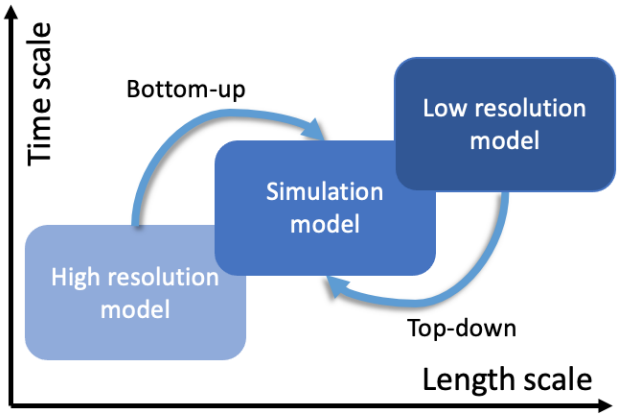

Figure 2.1.: Multiscale modelling connects models at different scales via parameterization of the "top-down" and "bottom-up" approach.

fig.(1.1). First, the principles of molecular dynamics, which models materials at the microscopic scale, are presented in sec.(2.1). Then, the coarse-grained model and the dissipative particle dynamics, both operating at the mesoscopic scale, are introduced in sec.(2.2) and sec.(2.3). Finally, sec.(2.4) gives a brief introduction to the grid-based continuum model at the macroscopic scale.

2.1. Atomistic Molecular Dynamics

Molecular dynamics (MD) is one of the most influential computational tools in modern science[9, 38, 39]. Based on the insights from quantum mechanics and statistical mechanics, MD simplifies the complicated, expensive, or even unsolvable computations for complex systems into a set of simple classical Newton's equations, allowing for analysis of atomic and molecular movements. The development of MD enables the study of structural, chemical, and physical properties of molecular systems and accelerates the advancement of various fields, including biology[40], chemistry[41], material science[42].

Since the twentieth century the development of quantum mechanics has explained the problem of many-body interactions[43], where an N-body system can be described probabilistically using the Schrödinger equation

$$i\hbar\frac{\partial\boldsymbol{\psi}}{\partial t} = \sum_{i}^{N}[-\frac{\hbar^2}{2m_i}\nabla^2 + U(\mathbf{r}_{i1}, \mathbf{r}_{i2} \dots \mathbf{r}_{iN})]\boldsymbol{\psi}, \tag{2.1}$$

where i is the imaginary unit, $\hbar$ is Planck's constant, m_i is the mass of particle i, $\boldsymbol{\psi}$ is the unknown wave function, and U is the atomic potential energy function with variable $\mathbf{r}_{ij}$ denotes the relative coordinates between particle i and j in the system. However, solving the many-body system is not easily achieved due to computational complexity. Even for a simple molecule like water, the basic description of the probability distribution for a water molecule is a complex-valued function of 39 variables in three-dimensional space.

Since the mass of the nucleus is much larger than the mass of the electron in an atom, the electronic timescale is much faster than the ionic timescale. Therefore, one can assume that the positions of the nuclei are fixed in an atomic system. This assumption is known as the Born-Oppenheimer approximation[44]. As a result, the ionic and electronic motions decouple, and the stationary electronic Schrödinger equation can be extracted. By solving the

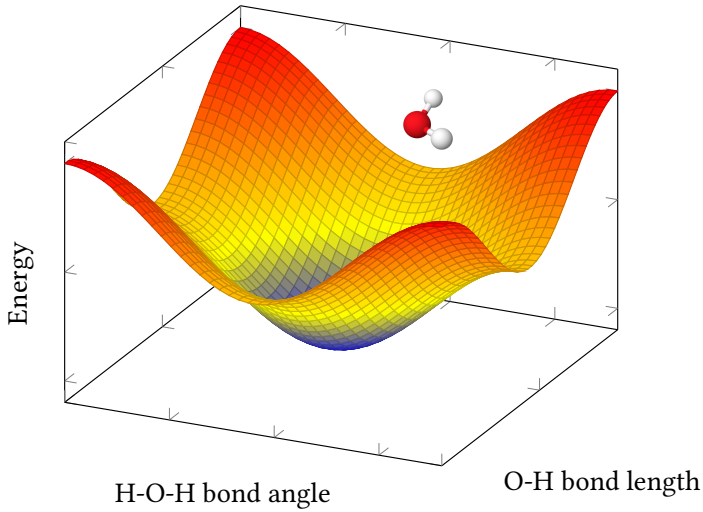

Figure 2.2.: Illustration of Born-Oppenheimer surface of a water molecule as a function of O-H bond length and H-O-H bond angle. The minimum energy, indicated by the blue region, corresponds to the optimized molecular structure with a bond length of 0.0958 nm and a bond angle of 104.5°.

static electronic structure problem, the potential energy landscape in terms of the nuclei positions can be obtained, which is also referred to as the Born-Oppenheimer surface, as shown in fig.(2.2). In the end, the Born-Oppenheimer surface can be utilized as the potential in the ionic Schrödinger equation to compute the dynamics of nuclei[45].

Nevertheless, solving the time-independent Schrödinger equation is still a challenging task. To further simplify the computations, the empirical forcefield method has been developed, which uses empirical models to represent the complex functional form of the Born-Oppenheimer surface. This method is known as Molecular Mechanics (MM)[46]. The interaction between atoms is approximated by an empirical forcefield[47, 48] which sums up the contributions of different interactions, such as pairs, triples and quadruples. As a result, the problem is converted from quantum mechanics to classical mechanics. Instead of solving the linear partial differential equation (the Schrödinger

equation), the time evolution of the molecular system is now described by ordinary differential equation (the Newtonian equation)

$$m\frac{d^2\mathbf{r}}{dt^2} = -\mathbf{F}(\mathbf{r}) = -\nabla U(\mathbf{r}), \tag{2.2}$$

where $\mathbf{F}(\mathbf{r})$ is the forcefield and $U(\mathbf{r})$ is the problem-specific interaction potential. For a specific molecule, the interaction potential can be divided into bonded and non-bonded interaction

$$U = U_{bonded} + U_{nonbonded}. \tag{2.3}$$

The non-bonded potential is given by the sum of the Coulomb potential and the Lennard-Jones potential between the atom i and j

$$U_{nonbonded} = \sum_{ij}(U_{ij}^{Coul} + U_{ij}^{LJ}). \tag{2.4}$$

The Coulomb potential is given by

$$U_{ij}^{Coul} = \frac{Q_iQ_j}{4\pi\epsilon_0|\mathbf{r}_{ij}|}, \tag{2.5}$$

where Q_i and Q_j are the partial charge on atom i and j, ϵ_0 is the vacuum permittivity, and $|\mathbf{r}_{ij}|$ is the separation between the atoms. The Lennard-Jones potential consists of a long-range attractive part and short-range repulsive part and is given by

$$U_{ij}^{LJ} = 4\epsilon_{ij}\left(\frac{\sigma_{ij}^{12}}{|\mathbf{r}_{ij}|^{12}} - \frac{\sigma_{ij}^{6}}{|\mathbf{r}_{ij}|^{6}}\right), \tag{2.6}$$

where ϵ_{ij} and σ_{ij} are the strength and range parameter to describe the interaction between atom i and j.

The bonded potential can be divided into 3 parts

$$U_{bonded} = \sum_{bonds} U_{bond} + \sum_{angles} U_{angle} + \sum_{dihedrals} U_{dihedral}, \tag{2.7}$$

which is given by the sum of the bond, angle and dihedral interactions, and they correspond to the intra-molecular 2-body, 3-body, and 4-body terms,

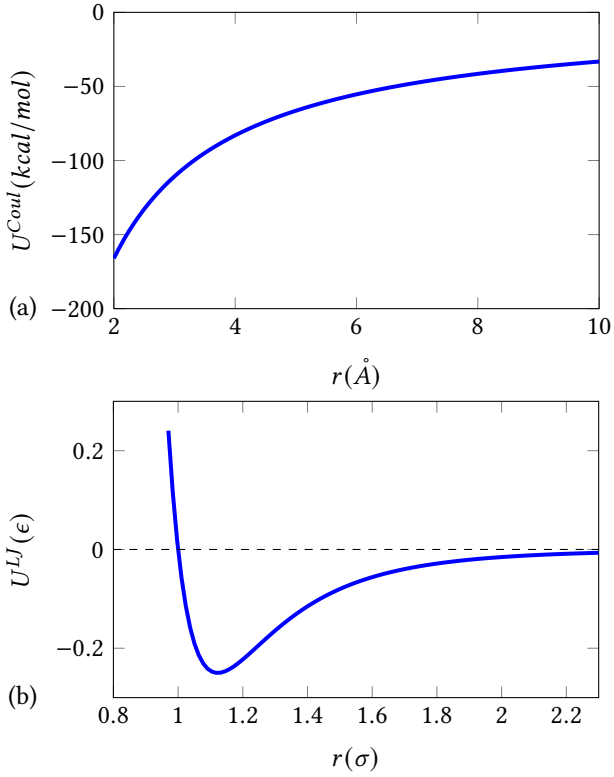

Figure 2.3.: Functional form of non-bonded forcefield contribution (a) Coulomb potential (b) Lennard-Jones potential

respectively. For the bond and angle potential, they are usually described by a harmonic form

$$U_{bond} = \frac{1}{2} k_b (r - r_0)^2, \tag{2.8}$$

where k_b is the force constant, r is the bond length, and r_0 is the equilibrium bond length.

$$U_{angle} = \frac{1}{2} k_\theta (\theta - \theta_0)^2, \tag{2.9}$$

where k_θ is the force constant, θ is the angle, and θ_0 is the equilibrium angle. The dihedral potential is usually given by a periodic function

$$U_{dihedral} = \frac{1}{2} k_\phi [1 + cos(n\phi + \gamma)], \tag{2.10}$$

where k_ϕ is the force constant, ϕ is the dihedral angle, n is a integer, and γ is the phase angle.

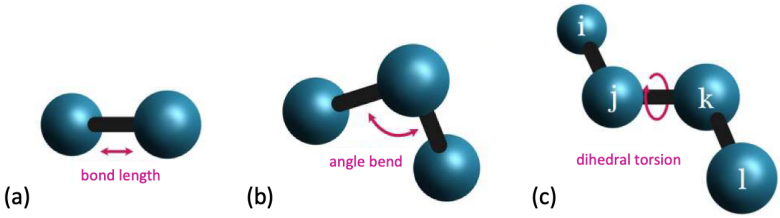

Figure 2.4.: Illustration of the bonded forcefield contribution (a) bond potential (b) angle potential (c) dihedral potential (adapted from [49] with permission from MDPI)

Once the problem-specific forcefield is obtained, the force acting on each individual particle can be computed. As a result, the Newton's equation for a set of atoms can be numerically solved to simulate the time evolution of the molecular system, know as Molecular Dynamics (MD). The implementation of MD relies on the discretization of the particle trajectories using a finite time step Δt. There are several numerical schemes available to solve the Newton's equation for MD, such as Euler scheme[50], Verlet leap frog scheme[51], and velocity-Verlet scheme[52]. In this work, the velocity-Verlet scheme is used due to its higher numerical precision and its ability to prevent round-off errors. For the integration in each time step, the coordinate and velocity of particle i, denotes as $\mathbf{r}_i(t + \Delta t)$ and $\mathbf{v}_i(t + \Delta t)$, are evaluated as follows:

$$\begin{aligned} \mathbf{r}_i(t + \Delta t) &= \mathbf{r}_i(t) + \mathbf{v}_i(t)\Delta t + \frac{1}{2}\mathbf{a}_i(t)\Delta t^2 \\ \mathbf{v}_i(t + \Delta t) &= \mathbf{v}_i(t) + \frac{1}{2}(\mathbf{a}_i(t) + \mathbf{a}_i(t + \Delta t))\Delta t, \end{aligned} \tag{2.11}$$

where $\mathbf{a}_i(t) = \frac{\mathbf{F}_i(t)}{m_i}$ is the acceleration of particle i computed from the forcefield. Moreover, the choice of timestep Δt is crucial in the simulation. A timestep that is too small wastes computational time without bringing the

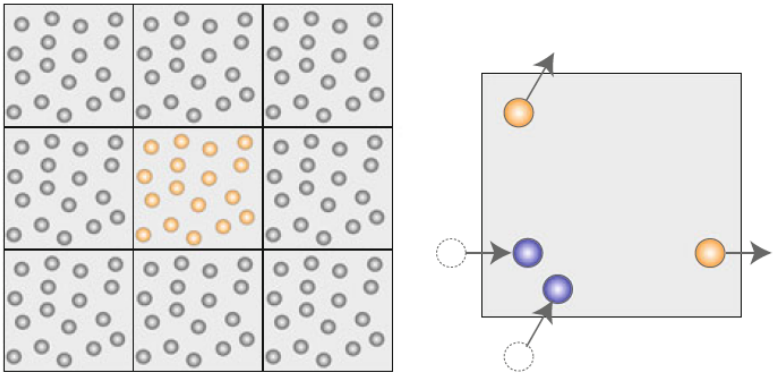

Figure 2.5.: Schematic diagram to illustrate the periodic boundary conditions, in which the left panel shows atoms of the central simulation cell are repeated in each neighboring cell, and the right panel shows an atom reenter via the opposite boundary when it leaves the central cell (reproduced from [54] with permission from the Springer Nature)

system to the desired state, while a timestep that is too large can lead to nonphysical results. The shortest timescale in the system, which is typically the frequency of bond vibration, determines the timestep for the MD simulation. A typical timestep of MD simulations usually falls in the range of femtoseconds.

The boundary conditions for the MD simulation should be carefully chosen based on the system of interest. For instance, periodic boundary conditions[53] are employed to study properties in the bulk phase by repeating the atoms of the central simulation cell to neigbouring cells, as in fig.(2.5). Due to the limitation of the particle number in MD simulations, periodic boundary conditions are realistic at replicating the behaviour of bulk system in experiment. On the other hand, fixed boundary conditions can be used to simulate interfaces by applying a refection potential at the boundary of the simulation cell.

The surrounding environment has a significant effect on the system of interest in MD simulation, so that it is treated as an extended system of MD, i.e. heat bath or a pressurizing medium. In order to include the effect of the extended system, different schemes for thermodynamic ensembles can be employed. The NVT and NPT ensembles, also known as the Nosé-Hoover thermostat[55,

56] and the Nosé-Hoover-Andersen barostat[57, 58], are two commonly used methods in MD simulations. In the NVT ensemble, the system is connected to an external degrees of freedom (the extended system), representing a heat bath to control the simulation temperature. The velocity of each individual atom is rescaled by subjecting to a frictional term. The scaling factor that rescales the atoms' velocities is defined as

$$\lambda_T(t) = \sqrt{1 + \frac{\Delta t}{\tau_T}(\frac{T_0}{T(t)} - 1)}, \tag{2.12}$$

where τ_T is the coupling parameter, $T(t)$ is the instantaneous temperature, and T_0 is the target temperature. In the NPT ensemble, the system is connected to an external degrees of freedom, representing a barostat to control the simulation pressure by adjusting the simulation box volume. The scaling factor $\lambda_P(t)$ that rescales the atoms' coordinates is defined as

$$\lambda_P(t) = [1 + \frac{\beta \Delta t}{\tau_P}(P_0 - P(t))]^{\frac{1}{3}}, \tag{2.13}$$

where τ_P is the coupling parameter, $P(t)$ is the instantaneous pressure, β is the isothermal compressibility , and P_0 is the target pressure.

The outline of a molecular dynamics code is presented in fig.(2.6). At each simulation timestep, the forces acting on each particle are computed based on the forcefield and the particles' current state. Additional information, such as the thermostat, barostat, and boundary conditions, can be introduced into the MD computation to correct the coordinates and velocities of particles. The coordinates and velocities are then updated for the next timestep by solving the Newton's equation. This routine is repeated until the final state of the system or the final timestep is reached. Furthermore, this is the basic outline of the particle-based models, where the energy potential landscape of each particle is computed and used to update the states. The state-of-the-art MD simulation packages, such as LAMMPS[59], GROMACS[60], and NAME[61], have been implemented and widely used in a variety of applications. However, many physical phenomena in biology, chemistry, and material science, which are caused by the process at the atomistic scale, determine the material behaviour on the larger scale. Due to computational limitation, atomistic MD is infeasible to study long-time phenomena in large-scale systems, in which the scales are far beyond the atomistic scales[62].

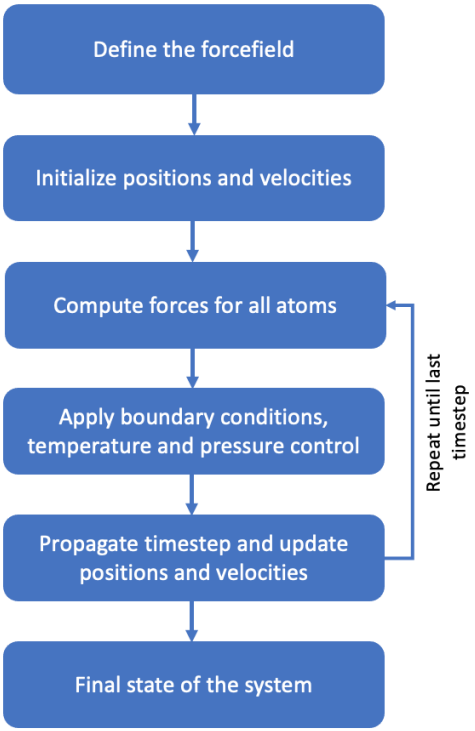

Figure 2.6.: Flowchart of MD code, in which the coordinates and velocities of each particle are updated in each timestep based on the force computed from the forcefield and additional information, i.e. boundary conditions, temperature and pressure control.

2.2. Coarse grained model

To enable simulation at the mesoscopic scale, a common approach is to reduce the resolution of the model by eliminating most of the atomistics details while retaining the essential information that reproduces consistent results with the atomistic level. This is known as coarse-grained (CG) modelling[13–15, 63]. CG methods capture the slow collective motions and average out the fast local motions, as a result there is less degrees of freedom at the CG level.

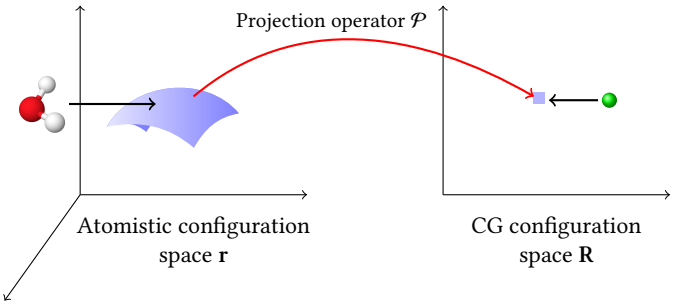

Figure 2.7.: Schematic diagram of projection of the atomistic representation in the high-dimensional space onto the CG representation in the low-dimensional space using coarse-graining method

A proper CG model should be capable of reproducing the physical and chemical properties of the underlying atomistic system. In other words, the statistical equilibrium distribution of the CG model should be closely resemble that of the atomistic model. Considering the atomistic representation in the high-dimensional space is given by $\mathbf{r} \in \mathbb{R}^{3N}$, which contains all atomistic details. The CG representation is the projection of the atomistic representation from the high-dimensional space to the low-dimensional space by eliminating the irrelevant fast degrees of freedom. It is given by

$$\mathbf{R} = \mathcal{P}(\mathbf{r}) \in \mathbb{R}^{3n} \tag{2.14}$$

where $N > n$ and $\mathcal{P}$ is a projection operation from the high-dimensional space to the low-dimensional space, where it depends on the choice of the mapping scheme. The relation between the equilibrium distribution of the atomistic model and that of the CG model is given by

$$p^{CG}(\mathbf{R}) = \int \delta(\mathbf{R} - \mathcal{P}(\mathbf{r}))p^{FG}(\mathbf{r})d\mathbf{r} \tag{2.15}$$

where $p^{FG}(\mathbf{r})$ is equilibrium distribution of the atomistic model and $p^{CG}(\mathbf{R})$ is equilibrium distribution of the CG model. In order to construct a CG model with a consistent equilibrium distribution, two criteria need to be satisfied: 1) a suitable CG mapping scheme 2) appropriate interactions between the CG sites.

In practice, the mapping scheme refers to replacing a cluster of heavy atoms with a pseudo-particle known as a CG bead. However, there is no unique way

for mapping a set of atoms to a CG bead, and random mapping is also not possible. The CG mapping scheme requires priori knowledge, particularly the chemical intuition[64]. The choice of CG description should be based on the physical and chemical properties of the material to ensure the CG model preserves the physical properties, structural correlations, and thermodynamics[65, 66].

To implement the CG mapping, the CG representation is connected to the atomistic representation by placing a CG bead at the center of mass (COM) of a group of atoms. The position $\mathbf{R}$ and the momentum $\mathbf{P}$ of the CG bead are given by

$$\mathbf{R} = \frac{1}{M} \sum_{i=1}^{N_c} m_i \mathbf{r}_i, \tag{2.16}$$

$$\mathbf{P} = \sum_{i=1}^{N_c} \mathbf{p}_i, \tag{2.17}$$

where M is the total mass of the cluster $M = \sum_{i=1}^{N_c} m_i$ with N_c atoms in the cluster. Here $\mathbf{r}_i$, $\mathbf{p}_i$, and m_i denote the position, momentum, and mass of particle i in the cluster respectively.

After determining the CG representation using a mapping scheme, appropriate interactions between the CG beads have to be constructed. These interactions in the CG model should capture the effects in the lower resolution model and reflect the correct physics, so that the model not only provides efficiency, but also fundamental insight and quantitative predictions. In order to construct the forcefield for CG model, there are two commonly used approaches: (i) top-down approach, (ii)bottom-up approach.

For the top-down approach, the CG model is based on the experimental observations at the length scales of the CG model[67, 68]. To construct the top-down model, the CG forcefield parameters are optimized to reproduce experimental phenomena or macroscopic thermodynamics properties[69, 70]. This approach is able to reproduce experimental observations and predict phenomena based on the general symmetry principles, which determine the properties that are preserved with increasing length scales. Therefore, the top-down CG forcefields provide a high transferability across different systems. However, there is no direct connection between the microscopic description

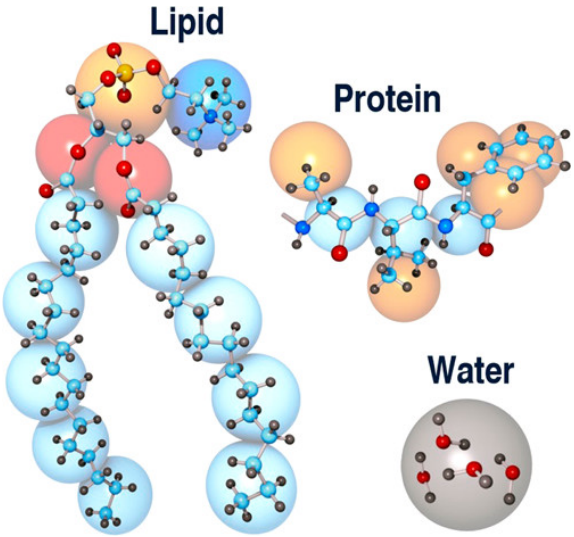

Figure 2.8.: Schematic illustration to map the atomistic representation of molecules to the CG representation using a mapping scheme based on the chemical and physical intuition (reproduced from [15] with permission from the American Chemical Society).

and the top-down CG model, resulting in the inability to accurately reproduce the structural and static properties of the underlying atomistic system.

In contrast, the bottom-up approach constructs the CG model based on the atomistic model of the same system. The forcefield parameters of the bottom-up model are optimized by matching microscopic static and structural properties obtained from the high-resolution model[71–73]. There are several methods to construct the bottom-up CG forcefield. The Boltzmann inversion[74] is a straightforward approach that constructs the CG potential from the atomistic distribution function in eq.(2.15). The potential constructed by the Boltzmann inversion method is equivalent to the atomistic pair potential of mean force

$$U(r) = -k_B T \ln g(r), \tag{2.18}$$

where $g(r)$ is the radial distribution function (RDF) obtained from the atomistic model. The Boltzmann inversion potential is a statistical pair potential, which provides an accurate description of isolated interactions. However, it fails to accurately reproduce atomistic distribution functions in strongly

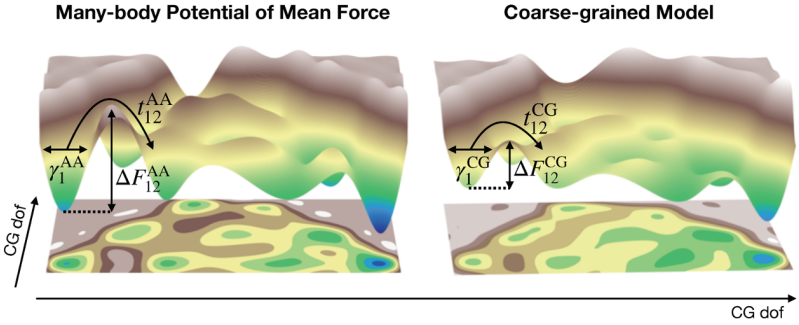

Figure 2.9.: Schematic diagram of the energy landscape of the atomsitic system (left) and the CG system (right), in which the energy landscape in the CG model is smoothened, lowering the energy barrier between CG sites.(reproduced from [64] with permission from MDPI).

coupled system as the CG distribution only reflects the single potential. Another widely used approach is the force-matching method[75, 76], which samples all atomic conformations to obtain the effective pair force between CG beads, corresponding to the potential of mean force. Since the PMF in force-matching approach is conformationally dependent, it can reproduce the structural features of the atomistic model accurately. While the transferability of the bottom-up models is lower than that of the top-down models, they are better at capturing the structural characteristics and static properties of the system.

There are three main reasons attribute to the significant increase in computational speed in the CG model. Firstly, there is a drastic reduction in the number of particles used in the simulation. Each CG particle represents several atoms along with associated hydrogen atoms. With fewer number of particles, the computation cost of the force calculations and particles propagation are significantly reduced. Secondly,the fastest oscillation frequencies in the CG simulation are decreased. In the atomistic model, bond potentials typically have the fastest oscillation frequency. However, in the CG model, the masses of the CG particles are higher, resulting in a reduction of the bond oscillation frequency. Consequently, the timestep of integration can be usually increased by a factor of ten. Lastly, the energy landscape in the CG simulation is much smoother compared to the atomistic model. The atomistic energy landscape exhibits local energy minima and traps, as shown in fig.(2.9),

which can significantly slow down the dynamics of the system or trap it in certain configurations. In contrast, the energy landscape in the CG system is averaged between CG sites, smoothing out some local traps.

The CG model enables to simulate system at a larger time and length scales, however during coarse-graining it eliminates the fast degrees of freedom that contribute to the dynamical properties of the system. Various phenomena of complex fluid or soft matter, i.e. polymer solutions, colloids, and liquid crystals, are related to the dynamical behaviour at the mesoscopic scale[6, 77]. Therefore, conventional CG model exhibits significant errors in reproducing the dynamical properties of soft matter [78], limiting their ability to study long-time dynamical behaviour of soft matter systems.

2.3. Dissipative Particle Dynamics

Both molecular interactions and transport behaviour in soft matter have significant impacts on its properties[7, 79]. To accurately model soft matter, it is essential to describe hydrodynamics, molecular interactions, as well as thermal fluctuations of the system. Several simulation methods for mesoscopic modelling, such as Langevin dynamics[80], dissipative particle dynamics[28], multiparticle collision dynamics[23], have been developed based on the framework of the CG model. Dissipative particle dynamics (DPD), which is the method closest to the CG model, is a particle-based approach that takes hydrodynamics and thermal fluctuations into account and can be employed to simulate complex fluids and soft matter at mesoscopic level. DPD was initially introduced by Hooger-brugge and Koelman[18], and later improved by Espanol and Warren with a proper statistical mechanics foundation by solving the Fokker–Planck–Boltzmann equation[19].

The original DPD model was developed to study the fluid dynamics of molecular fluids, which is consistent with the Navier-Stokes equations.[18]. In contrast to the CG model discussed in the previous chapter, in which a group of atoms is replaced by a pseudo particle, the DPD model considers each particle as a fluid element. The motion of the pseudo particles is governed by three types of pairwise forces: conservative force, dissipative force, and random force. The equation of motion of the DPD particle is given by[19]

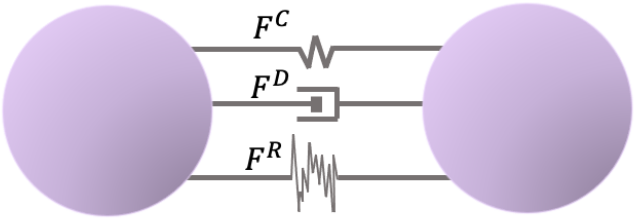

Figure 2.10.: Illustration of the interactions between a DPD particle pair which consist of 1) conservative force F^C, 2) dissipative force F^D, and 3) random force F^R (adapted from [28] with permission from the American Institute of Physics)

$$M_I \frac{d\mathbf{V}_I}{dt} = \sum_{J \neq I} \mathbf{F}_{IJ} = \sum_{J \neq I} (\mathbf{F}^C_{IJ} + \mathbf{F}^D_{IJ} + \mathbf{F}^R_{IJ}), \tag{2.19}$$

where $\mathbf{F}_{IJ}$, $\mathbf{F}^C_{IJ}$, $\mathbf{F}^D_{IJ}$ and $\mathbf{F}^R_{IJ}$ are total force, conservative force, dissipative force and random force acting on particle I by particle J.

For the conservative force, it is given by the gradient of the potential energy $U(\mathbf{R})$

$$\mathbf{F}^C_{IJ} = -\frac{\partial U(\mathbf{R})}{\partial \mathbf{R}_I}, \tag{2.20}$$

where the functional form of the potential should be translational and rotational invariant to ensure the conservation of linear and angular momentum. In the original DPD formalism, the purely repulsive potential is used

$$U(\mathbf{R}) = \frac{1}{2} \sum_{IJ} a_{IJ} (1 - |\mathbf{R}_{IJ}|/\mathbf{R}_c)^2, \tag{2.21}$$

where $\mathbf{R}_{IJ} = \mathbf{R}_J - \mathbf{R}_I$ is the relative coordinates between particles I and J, a_{IJ} is a interaction constant, and $\mathbf{R}_c$ is the cutoff distance. When $\mathbf{R}_{IJ}$ exceeds $\mathbf{R}_c$, the conservative force is zero.

The dissipative force $\mathbf{F}^D_{IJ}$ reduces the radial velocities differences between particles and it is given by

$$\mathbf{F}^D_{IJ}(\mathbf{R}, \mathbf{V}) = -\gamma \omega_D(\mathbf{R}_{IJ})(\mathbf{V}_{IJ} \cdot \mathbf{e}_{IJ})\mathbf{e}_{IJ}, \tag{2.22}$$

where γ is a friction coefficient, $\omega_D(\mathbf{R}_{IJ})$ is a dissipative force weight function related to $\mathbf{R}_{IJ}$, $\mathbf{V}_{IJ} = \mathbf{V}_I - \mathbf{V}_I$ is the relative velocity, and $\mathbf{e}_{IJ}$ is the unit vector of the radial direction between particles I and J.

The random force $\mathbf{F}_{IJ}^R$ accelerates the movement of the DPD particles by keeping the system's temperature constant and it is given by

$$\mathbf{F}_{IJ}^R(\mathbf{R}) = -\sigma\omega_R(\mathbf{R}_{IJ})\frac{dW_{IJ}}{dt}\mathbf{e}_{IJ}, \tag{2.23}$$

where σ is a random force constant, ω_R is the random force weight function, dW_{IJ} is an independent increment of Wiener process. To satisfy the condition of the fluctuation-dissipation theorem[19], the random force constant σ is linked to γ directly, i.e. $\sigma^2 = 2\gamma k_B T$, and the random force weight function $\omega_R(r_{IJ})$ is also connected to the dissipative force weight function, i.e. $\omega_D(r_{IJ}) = [\omega_R(r_{IJ})]^2$. Here k_B denotes the Boltzmann constant and T is the temperature of the system.

The static properties of the DPD system are determined by the conservative force, which can be modified by adding additional interactions[81], such as spring, attractive potential or repulsive potential. The static probability distribution of the DPD system is given by the Gibbs canonical ensemble

$$\rho(\mathbf{R}, \mathbf{V}) = \frac{1}{Z}exp\{-\sum_{i}^{N}(\frac{1}{2}M_I V_I + U(\mathbf{R}))/k_B T\}, \tag{2.24}$$

where Z is the canonical partition function. On the other hand, the dynamical properties of the DPD system are governed by the dissipative and random forces. Since all forces are pairwise in the DPD model, both linear and angular momentum are conserved. As a result, the DPD model reproduces hydrodynamic behaviour and satisfies the Navier-Stokes equation[82].

There are three main advantages of the DPD model: 1) The pairwise interaction in the DPD system is relatively soft, allowing for a large timestep that improves the computational efficiency. 2) Due to the conservation of momentum, the DPD model exhibits hydrodynamic behaviour and is consistent with the Navier-Stokes equation. Additionally, the random force acts as a thermostat to include the thermal fluctuations to the system. Therefore, the DPD model is efficient at simulating complex fluids, where both hydrodynamics and thermal fluctuation are included. 3) The DPD model is particle-based and

meshfree, making it suitable for simulating complex fluid flows with moving interfaces.

Compared to conventional CG model, the DPD model is more effective in studying complex fluid transport behaviour at the mesoscopic level. Each pseudo particle in the DPD model represents a fluid element, and the interactions between them are constructed by matching the hydrodynamic behaviour of the complex fluid. However, the pseudo particles and the interactions in the DPD model lack a detailed physical derivation and description to relate them with the microscopic system. Therefore, the interaction between pseudo particles is oversimplified, unphysical, and inconsistent with the microscopic system, restricting the ability of the DPD model to study mesoscopic behaviour in soft matter.

2.4. Continuum model

Even though the DPD model can simulate phenomena at the mesoscopic level, macroscopic scale modelling remains impractical for it due to the drastic increase in computational cost with the number of particles. To simulate the system at larger scales, one can model material as a continuous mass instead of discrete particles, which is known as the continuum model (CM)[12, 83]. CM is a coarse version of the particle system, where the length scale is much larger than the interatomic distance. In the continuum model, the material is governed by physical laws such as mass conservation, momentum conservation, and energy conservation. As a result, CM is based on the macroscopic material behaviour and ignores the microscopic molecular interactions.

To represent a system with a set of particles by a system with continuous material domain, two main assumptions are made: 1) the continuum limit: each volume element in the CM should contain a large number of atoms[84] and 2) the local equilibrium assumption: the volume of the element should be large enough to reproduce the thermodynamic behaviour of the whole system.[85] Consequently, each space point in the CM can be considered as a microscopic system with local thermodynamic equilibrium. Moreover, the differences of the physical quantities, i.e. temperature, pressure, and concentration, between a volume element and its neighbour are assumed to be small, such that the behaviour of the system can be described mathematically

by partial differential equations, which are the foundation of many physical laws at the macroscopic scale.

In continuum mechanics, the behaviour of a material is approximated as continuous with space and time, and the physics of the material is governed by the following coupled fundamental equations[86]:

$$\dot{\rho} + \rho(\nabla \cdot \mathbf{v}) = 0, \tag{2.25}$$

$$\rho\mathbf{v} - \nabla \cdot \boldsymbol{\sigma} + \rho\mathbf{b} = 0, \tag{2.26}$$

$$\boldsymbol{\sigma} = \boldsymbol{\sigma}^T, \tag{2.27}$$

$$\rho\dot{e} - \sigma : (\nabla\mathbf{v}) + \nabla \cdot \mathbf{q} - \rho s = 0, \tag{2.28}$$

where ρ is the element density, $\mathbf{v}$ is the element velocity, $\boldsymbol{\sigma}$ is the Cauchy stress tensor, $\mathbf{b}$ is the body force, e is the internal energy density, $\mathbf{q}$ is the heat flow vector, and s is the source term of the energy density. The four equations correspond to the conservation of mass, linear momentum, angular momentum, and energy, respectively.

Under the framework of the continuum mechanics, the general coupled equations can be modified and applied to various basic physics problems, such as diffusion and heat transport in the materials, as well as the flow of Newtonian fluids in fluid mechanics. Additionally, there are numerous other applications, such as charge transport in charge-carrying materials[87] and the interfacial phenomena in multiphase systems[88].

To solve the coupled partial differential equations, two main approaches are commonly used: the finite element method (FEM)[89] and the finite difference method (FDM)[90]. In this thesis, only FDM approach will be employed. In the FDM approach, the material domain is divided by a set of nodes, forming a group of subdomains known as grids, as presented in fig.(2.11). A finite difference function is used to approximate the derivatives of physical quantities at each node. In order to solve the partial differential equation, it can be approximated by a linear equation by taking the neighbouring nodes

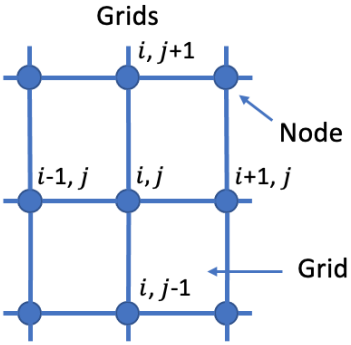

Figure 2.11.: Illustration of the finite difference method (FDM), in which the material domain is divided by the nodes to form a group of subdomains.

into account. By using the central difference scheme, the first derivative $\frac{\partial u}{\partial x}$ of physical quantities u at a node n can be approximated

$$\frac{\partial u}{\partial x} = \lim_{h \to 0} \frac{u(x+h) - u(x-h)}{2h} \approx \frac{u(x+h) - u(x-h)}{2h}, \tag{2.29}$$

where x is the position of node n and h is the separation between the neighbouring nodes. Moreover, the second derivative $\frac{\partial^2 u}{\partial x^2}$ of the physical quantities u at node n is approximated as

$$\frac{\partial^2 u}{\partial x^2} \approx \frac{\frac{\partial u}{\partial x}\Big|_{x=x+\frac{h}{2}} - \frac{\partial u}{\partial x}\Big|_{x=x-\frac{h}{2}}}{h} = \frac{u(x+h) - 2u(x) + u(x-h)}{h^2}. \tag{2.30}$$

Furthermore, the choice of boundary conditions in the continuum model is crucial for obtaining the correct interpolation function to describe the physics of the system[91]. One of the most commonly used boundary conditions is the Dirichlet boundary condition, which fixes the boundary value of physical quantities u by a given value

$$u(a) = A_1, \tag{2.31}$$

where a is the boundary of the system and A_1 is a given value at the boundary. This boundary condition is suitable for simulating systems which are connected to a giant neighbouring system, such as heat bath. On the other hand,

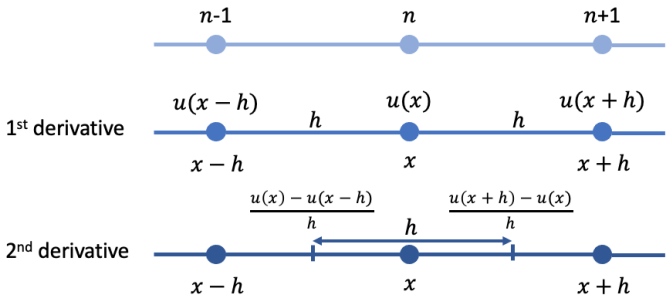

Figure 2.12.: Illustration of the finite difference approximation for the first and second derivative of physical quantities u at node n.

the Neumann boundary condition is another common boundary condition in the continuum model, where the normal derivative of the physical quantities u is fixed by a given value

$$\hat{n} \cdot \nabla u(a) = A_2, \tag{2.32}$$

where $\hat{n}$ the normal vector of the system boundary and A_2 is a given value at the boundary. This boundary condition is suitable to simulate an isolated system, which has zero flux at the boundary.

When all the partial differential equations and the boundary conditions of the system are all known, the physical states of every node in the system can be computed. The Jacobi method[92], which is a simple and straightforward iterative algorithm for solving a system of linear equations, is employed. Considering $\boldsymbol{\mathcal{A}}\mathbf{x} = \mathbf{b}$ is a system of n linear equations with unknown $\mathbf{x}$, it can be written as

$$\sum_{ij}^{n} a_{ij} x_j = b_i, \tag{2.33}$$

where a_{ij} is the element in matrix $\boldsymbol{\mathcal{A}}$, x_j is the element in vector $\mathbf{x}$ and b_i is the element in vector $\mathbf{b}$. The algorithm starts with an initial guess of the solution $\mathbf{x}^{(0)}$. In each iteration of the Jacobi method, the solution of the k-th iteration $\mathbf{x}^{(k)}$ is given by

$$x_i^{(k)} = \frac{b_i - \sum_{i \neq j} a_{ij} x_j^{(k-1)}}{a_{ii}}, \tag{2.34}$$

which is related to the solution of the $(k-1)$-th iteration. The solution of the k-th iteration is then used as the input in eq.(2.34) to generate the solution of the next iteration. By repeating this procedure, the final solution of $\mathbf{x}$ is obtained when the convergence condition is satisfied.

The outline of the code of a continuum model is presented in fig.(2.13). Before the start of the simulation, the governing equations of the system and the boundary conditions are defined. At the initial timestep, an initial guess of the solutions for the physical states of all nodes is used as the input to solve the partial differential equations using a solver. At each simulation timestep, the current states of all nodes are used as the input to solve the governing equations, and the physical states of each node are updated accordingly. This routine is repeated until the end time of the simulation, and the dynamical behaviour of the system can then be obtained. This is also the general outline of the grid-based models, where the states of each node are computed by solving partial differential equations at every timestep. However, it is important to note that the grid-based models are limited in mesoscopic modelling due to lack of the resolution required to describe the molecular interactions. Therefore, the continuum model is unable to capture the details of the underlying physics contributing to the mesoscopic behaviour.

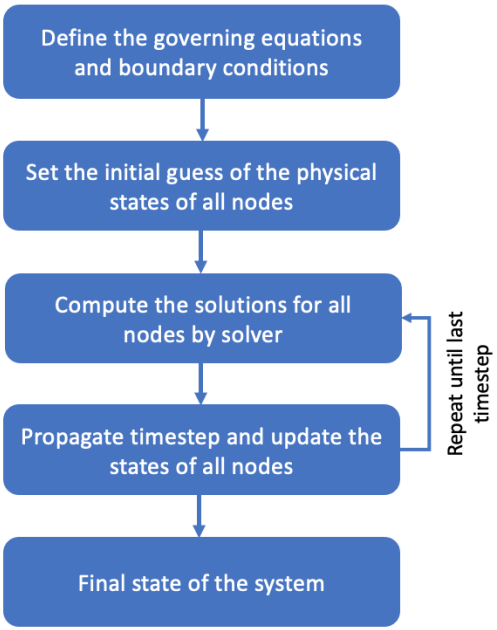

Figure 2.13.: Flowchart of the code for the continuum model, in which the physical states of each nodes are updated from the previous states and the boundary conditions by solving the partial difference equations in every timestep

3. Dynamically consistent coarse grained Molecular Dynamics

In the previous chapter, I presented different models for simulating material properties, each with its own advantages and limitations. Classical MD has high resolution but is computationally expensive and limited to the atomistic resolution. Coarse-grained model can simulate systems at larger scales but exhibits significant errors in dynamical properties over long timescales. Dissipative particle dynamics is consistent with hydrodynamic properties but lacks a proper chemical description for pseudo particles. Continuum model, based on grids rather than particles, can simulate much larger scales but lose the details of molecular interactions. To enable simulation of mesoscopic phenomena in soft matter, a model should be able to 1) access large length and time scales, 2) provide consistent dynamical properties, and 3) capture the atomistic details and interactions.

In the 1960s, Mori and Zwanzig proposed a derivation of a generalized Langevin equation (GLE) via a projection operator, which is known as the Mori-Zwanzig formalism (MZ) [29, 30]. This formalism provides a systematic way to relate the mesoscopic variables to the microscopic variables, such that the GLE describes the non-equilibrium evolution of collective variables which directly extracted from the phase-space of the microscopic system. However, the GLE is too complicated to be employed as a computational tool as solving the numerical integration of an integro-differential equation is difficult. Recently, various approaches have been proposed to make the Mori–Zwanzig formalism computationally practical[93, 94]. In this chapter, I will present the Mori-Zwanzig formalism and the coarse-graining procedure for a molecular system in detail. I will also demonstrate the formulation of the anisotropic MZDPD model and analyse its performance by comparing it with other CG models.

3.1. Mori-Zwanzig formalism

In this section, the derivation of the Mori-Zwanzig formalism is presented. Considering $\mathcal{P}$ is a projection operator

$$\mathcal{P}(\Gamma) = \Gamma_{slow}, \tag{3.1}$$

where Γ is the phase space of a system and Γ_{slow} is the subspace of slow variables in Γ, such that $\mathcal{P}$ projects out the slow degrees of freedom. Moreover, an orthogonal counterpart $\mathcal{Q}$ of the projection operator can be defined as

$$\mathcal{Q} = 1 - \mathcal{P}. \tag{3.2}$$

When the projection operator acts on a variable X in phase space Γ, the projection is given by

$$\mathcal{P}X = \frac{\langle A, X\rangle}{\langle A, A\rangle} A, \tag{3.3}$$

where A is a collective variable in the subspace Γ_{slow}.

Considering the Liouville equation of the collective variable A

$$\frac{dA}{dt} - i\mathcal{L}A = 0, \tag{3.4}$$

where $\mathcal{L}$ is the Liouville operator, the solution of eq.(3.4) is given by

$$A(t) = e^{i\mathcal{L}t}A. \tag{3.5}$$

By inserting operator $\mathcal{P}$ and $\mathcal{Q}$ into eq.(3.4), it can be rewritten as

$$\begin{aligned} \frac{dA}{dt} &= ie^{i\mathcal{L}t}(\mathcal{P} + \mathcal{Q})\mathcal{L}A \\ &= \Omega A(t) + ie^{i\mathcal{L}t}\mathcal{Q}\mathcal{L}A, \end{aligned} \tag{3.6}$$

where $\Omega A(t) = ie^{i\mathcal{L}t}\mathcal{P}\mathcal{L}A$ and Ω denotes the frequency matrix.

For the second term in eq.(3.6), the Dyson identity gives us

$$ie^{i\mathcal{L}t}\mathcal{Q}\mathcal{L}A = ie^{i\mathcal{Q}\mathcal{L}t}i\mathcal{Q}\mathcal{L}A + i\int_0^t \mathrm{d}s e^{i\mathcal{L}(t-s)}\mathcal{P}\mathcal{L}e^{\mathcal{Q}\mathcal{L}s}\mathcal{Q}\mathcal{L}A, \tag{3.7}$$

where the random force $F^Q(t) = ie^{iQ\mathcal{L}t}Q\mathcal{L}A$ and the memory function $K(t) = i\mathcal{P}\mathcal{L}e^{iQ\mathcal{L}t}Q\mathcal{L}$ are defined. In the end, the generalized Liouville equation is given by

$$\frac{dA}{dt} = \Omega A(t) + \int_0^t \mathrm{d}sK(s)A(t-s) + F^Q(t). \tag{3.8}$$

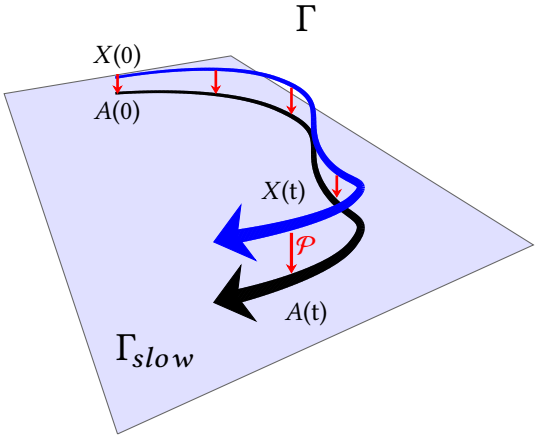

Figure 3.1.: Schematic diagram of the Mori-Zwanzig formalism, in which the projection operator $\mathcal{P}$, represented by the red arrows, projects a variable X, which is indicated by the blue arrow, in phase space Γ into a collective variable A, which is indicated by the black arrow, in the subspace Γ_{slow}. In the MZ formalism, the dynamics of A is guided by the dynamics of X to ensure the dynamical consistency.

3.2. Coarse-graining of molecular system

Based on the Mori-Zwanzig formalism, a N-body problem can be simplified by separating the slow and fast degrees of freedom, such that the coarse-graining of molecular systems can be performed in a systematic way. Recalling the CG model and the DPD model in ch.(2), they both show deficiencies in coarse-graining. The CG model eliminates the fast degrees of freedom, leading to significant errors in dynamical properties, while the DPD model lacks a connection with the underlying microscopic system. A question arises: is it

possible to connect these two models in a way that captures the microscopic system and ensures consistent dynamical properties?

The answer is yes. On the left hand side of the expression of the generalized Liouville equation in eq.(3.8), there are three terms: the projected term, memory term, and fluctuating term. When compared to the equation of motion of the DPD particle in eq.(2.19), these three terms can be related to the conservative, dissipative, and random forces in the DPD model. This suggests that an N-particle system can be coarse-grained using the MZ formalism within the framework of the dissipative particle dynamics. As a result, the CG model gives the intuition for mapping groups of atoms to pseudo particles, the MZ formalism provides a systematic way to project information from the microscopic system to the mesoscopic system, and the DPD framework ensures the consistency of the hydrodynamic behaviour for a system over time.

However, the complexity of solving the integro-differential equation is another problem that hinders the practical use of the MZ approach. In order to realize the MZ formalism as a computational tool, Hijon[93] proposed constrained CG degrees of freedom to make the Markovian approximation exact, while Lei[94] performed constrained MD simulations by fixing the radius of gyration to construct CG system. In the following, the details of coarse-graining an N-particle system using the MZ formalism are presented.

Considering an N-particle system in a microscopic state $\Gamma = \{\mathbf{r}_i, \mathbf{p}_i\}$, with instantaneous positions $\mathbf{r}_i$ and momenta $\mathbf{p}_i$ of particle i, where $i = 1...N$. The atomistic Hamiltonian of the system is given by

$$H(\Gamma) = \sum_{i=1}^{N} \frac{\mathbf{p}_i^2}{2m_i} + \frac{1}{2} \sum_{i \neq j} U(\mathbf{r}_{ij}), \tag{3.9}$$

where m_i is the mass of particle i. In order to abstract the atomic details, the N-particle system is mapped into a K-cluster system by grouping atoms into clusters. The dynamics of the clusters can be described by proper CG variables with lower resolution. The position $\mathbf{R}$ and the translational momentum $\mathbf{P}$ of the center of mass (COM) of a cluster of atoms are given by eq.(2.16) and eq.(2.17) respectively.

The dynamics of the high-resolution system with full atomistic detail is determined by the atomistic Hamiltonian in eq.(3.9), and the time evolution of microscopic state is described by the Liouville equation

$$\frac{\partial \Gamma}{\partial t} + i\mathcal{L}\Gamma = 0. \tag{3.10}$$

The projection operator $\mathcal{P}$ and its orthogonal counterpart $\mathcal{Q}$ are employed to decompose the system into the fast and slow degrees of freedom. The CG variables, which are the slow degrees of freedom that of our interest, are projected out by the projection operator $\mathcal{P}$, while the remaining fast degrees of freedom, which correspond to the irrelevant atomistic details, are projected out by $\mathcal{Q}$. By using the Mori-Zwanzig projection, the equation of motion (EOM) of a CG particle can be written in terms of the CG variables[93–95]

$$\begin{aligned}\frac{\mathrm{d}}{\mathrm{d}t}\mathbf{P}_I =& \frac{1}{\beta}\frac{\partial}{\partial \mathbf{R}_I} \ln\omega(\mathbf{R}) \\ & - \beta \sum_{J=1}^{K} \int_0^t ds \langle [\delta \mathbf{F}_I^{\mathcal{Q}}(t-s)][\delta \mathbf{F}_J^{\mathcal{Q}}(0)]^T \rangle \frac{\mathbf{P}_J(s)}{M_J} \\ & + \delta \mathbf{F}_I^{\mathcal{Q}}(t),\end{aligned} \tag{3.11}$$

where $\beta = 1/k_B T$ with T denotes the temperature and k_B denotes the Boltzmann constant. $\mathbf{R} = \{\mathbf{R}_1, \mathbf{R}_2, \ldots, \mathbf{R}_K\}$ is the phase point in the CG phase space, $\omega(R)$ is the normalized partition function of all microscopic configurations at phase point $\mathbf{R}$, and $\delta \mathbf{F}^{\mathcal{Q}}$ is the $\mathcal{Q}$-projected random force. In the right hand side of eq.(3.11), each term corresponds to a conservative force, dissipative force and random force respectively, which is consistent with the framework of the DPD model. The conservative force represents the many-body mean force by the change of microscopic configurations. Both dissipative force and random force depend on the choice of the projection operator $\mathcal{P}$, such that they compensate the missing degrees of freedom during coarse-graining. The dissipative force is computed from the time convolution of the memory kernel of the random force and the momenta of the cluster. And the $\mathcal{Q}$-projected random force is given by

$$\delta \mathbf{F}_I^{\mathcal{Q}}(t) = \mathbf{e}^{-\mathcal{Q} i \mathcal{L} t} \delta \mathbf{F}_I(t), \tag{3.12}$$

where $\delta \mathbf{F}_I(t)$ is the fluctuating force acting on cluster I and is given by $\delta \mathbf{F}_I(t) = \mathbf{F}_I(t) - \langle \mathbf{F} \rangle$ with $\mathbf{F}_I(t)$ denotes the instantaneous force on cluster I. By using the zeroth order approximation[96], i.e. $\mathbf{e}^{-\mathcal{Q} i \mathcal{L} t} \approx \mathbf{e}^{-i\mathcal{L}t}$, the random force correlation function can be approximated by the fluctuating force correlation function

$$\langle [\delta \mathbf{F}_I^{\mathcal{Q}}(t-s)][\delta \mathbf{F}_J^{\mathcal{Q}}(0)]^T \rangle \approx \langle [\delta \mathbf{F}_I(t-s)][\delta \mathbf{F}_J(0)]^T \rangle. \tag{3.13}$$

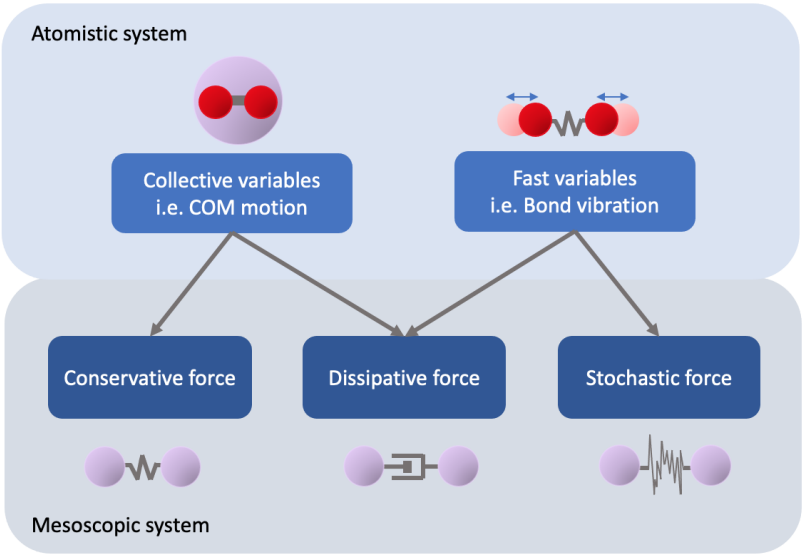

Figure 3.2.: Illustration of the MZ formalism to coarse grain an atomistic system to a mesoscopic system, in which the collective variables are mapped to conservative force, the fast variables are mapped to the stochastic force, and the effects from the collective and fast variables are approximated by the dissipative force. Red sphere indicates the atomic particle and purple sphere indicates the CG particle.

When the fast degrees of freedom couples with the slow degrees of freedom, a strong non-linear memory effect on the dynamics of the CG variables has been observed[97]. In this thesis, I only consider systems that the timescale of the force, which is determined by the collision time, is faster than the characteristic timescale of the momenta, which is proportional to the mass of particle. As a result, the characteristic timescale of the momenta (the slow variable) and the force (the fast variable) are well-separated, and thus the system can treated as a Markovian process. In this limit, the auto-correlation function of the fluctuating force can be replaced by delta function via the Markovian approximation

$$\beta\langle[\delta\mathbf{F}_I(t-s)][\delta\mathbf{F}_J(0)]^T\rangle = 2\gamma_{IJ}\delta(t-s), \tag{3.14}$$

$$\beta \int_0^t ds \langle [\delta \mathbf{F}_I(t-s)][\delta \mathbf{F}_J(0)]^T \rangle \frac{\mathbf{P}_J(s)}{M_J} = \gamma_{IJ} \frac{\mathbf{P}_J(t)}{M_J}, \tag{3.15}$$

where $\gamma_{IJ} = \beta \int_0^t ds \langle [\delta \mathbf{F}_I(t-s)][\delta \mathbf{F}_J(0)]^T \rangle$ is the frictional tensor.

The force acting on a CG particle in eq.(3.11) depends on the microscopic state in phase space, which is determined by the positions and momenta of all other clusters in the system. However, the direct evaluation of the multi-body interaction is very demanding even for one-dimensional harmonic system[31]. In practice, two approximations are employed here. First, the multi-body interactions are assumed to be negligible and all interactions are pairwise. Second, the non-bonded interactions are assumed to be pairwise decomposable[98]. As a result, the total force on a cluster can be rewritten as a sum of pairwise additive forces

$$\mathbf{F}_I \approx \sum_{J \neq I} \mathbf{F}_{IJ}. \tag{3.16}$$

Moreover, the fluctuating force is assumed to be pairwise and uncorrelated in time by employing the Markovian approximation. The multi-body interactions[99] of the fluctuating terms are also negligible, so that it can be written as

$$\delta \mathbf{F}_I \approx \sum_{J \neq I} \delta \mathbf{F}_{IJ}. \tag{3.17}$$

As a result, the memory kernel can be approximated by an additive pairwise expression

$$\langle [\delta \mathbf{F}_I(t-s)][\delta \mathbf{F}_J(0)]^T \rangle \mathbf{V}_J(s) \approx \sum_{J \neq I} [\delta \mathbf{F}_{IJ}(t-s)][\delta \mathbf{F}_{IJ}(0)]^T \rangle \mathbf{V}_{IJ}(s), \tag{3.18}$$

where $\mathbf{V}_{IJ} = \mathbf{V}_J - \mathbf{V}_I$ is the relative velocity between particle I and J. In the end, the EOM of the CG particle in eq.(3.11) can be expressed in a Markovian pairwise additive form

$$\frac{\mathrm{d}}{\mathrm{d}t} \mathbf{P}_I = \sum_{J \neq I} \mathbf{F}_{IJ}(t) = \sum_{J \neq I} [\langle \mathbf{F}_{IJ} \rangle - \gamma_{IJ} \mathbf{V}_{IJ}(t) + \delta \mathbf{F}_{IJ}(t)]. \tag{3.19}$$

3.3. Isotropic Mori-Zwanzig Dissipative Particle Dynamics approach

This section presents the procedure for implementing an isotropic CG model using the MZ approach, where a cluster of atoms is represented by an isotropic spherical CG particle. The procedure presented here follows Li's approach, which constructs the isotropic CG forcefield using unconstrained MD systems of star polymer melts to avoid the effects from artificial constraints[100]. In an isotropic system, the pairwise force between CG particle pair is distance-dependent and the EOM can be expressed in a distance-dependent form

$$\frac{\mathrm{d}}{\mathrm{d}t}\mathbf{P}_I = \sum_{J\neq I}[\langle \mathbf{F}_{IJ}(\mathbf{R}_{IJ})\rangle - \gamma_{IJ}(\mathbf{R}_{IJ})\mathbf{V}_{IJ}(t) + \delta\mathbf{F}_{IJ}(\mathbf{R}_{IJ})(t)], \tag{3.20}$$

where $\mathbf{R}_{IJ} = \mathbf{R}_J - \mathbf{R}_I$ is the relative position between the COM of CG particle I and J. A system of star polymer is employed as the microscopic system, and a spherical CG particle is used to represent each star polymer, as presented in fig.(3.3).

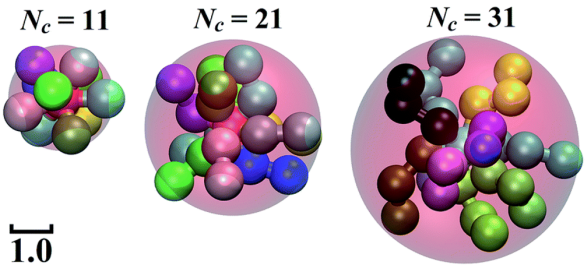

Figure 3.3.: Schematic diagram to illustrate star polymer represented by a spherical CG particle in coarse-graining, where N_c is the total number of atoms in the CG bead (reproduced from [100] with permission from the Royal Society of Chemistry)

To extract the information from the microscopic system, a melt of star polymer is sampled, such that the interactions and dynamics between the cluster can be evaluated from the MD trajectories.

To compute the conservation force in eq.(3.20) from the star polymer system, a binning method is employed, in which the distance between two molecules

is divided into many bins with width δ. As a result, the molecule pair I and J with intermolecular distance between $R_{IJ} + \frac{\delta}{2}$ and $R_{IJ} - \frac{\delta}{2}$ is considered as a pair within the bin of distance R_{IJ}. By averaging the interaction force over all pairs in the bins, the distance-dependent conservation force can be computed. Moreover, the conservation force is approximated by an empirical function in order to make the computation efficient. Typically, a bell-shaped function is employed to approximate the average conservation force[100].

The frictional force is computed from the product of the auto-correlation function of the fluctuating force and the relative velocity between cluster as in eq.(3.18). The fluctuating force is given by

$$\delta \mathbf{F}_{IJ} = \mathbf{F}_{IJ} - \langle \mathbf{F}_{IJ} \rangle, \tag{3.21}$$

where $\mathbf{F}_{IJ}$ is the instantaneous force exerted on particle I by J, and $\langle \mathbf{F}_{IJ} \rangle$ is the ensemble average of $\mathbf{F}_{IJ}$ that is computed in the conservative force. Moreover, as presented in fig.(3.4), the fluctuating force can be decomposed into radial and perpendicular components

$$\delta \mathbf{F}_{IJ} = \delta \mathbf{F}_{IJ}^{\parallel} + \delta \mathbf{F}_{IJ}^{\perp}, \tag{3.22}$$

where $\delta \mathbf{F}_{IJ}^{\parallel}$ is the radial component and $\delta \mathbf{F}_{IJ}^{\perp}$ is the perpendicular component of the fluctuating force, respectively. The memory tensor, which is the integral of the auto-correlation function of the fluctuating force, can be computed separately along radial and perpendicular direction

$$\phi_{\parallel}(\mathbf{R}_{IJ}) = \beta \int_0^{\infty} dt \langle \delta \mathbf{F}_{IJ}^{\parallel}(t) \cdot \delta \mathbf{F}_{IJ}^{\parallel}(0) \rangle, \tag{3.23}$$

$$\phi_{\perp}(\mathbf{R}_{IJ}) = \beta \int_0^{\infty} dt \langle \delta \mathbf{F}_{IJ}^{\perp}(t) \cdot \delta \mathbf{F}_{IJ}^{\perp}(0) \rangle, \tag{3.24}$$

where $\phi_{\parallel}(\mathbf{R}_{IJ})$ and $\phi_{\perp}(\mathbf{R}_{IJ})$ are the radial and perpendicular components of the friction coefficient, respectively. Similar to the conservative force, the average frictional coefficient, which is a function of the pair separation R_{IJ}, is approximated by a bell-shaped function. Furthermore, the random force can be computed from the frictional force via the fluctuation-dissipation theorem.

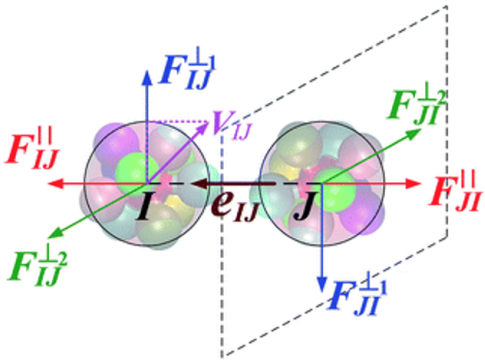

Figure 3.4.: Illustration of the pairwise interaction force between two CG particles, which is decomposed into a radial component and two perpendicular components (reproduced from [100] with permission from the Royal Society of Chemistry).

In the end, the equation of motion of the CG particle in the isotropic MZDPD model is given by

$$\begin{aligned} \mathrm{d}\mathbf{P}_I/\mathrm{d}t = \sum_{J\neq I}\mathbf{F}_{IJ} = &\sum_{J\neq I} w_C(\mathbf{R}_{IJ})\mathbf{e}_{IJ} \\ &+ \sum_{J\neq I} w_D^{\parallel}(\mathbf{R}_{IJ})(\mathbf{e}_{IJ}\cdot\mathbf{V}_{IJ})\mathbf{e}_{IJ} \\ &+ \sum_{J\neq I} w_D^{\perp}(\mathbf{R}_{IJ})[\mathbf{V}_{IJ} - (\mathbf{e}_{IJ}\cdot\mathbf{V}_{IJ})\mathbf{e}_{IJ}] \\ &+ \sum_{J\neq I} w_D^{\perp}(\mathbf{R}_{IJ})(\frac{\mathbf{R}_{IJ}}{2}\times(\boldsymbol{\Omega}_I+\boldsymbol{\Omega}_J)) \\ &+ \sum_{J\neq I} \frac{1}{\sqrt{3}}\sigma_{\parallel} w_R^{\parallel}(\mathbf{R}_{IJ})\Delta t^{-1/2} tr\{d\mathbf{W}_{IJ}\}\mathbf{e}_{IJ} \\ &+ \sum_{J\neq I} \sqrt{2}\sigma_{\perp} w_R^{\perp}(\mathbf{R}_{IJ})\Delta t^{-1/2} d\mathbf{W}_{IJ}^{A}\cdot\mathbf{e}_{IJ}^{\perp}, \end{aligned} \tag{3.25}$$

where $\mathbf{e}_{ij}$ is the unit vector of the radial direction, i.e. $\mathbf{e}_{IJ} = \frac{\mathbf{R}_{IJ}}{|\mathbf{R}_{IJ}|}$,$w_C(\mathbf{R}_{IJ})$ is the weighting function of the conservative force, $w_D^{\parallel}(\mathbf{R}_{IJ})$ and $w_D^{\perp}(\mathbf{R}_{IJ})$ are the weighting function of the frictional coefficient along the radial direction

and perpendicular direction respectively, and $\mathbf{\Omega}_I$ and $\mathbf{\Omega}_J$ are the angular velocity of CG particle I and J. Moreover, $d\mathbf{W}_{IJ}$ is a matrix of independent Wiener increments and $d\mathbf{W}^A_{IJ} = \frac{1}{2}(d\mathbf{W}^{\mu\nu}_{IJ} - d\mathbf{W}^{\nu\mu}_{IJ})$ is an antisymmetric noise matrix. In order to satisfy the fluctuation-dissipation theorem, it requires $\sigma_{\parallel} = \sigma_{\perp} = 2k_BT$ and relates the weighting functions of w_R to w_D, such that $w^{\parallel}_R = \sqrt{w^{\parallel}_D}$ and $w^{\perp}_R = \sqrt{w^{\perp}_D}$.

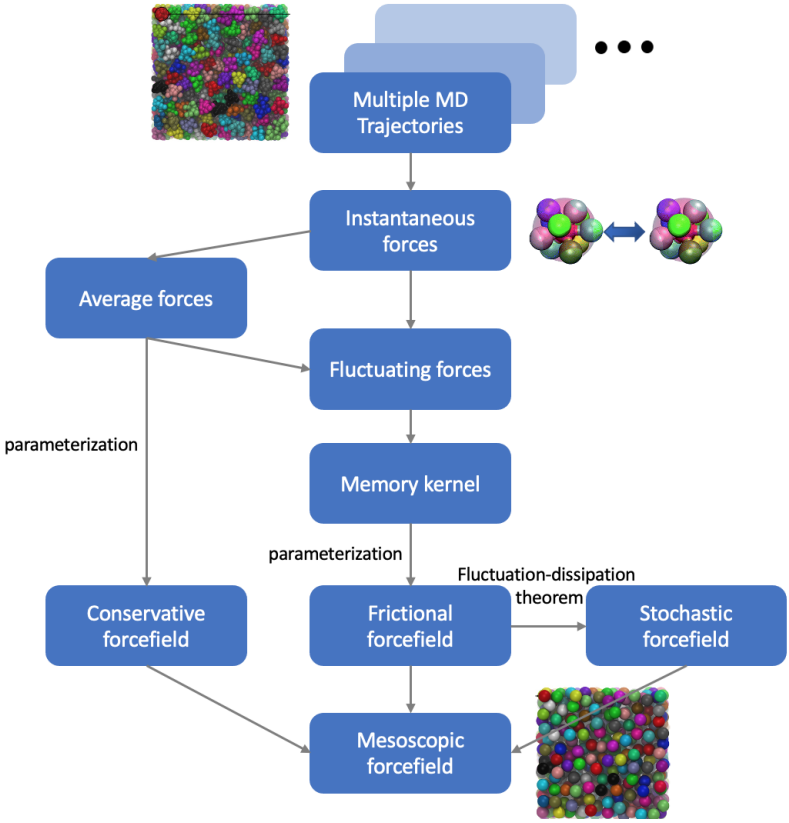

Figure 3.5.: Outline of the mesoscopic forcefield construction in the MZDPD approach, in which multiple MD trajectories are employed to optimize the forcefield parameters (adapted from [100] with permission from the Royal Society of Chemistry).

3.4. Anisotropic Mori-Zwanzig Dissipative Particle Dynamics approach

The isotropic MZDPD model, like most coarse-grained models, exhibits inaccuracies when representing non-spherical molecular structures using spherical CG particles. This is especially problematic for molecules with ring structures, such as benzene and pentacene. The spherical CG beads poorly approximate the geometric shape of these molecules, leading to significant errors in isotropic CG models.

To address this limitation, the Gay-Berne (GB) potential was developed[32, 33]. Berne and Pechukas[101] proposed this Lennard-Jones potential extension for aspherical particles by introducing range parameter and strength parameter, which represent the shape and size of an ellipsoidal particle, to describe the interparticle interactions in terms of the relative orientation with respect to the particles' principal axis. Golubkov proposed a model combining the GB potential and the point multipole expansion to construct the CG forcefield for benzene and methanol[102]. Tripathy extracted GB parameters for poly-aromatic hydrocarbons via a force matching approach[103]. Moreover, Tanis[104] and Goujon[105] illustrated that treatment of anisotropic effects at the CG level improves structural and static properties. However, the dynamical properties of the anisotropic CG system is not guaranteed to be consistent with the underlying atomistic system, since the pairwise non-conservative force is also anisotropic for ellipsoidal CG particles[106].

In this section, I extend the MZDPD formalism to anisotropic system, aiming to improve the dynamical accuracy of aspherical particles at the CG level. Here I construct a molecule-specific anisotropic forcefield that maps directly from the atomistic model and accurately reproduces the dynamical properties at the CG level. To preserve the dynamics, the anisotropic forcefield must properly represent the interactions in terms of distance and relative orientation, implying that much more complex potentials must be fitted than in the isotropic model. The EOM of the anisotropic CG particle via MZDPD approach is given by

$$\frac{\mathrm{d}}{\mathrm{d}t}\mathbf{P}_I = \sum_{J\neq I}[\langle \mathbf{F}_{IJ}(\mathbf{R}_{IJ},\mathbf{u}_I,\mathbf{u}_J)\rangle - \gamma_{IJ}(\mathbf{R}_{IJ},\mathbf{u}_I,\mathbf{u}_J)\mathbf{V}_{IJ}(t) + \sigma_{IJ}(\mathbf{R}_{IJ},\mathbf{u}_I,\mathbf{u}_J)\xi_{IJ}], \tag{3.26}$$

where $\mathbf{u}_I$ and $\mathbf{u}_J$ are the unit vectors of the orientation of ellipsoid I and J respectively, as shown in fig.(3.6a). The conservative force $\mathbf{F}_{IJ}$ and the frictional tensor γ_{IJ} are dependent on $\mathbf{R}_{IJ}$, $\mathbf{u}_I$ and $\mathbf{u}_J$. σ_{IJ} is related to γ_{IJ} through the fluctuation-dissipation relation and ξ_{IJ} is the Gaussian random variable with zero mean and unit variance.

In the following, I will present the procedure to coarse-grain an anisotropic system consisting of many anisotropic molecules at the atomistic level. To illustrate the procedure, I consider benzene as our system of interest, such that the mesoscopic forcefield is constructed directly from the trajectories of a benzene MD simulation.

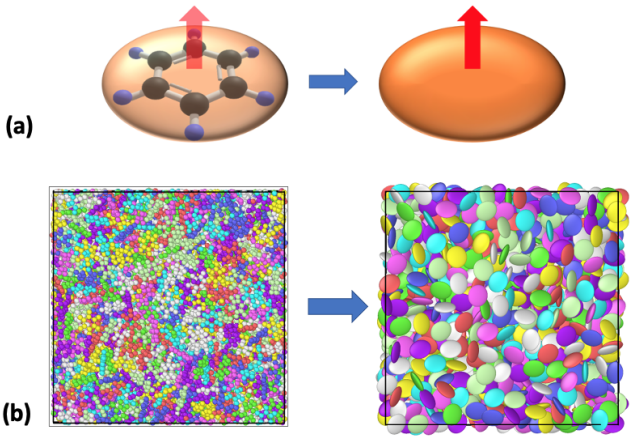

Figure 3.6.: Schematic diagram of coarse-graining an anisotropic model. (a) A benzene molecule is represented by an ellipsoidal CG particle(in orange). Red arrows indicate the normal vector of the symmetry plane. (b) Coarse-graining of anisotropic molecules in a simulation box.

3.4.1. Parameterization procedures

3.4.1.1. Microscopic system

In order to generate the microscopic data for coarse-graining, an atomistic system of 1000 benzene molecules is considered. The atomistic MD simulations was performed using LAMMPS[107] (large-scale atomic/molecular

massively parallel simulator) and the forcefield parameters for the intra- and inter-molecular interaction were obtained from the OPLS forcefield[10]. The cutoff of both Lennard-Jones (LJ) potential and Coulomb potential are 11 $\mathring{A}$ and the electrostatic force is calculated with the Particle Particle Particle Mesh method (P3M) with real space cutoff of 11 $\mathring{A}$.

For the details of the system configuration, 1000 benzene was simulated in a periodic simulation box with length 52.9451 $\mathring{A}$, which results in a density of the system of $0.874 g/cm^3$. An arbitrary initial configuration was prepared and the NVT ensemble was performed until the system reached a thermal equilibrium. Further NVT simulations were performed to generate trajectories that were used to construct the anisotropic mesoscopic forcefield. Moreover, the time scale of the force and the momenta were computed and compared to ensure that the timescales are well-separated, allowing the system to be treated as a Markovian process.

3.4.1.2. Construction of conservative force

In order to represent benzene molecules by oblate ellipsoidal particles, the intermolecular interaction between the ellipsoid pairs is described by the uniaxial Gay-Berne (GB) potential[33, 101], which represents the size, shape and interaction strength. Each GB particle is characterized by its COM position and an orientation defined by the normal vector to the molecule's symmetry plane. Moreover, a GB particle pair is characterized by the pair distance $|\mathbf{R}_{IJ}|$ and angles formed by the direction of the distance vector $\mathbf{e}_{IJ} = \frac{\mathbf{R}_{IJ}}{|\mathbf{R}_{IJ}|}$ and the normal vectors $\mathbf{u}_I$ and $\mathbf{u}_J$, eg. $\Theta = \{\theta_\alpha, \theta_\beta, \theta_\gamma\}$, with $\theta_\alpha = \cos^{-1}(\mathbf{u}_I \cdot \mathbf{u}_J)$, $\theta_\beta = \cos^{-1}(\mathbf{e}_{IJ} \cdot \mathbf{u}_I)$ and $\theta_\gamma = \cos^{-1}(\mathbf{e}_{IJ} \cdot \mathbf{u}_J)$ as shown in fig.(3.7).

To construct the conservative forcefield, the force-matching approach[103] is employed, in which the CG conservative forcefield is approximated by comparing to the atomistic MD trajectories. By employing the binning method, the distance $|\mathbf{R}_{IJ}|$ and the orientation $\Theta = \{\theta_\alpha, \theta_\beta, \theta_\gamma\}$ between two molecules are divided into many bins with width of δ_R, δ_α, δ_β and δ_γ respectively. The magnitude of the conservative force $\mathbf{F}_{IJ}(\mathbf{R}_{IJ}, \mathbf{u}_I, \mathbf{u}_J)$ is then obtained by averaging the results over the pairs with distance and orientation in the specific

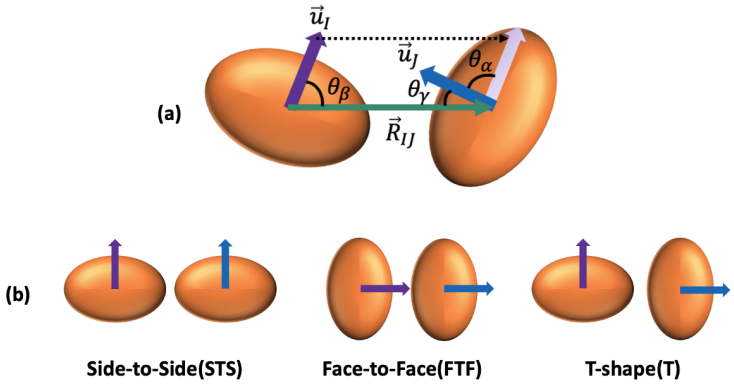

Figure 3.7.: Schematic illustration to the configuration of oblate ellipsoidal CG particle pairs. (a) Each CG pair is characterized by the pair distance $|\mathbf{R}_{IJ}|$ and the relative orientation $\Theta = \{\theta_\alpha, \theta_\beta, \theta_\gamma\}$, (b) the illustration of three configurations, i.e. side-to-side(STS), face-to-face(FTF) and T-shape(T).

distance bin and orientation bin. The LJ interaction between pair of GB particles I and J is approximated by the GB potential, which is given by

$$U_{GB}(\mathbf{R}_{IJ},\mathbf{u}_I,\mathbf{u}_J) = 4\epsilon(\mathbf{e}_{IJ},\mathbf{u}_I,\mathbf{u}_J) \times [\mathcal{R}^{12} - \mathcal{R}^6],$$
$$\mathcal{R} = \frac{d_w\sigma_0}{|\mathbf{R}_{IJ}| - \sigma(\mathbf{e}_{IJ},\mathbf{u}_I,\mathbf{u}_J) + d_w\sigma_0}, \tag{3.27}$$

where σ and ϵ are the range parameter and the strength parameter, respectively. The range parameter describes the size and the shape of the ellipsoid and is determined by two variables l and d, which represent the length and the width of an ellipsoid, respectively. The strength parameter represents the interaction strength for different orientations and is determined by another two parameters ϵ_0 and $\frac{\epsilon_F}{\epsilon_S}$, which refer to the well-depth of cross configuration and the ratio between the well-depth of face-to-face configuration ϵ_F and that of side-to-side configuration ϵ_S, respectively[108]. The term d_w is introduced to control the "softness" of the potential[109]. Therefore, there are in total five parameters to fully specify a GB potential. The full expressions for σ and ϵ can be found in the Appendix.

The Gay-Berne force is computed from the gradient of the Gay-Berne potential and can be decomposed into the components along the direction of three non-orthogonal unit vectors $\mathbf{e}_{IJ}$, $\mathbf{u}_I$ and $\mathbf{u}_J$

$$\begin{aligned}\mathbf{F}_{GB}(\mathbf{R}_{IJ}, \mathbf{u}_I, \mathbf{u}_J) &= -\nabla U_{GB}(\mathbf{R}_{IJ}, \mathbf{u}_I, \mathbf{u}_J), \\ &= f_R \mathbf{e}_{IJ} + f_{u_I} \mathbf{u}_I + f_{u_J} \mathbf{u}_J,\end{aligned} \tag{3.28}$$

where f_R, f_{u_I}, f_{u_J} are the components of the total Gay-Berne force defined as

$$\begin{aligned} f_R &= -\frac{\partial U_{GB}}{\partial \mathbf{R}_{IJ}}, \\ f_{u_I} &= -\frac{\partial U_{GB}}{\partial (\mathbf{e}_{IJ} \cdot \mathbf{u}_I)}, \\ f_{u_J} &= -\frac{\partial U_{GB}}{\partial (\mathbf{e}_{IJ} \cdot \mathbf{u}_J)}. \end{aligned} \tag{3.29}$$

To extract five parameters at the same time is inefficient, a small deviation from the MD data can result in unstable parameterization. Therefore, a two-step parameterization was performed to extract the GB parameters as illustrated in fig.(3.8). I first considered each relative orientation $\Theta = \{\theta_\alpha, \theta_\beta, \theta_\gamma\}$ separately and extracted the corresponding parameters σ and ϵ. By fixing the relative orientation, the GB potential depends only on the pair distance $|\mathbf{R}_{IJ}|$. The GB force of a pair with fixed relative orientation is given by the gradient of the GB potential

$$\begin{aligned}\mathbf{F}_{GB}(\mathbf{R}_{ij}, \epsilon, \sigma) &= -\frac{dU_{GB}}{d|\mathbf{R}_{IJ}|} \\ &= -4\frac{\epsilon}{d_w \sigma_0}[12\mathcal{R}^{13} - 6\mathcal{R}^7].\end{aligned} \tag{3.30}$$

A set of σ and ϵ in terms of the relative orientation was obtained from the first parameterization. I utilized this data set of σ and ϵ to perform the second parameterization and extracted the GB parameters from the expression of σ and ϵ in Appendix.

Fig.(3.9) illustrates how the Lennard-Jones forces are approximated by the Gay-Berne force using the two-step parameterization, where I only present

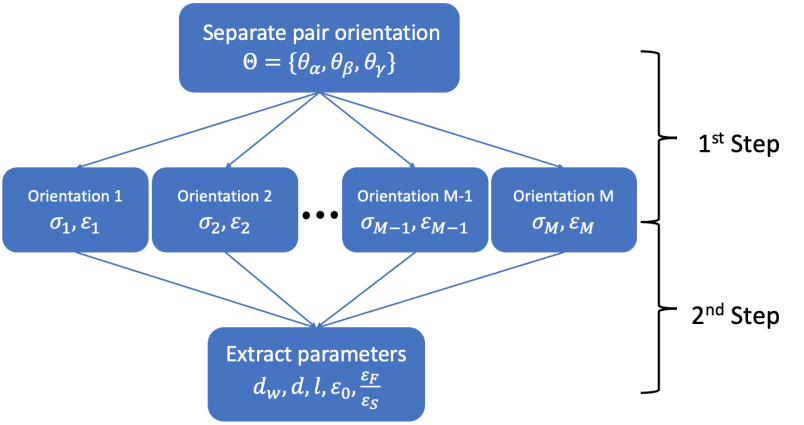

Figure 3.8.: Outline of two-step parameterization. The range parameter σ and strength parameter ϵ are optimized for each individual relative orientation $k = 1 \ldots M$ in the first step. The GB parameters, e.g., d, l, ϵ_0 and $\frac{\epsilon_F}{\epsilon_S}$ are parameterized from the data set of σ and ϵ in the second step.

the results of three relative orientations: face-to-face(FTF), side-to-side(STS) and T-shape, in the thesis. In the top panel, a set of σ and ϵ were obtained separately by fitting eq.(3.30) in the first parameterization. The data set of σ and ϵ to were then used to perform the second parameterization, such that the GB parameters d_w, d, l, ϵ_0 and $\frac{\epsilon_F}{\epsilon_S}$ were obtained by fitting the expression of σ and ϵ in Appendix, as shown in the middle panel. In the end, the fitting of the LJ force with the optimized GB parameters is presented in the bottom panel.

For the electrostatic interactions between the oblate ellipsoidal particles, the long-range electrostatic force is approximated by an electric multipole potential (EMP)[102, 110]. In order to replace the charge distribution of the molecule at the atomistic level, a multipole expansion is placed at the COM of particle. The potential energy between two multipole sites is given by a polytensor form[111]

$$U_{\mathrm{EMP}} = \mathcal{M}_i^t T_{ij} \mathcal{M}_j, \tag{3.31}$$

where

$$\mathcal{M} = [q, d_x, d_y, d_z, Q_{xx}, Q_{xy}, \ldots, Q_{zz}], \tag{3.32}$$

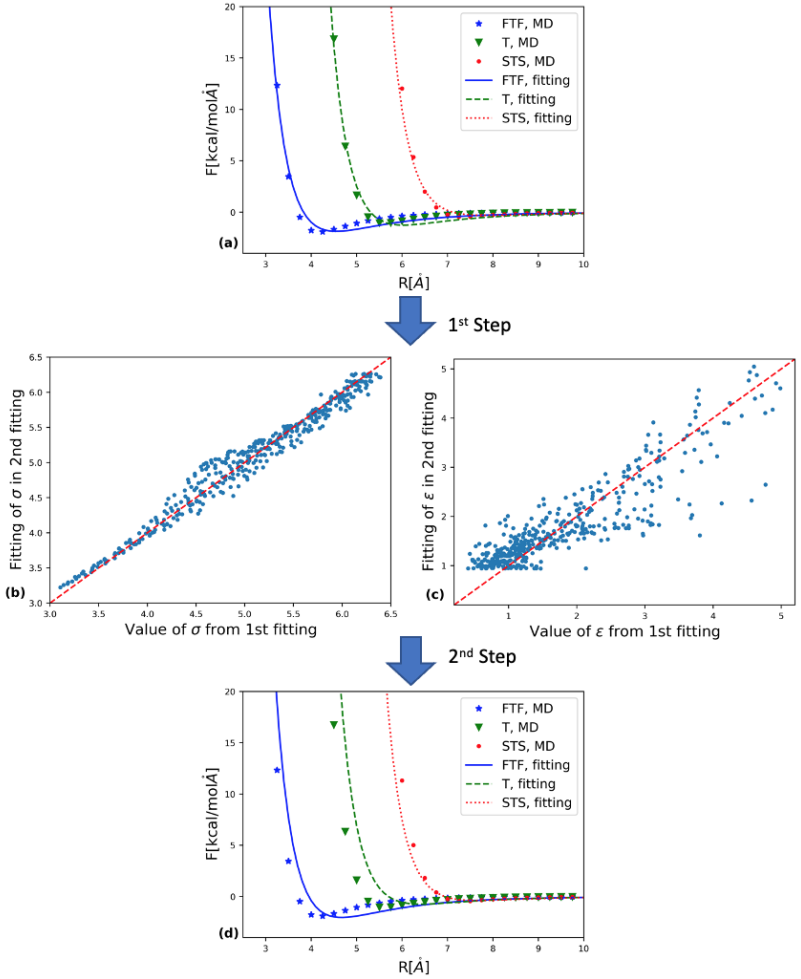

Figure 3.9.: The upper panel shows (a) the Lennard-Jones force $|\mathbf{F}_{LJ}|$ versus the pair distance $|\mathbf{R}_{IJ}|$ for fixed relative orientation in the first parameterization. The middle panel shows (b) the fitting of the range parameter σ and (c) the fitting of the strength parameter ϵ in the second parameterization. The bottom panel shows (d) the fitting of the Lennard-Jones force $|\mathbf{F}_{LJ}|$ versus the pair distance

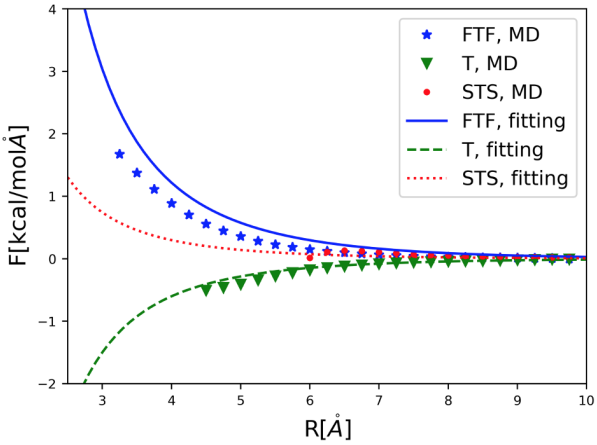

Figure 3.10.: The fitting of the electrostatic force $|\mathbf{F}_{EMP}|$ versus the pair distance

denotes that $\mathcal{M}, q, d, Q$ are multipole expansion, charge, dipole and quadrupole moments, respectively. For large separation, the multipole expansion can reproduce an accurate electrostatic potential. However, when the CG particles are close to each other, the point multipole expansion fails to accurately represent the actual overlap of charge distribution. This results in a penetration error. To address this, a damping function is employed to modify the short-range multipole[112]

$$\lambda = 1 - e^{-au^3}, \tag{3.33}$$

where $u = |\mathbf{R}_{IJ}|/(\alpha_i\alpha_j)^{1/6}$ is the effective separation between CG particles I and J, and α indicates the "size" of the particle. The factor a is a dimensionless parameter that controls the damping strength and was set to 0.49 in this thesis. To avoid the penetration error, the damping function modulates the regular formula of the multipole potential by replacing the point multipole with a smeared charge distribution. The electric multipole force of the ellipsoid pair is given by

$$\mathbf{F}_{\text{EMP}} = -\lambda\nabla U_{\text{EMP}}, \tag{3.34}$$

which is also orientation-dependent. The electrostatic force of the ellipsoidal pair is fitted by the electric multipole force as shown in fig.(3.10). The total pairwise conservative force between the CG particle is approximated by the

sum of the GB force and the electric multipole force, i.e. $\langle \mathbf{F}_{IJ} \rangle = \mathbf{F}_{GB} + \mathbf{F}_{\text{EMP}}$. Fig.(3.11) depicts the fitting result for the total pairwise conservative force.

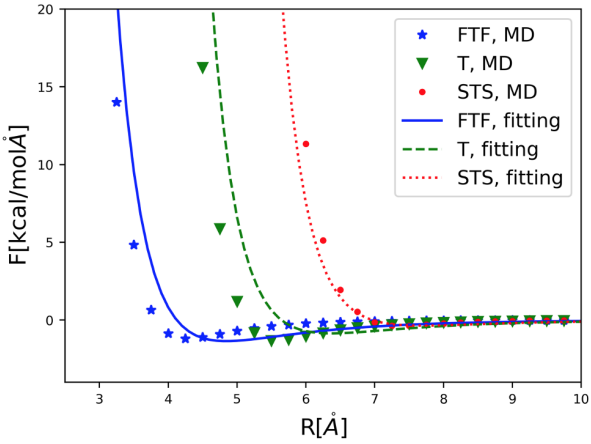

Figure 3.11.: The fitting of the total conservative force $\langle \mathbf{F} \rangle$ versus the pair distance

3.4.1.3. Construction of non-conservative force

In the MZ formalism, the non-conservative force recovers the missing degrees of freedom by an orthogonal operator Q. To construct the non-conservative forcefield, the fluctuating force on each CG particle is considered. To compute the magnitude of the fluctuating force $\delta F(\mathbf{R}_{IJ}, \mathbf{u}_I, \mathbf{u}_J)$, I employed the same binning method for the conservation force, where the distance bins and orientation bins are considered, as presented in the previous section.

Similar to the conservative forces, the components of the fluctuating forces along the direction of three non-orthogonal unit vectors $\mathbf{e}_{IJ}$, $\mathbf{u}_I$ and $\mathbf{u}_J$ are given by

$$\begin{aligned} \delta\mathbf{F}_{IJ}^{R} &= (\delta\mathbf{F}_{IJ} \cdot \mathbf{e}_{IJ})\mathbf{e}_{IJ}, \\ \delta\mathbf{F}_{IJ}^{u_I} &= (\delta\mathbf{F}_{IJ} \cdot \mathbf{u}_I)\mathbf{u}_I, \\ \delta\mathbf{F}_{IJ}^{u_J} &= (\delta\mathbf{F}_{IJ} \cdot \mathbf{u}_J)\mathbf{u}_I, \end{aligned} \tag{3.35}$$

respectively. The frictional tensor between CG particle I and J can be computed from the memory kernel which is determined by the time convolution of the fluctuating force[99], i.e.$\int_0^\infty \langle \delta\mathbf{F}_{IJ}(t)\delta\mathbf{F}_{IJ}(0)^T\rangle dt$. As a result, the frictional coefficients along three directions $\mathbf{e}_{IJ}$, $\mathbf{u}_I$ and $\mathbf{u}_J$ are computed from the components of the fluctuating force in eq.(3.35) and are given by

$$\begin{aligned}
\mathbf{\Phi}^R_{IJ}(\mathbf{R}_{IJ},\mathbf{u}_I,\mathbf{u}_J) &= \beta\int_0^\infty \langle \delta\mathbf{F}^R_{IJ}(\mathbf{R}_{IJ},\mathbf{u}_I,\mathbf{u}_J;t)\delta\mathbf{F}^R_{IJ}(\mathbf{R}_{IJ},\mathbf{u}_I,\mathbf{u}_J;0)^T\rangle dt,\\
\mathbf{\Phi}^{u_I}_{IJ}(\mathbf{R}_{IJ},\mathbf{u}_I,\mathbf{u}_J) &= \beta\int_0^\infty \langle \delta\mathbf{F}^{u_I}_{IJ}(\mathbf{R}_{IJ},\mathbf{u}_I,\mathbf{u}_J;t)\delta\mathbf{F}^{u_I}_{IJ}(\mathbf{R}_{IJ},\mathbf{u}_I,\mathbf{u}_J;0)^T\rangle dt,\\
\mathbf{\Phi}^{u_J}_{IJ}(\mathbf{R}_{IJ},\mathbf{u}_I,\mathbf{u}_J) &= \beta\int_0^\infty \langle \delta\mathbf{F}^{u_J}_{IJ}(\mathbf{R}_{IJ},\mathbf{u}_I,\mathbf{u}_J;t)\delta\mathbf{F}^{u_J}_{IJ}(\mathbf{R}_{IJ},\mathbf{u}_I,\mathbf{u}_J;0)^T\rangle dt.
\end{aligned} \tag{3.36}$$

In the integral, the correlation functions are integrated from time zero to infinity. In practice, Kirkwood introduced a cutoff upper limit t_0[113], which should be large enough to attain a plateau of the integral in eq.(3.36), but short enough that the correlation function does not decay appreciably to zero[114]. In this thesis, the upper time limit was set at $t_0 = 40fs$, where the plateau is attained as shown in fig.(3.12). As the distance and the relative orientation of the particle pairs change with time, I only considered the pairs that remain in the same distance bin and orientation bin over time, so that the ensemble averages of the fluctuating force expectation value over time can be computed.

In order to simplify the computation, the frictional tensor is assumed to be non-zero along only one direction. As a result, it can be reduced to a vector and decomposed into three components along $\mathbf{e}_{IJ}$, $\mathbf{u}_I$ and $\mathbf{u}_J$ directions

$$\mathbf{\Phi}_{IJ} = \varphi^R_{IJ}\mathbf{e}_{IJ} + \varphi^{u_i}_{IJ}\mathbf{u}_I + \varphi^{u_J}_{IJ}\mathbf{u}_J, \tag{3.37}$$

where the frictional coefficient along each direction can be expressed by the components

$$\begin{aligned}
|\mathbf{\Phi}^R_{IJ}| &= \varphi^R_{IJ} + \varphi^{u_I}_{IJ}\mathbf{e}_{IJ}\cdot\mathbf{u}_I + \varphi^{u_J}_{IJ}\mathbf{e}_{IJ}\cdot\mathbf{u}_J,\\
|\mathbf{\Phi}^{u_I}_{IJ}| &= \varphi^R_{IJ}\mathbf{e}_{IJ}\cdot\mathbf{u}_I + \varphi^{u_I}_{IJ} + \varphi^{u_J}_{IJ}\mathbf{u}_I\cdot\mathbf{u}_J,\\
|\mathbf{\Phi}^{u_J}_{IJ}| &= \varphi^R_{IJ}\mathbf{e}_{IJ}\cdot\mathbf{u}_J + \varphi^{u_I}_{IJ}\mathbf{u}_I\cdot\mathbf{u}_J + \varphi^{u_J}_{IJ}.
\end{aligned} \tag{3.38}$$

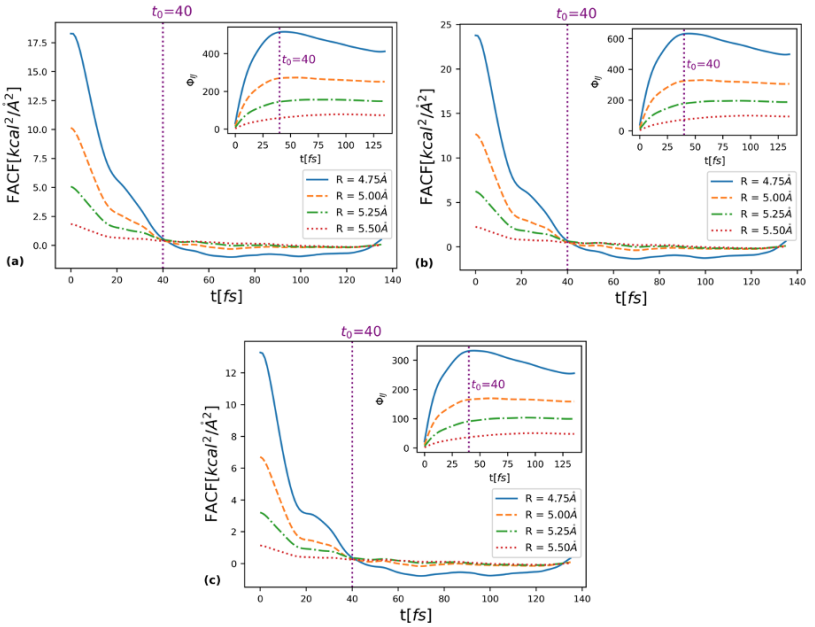

Figure 3.12.: Time correlations of the fluctuating force for one of the relative orientation, i.e. $\Theta = \{35^\circ, 45^\circ, 75^\circ\}$, along the direction of (a) the unit vector of the pair distance $\mathbf{e}_{IJ}$ (b) the normal vector of particle I $\mathbf{u}_I$ (c) the normal vector of particle J $\mathbf{u}_J$. The insets show the memory kernel along the specific direction.

The expressions of φ^R_{IJ}, $\varphi^{u_I}_{IJ}$ and $\varphi^{u_J}_{IJ}$ are presented in detail in the Appendix. By obtaining the value of the frictional coefficient components, The magnitude and direction of the frictional kernel can be computed and the dissipative force between the neighbouring CG particles can also be determined.

In order to approximate the frictional kernel, a modified repulsive Gay-Berne (mrGB) functional is proposed in this thesis, in which the attractive part of the GB functional form is removed and the repulsive part is modified to match the friction profile. Since the frictional force is always positive for all orientations, the attractive part of the regular GB potential is excluded in the mrGB functional. The power of the range parameter and the well-depth parameter are also adjusted based on the short-range and hard nature of the frictional force. As a result, the mrGB functional is able to describe the

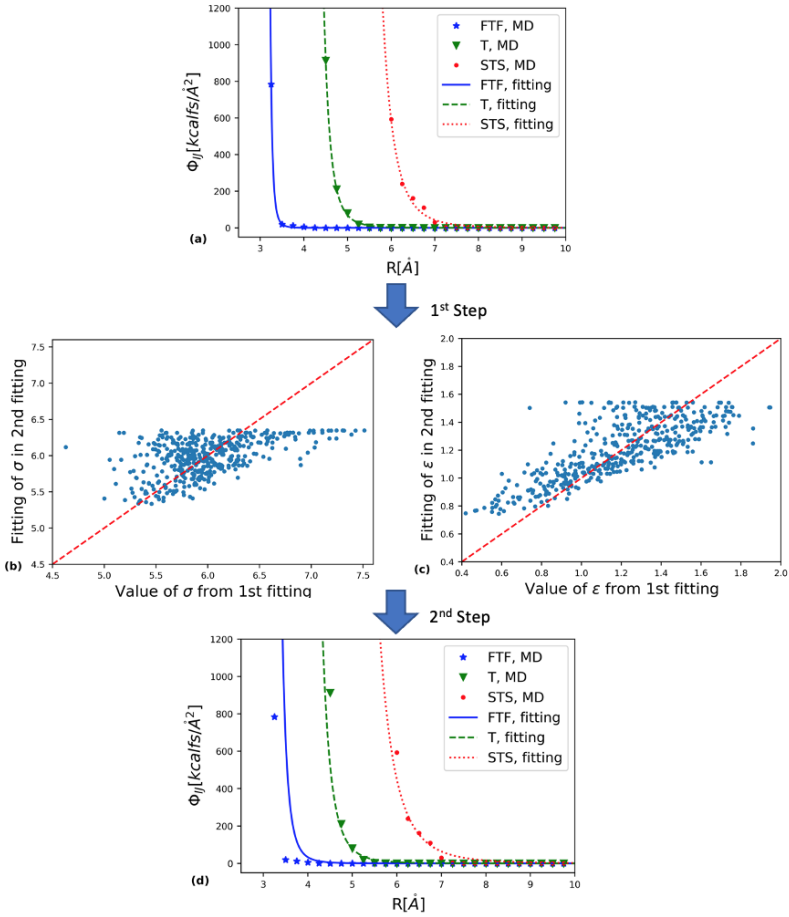

Figure 3.13.: (a) The top panel shows (a) the memory kernel $\mathbf{\Phi}_{IJ}$ versus the pair distance $|\mathbf{R}_{IJ}|$ for fixed relative orientation in the first parameterization. The middle panel shows (b) the fitting of the range parameter σ and (c) the fitting of the strength parameter ϵ in the second parameterization. The bottom panel shows (d) the fitting result of the memory kernel $\mathbf{\Phi}_{IJ}$ versus the pair distance $|\mathbf{R}_{IJ}|$

frictional interaction between the ellipsoidal particle pairs and is given by the form

$$U_{mrGB}(\mathbf{R}_{IJ}, \mathbf{u}_I, \mathbf{u}_J) = 4\epsilon^8(\mathbf{e}_{IJ}, \mathbf{u}_I, \mathbf{u}_J)) \times [(\frac{d_w}{|\mathbf{R}_{IJ}| - \sigma(\mathbf{e}_{IJ}, \mathbf{u}_I, \mathbf{u}_J) + d_w\sigma_0})^4], \tag{3.39}$$

and the frictional kernel is given by the gradient of the mrGB functional

$$\mathbf{\Phi}_{IJ}(\mathbf{R}_{IJ}, \mathbf{u}_I, \mathbf{u}_J) = -\nabla U_{mrGB}(\mathbf{R}_{IJ}, \mathbf{u}_I, \mathbf{u}_J). \tag{3.40}$$

Similar to the parameterization of the conservative forces, the two-step parameterization was employed to parameterize the frictional kernel. By fixing the relative orientation, the frictional kernel depends only on the pair distance

$$\mathbf{\Phi}_{IJ}(\mathbf{R}_{IJ}, \mathbf{u}_I, \mathbf{u}_J) = -\frac{\mathrm{d}U_{mrGB}}{\mathrm{d}|\mathbf{R}_{IJ}|} = -\frac{16\epsilon^8\mathcal{R}^5}{d_w\epsilon_0}. \tag{3.41}$$

The parameters σ and ϵ of frictional kernel were extracted for each relative orientation $\Theta = \{\theta_\alpha, \theta_\beta, \theta_\gamma\}$ in the first parameterization. Then a set of values of σ and ϵ for different relative orientation were employed to fit the range and the strength parameters σ and ϵ. The parameters of mrGB functional d_w, d, l, ϵ_0 and $\frac{\epsilon_F}{\epsilon_S}$ can be obtained by fitting σ and ϵ presented in the Appendix. The results of fitting the frictional kernel using the two-step parameterization are presented in fig.(3.13).

3.4.1.4. Mesoscopic model

For an anisotropic MZDPD particle, the fixed body-frame of the particle along its normal vector is considered. The rotational matrix $\mathbb{R}_i(t)$ represents a rotational transformation of the normal vector from fixed body-frame of particle I to the simulation box frame at time t. Given that the ellipsoidal particle has the semi-principal axes with length L_a, L_b and L_c, a shape matrix $\mathbf{S}$, which indicates the size and the shape of particle, and a quadratic form matrix $\mathbb{M}$ can be defined

$$\begin{aligned} \mathbf{S} &= diag(L_a, L_b, L_c), \\ \mathbb{M}_i &= \mathbb{R}_i^T \mathbf{S}_i^2 \mathbb{R}_i, \\ \mathbb{M}_j &= \mathbb{R}_j^T \mathbf{S}_j^2 \mathbb{R}_j. \end{aligned} \tag{3.42}$$

The time evolution of the angular motion of an ellipsoidal particle is governed by the angular equation of motion

$$\mathrm{d}\mathbf{L}_I/\mathrm{d}t = \sum_{i\neq j} \mathbf{T}_{IJ} = \sum_{i\neq j} \mathbf{G}_{IJ}\mathbf{R}_{IJ} \times \mathbf{F}^{\perp}_{IJ}, \tag{3.43}$$

where $\mathbf{T}_{ij}$ is the torque exerted on particle I by J and $\mathbf{F}^{\perp}_{IJ}$ is the component of the pairwise force acting on particle I by J perpendicular to the radial direction of two particles. $\mathbf{G}_{IJ}$ is a prefactor matrix that accounts for the contributions of the interacting particles with different sizes and shapes[106]. It is considered as a generalization of the scalar factor defined in the isotropic single-particle DPD method[115]. The prefactor matrix is defined as $\mathbf{G}_{IJ} = \mathbb{M}_i^{-1}(\mathbb{M}_i^{-1} + \mathbb{M}_j^{-1})^{-1}$, which satisfies the condition $\mathbf{G}_{IJ} + \mathbf{G}_{JI} = \mathbf{I}$. Moreover, the relative angular velocity $\mathbf{\Omega}_{IJ}$ between ellipsoidal DPD particles is given by

$$\mathbf{\Omega}_{IJ} = \boldsymbol{\omega}_I \times \mathbf{G}_{IJ}\mathbf{R}_{IJ} + \boldsymbol{\omega}_J \times \mathbf{G}_{JI}\mathbf{R}_{IJ}, \tag{3.44}$$

where $\boldsymbol{\omega}_I$ and $\boldsymbol{\omega}_J$ are the angular velocity of particle I and J, respectively.

The translational equation of motion governing the motion of an anisotropic MZDPD particle is given by

$$\begin{aligned}
\mathrm{d}\mathbf{P}_I/\mathrm{d}t = \sum_{J\neq I} \mathbf{F}_{IJ} = &\sum_{J\neq I} W_C(\mathbf{R}_{IJ}, \mathbf{u}_I, \mathbf{u}_J)\mathbf{e}^C_{IJ} \\
&+ \sum_{J\neq I} W_D^{\parallel}(\mathbf{R}_{IJ}, \mathbf{u}_I, \mathbf{u}_J)(\mathbf{e}_{IJ}\cdot\mathbf{V}_{IJ})\mathbf{e}_{IJ} \\
&+ \sum_{J\neq I} W_D^{\perp,V}(\mathbf{R}_{IJ}, \mathbf{u}_I, \mathbf{u}_J)[\mathbf{V}_{IJ} - (\mathbf{e}_{IJ}\cdot\mathbf{V}_{IJ})\mathbf{e}_{IJ}] \\
&+ \sum_{J\neq I} W_D^{\parallel}(\mathbf{R}_{IJ}, \mathbf{u}_I, \mathbf{u}_J)(\mathbf{e}_{IJ}\cdot\mathbf{\Omega}_{IJ})\mathbf{e}_{IJ} \\
&+ \sum_{J\neq I} W_D^{\perp,\Omega}(\mathbf{R}_{IJ}, \mathbf{u}_I, \mathbf{u}_J)[\mathbf{\Omega}_{IJ} - (\mathbf{e}_{IJ}\cdot\mathbf{\Omega}_{IJ})\mathbf{e}_{IJ}] \\
&+ \sum_{J\neq I} \frac{1}{\sqrt{3}}\sigma_{\parallel} W_R^{\parallel}(\mathbf{R}_{IJ}, \mathbf{u}_I, \mathbf{u}_J)\Delta t^{-1/2} tr\{d\mathbf{W}_{IJ}\}\mathbf{e}_{IJ} \\
&+ \sum_{J\neq I} \sqrt{2}\sigma_{\perp} W_R^{\perp,\Omega}(\mathbf{R}_{IJ}, \mathbf{u}_I, \mathbf{u}_J)\Delta t^{-1/2} d\mathbf{W}^A_{IJ}\mathbf{e}^{\perp}_{IJ},
\end{aligned} \tag{3.45}$$

where $\mathbf{e}_{IJ}^{C}$ is the unit vector of the conservative force acting on particle I by J in eq(3.28). W_C, W_D and W_R are the weighting functions of $\mathbf{F}_C$, $\mathbf{F}_D$ and $\mathbf{F}_R$, respectively:

$$\begin{aligned} W_C &= |\mathbf{F}_C|, \\ W_D^{\parallel} &= \mathbf{\Phi}_{IJ} \cdot \mathbf{e}_{IJ}, \\ W_D^{\perp,V} &= \mathbf{\Phi}_{IJ} \cdot \mathbf{e}_{IJ}^{\perp,V}, \\ W_D^{\perp,\Omega} &= \mathbf{\Phi}_{IJ} \cdot \mathbf{e}_{IJ}^{\perp,\Omega}, \end{aligned} \tag{3.46}$$

where $\mathbf{e}_{IJ}^{\perp,V} = \frac{\mathbf{V}_{IJ} - (\mathbf{e}_{IJ} \cdot \mathbf{V}_{IJ})\mathbf{e}_{IJ}}{|\mathbf{V}_{IJ} - (\mathbf{e}_{IJ} \cdot \mathbf{V}_{IJ})\mathbf{e}_{IJ}|}$ and $\mathbf{e}_{IJ}^{\perp,\Omega} = \frac{\mathbf{\Omega}_{IJ} - (\mathbf{e}_{IJ} \cdot \mathbf{\Omega}_{IJ})\mathbf{e}_{IJ}}{|\mathbf{\Omega}_{IJ} - (\mathbf{e}_{IJ} \cdot \mathbf{\Omega}_{IJ})\mathbf{e}_{IJ}|}$ are the unit vector of the perpendicular component of $\mathbf{V}_{IJ}$ and $\mathbf{\Omega}_{IJ}$ to the radial direction. The weighting function of conservative force W_C is the magnitude of conservative force. $W_D^{\parallel}$ is the weighting function of frictional force along radial direction, while $W_D^{\perp,V}$ and $W_D^{\perp,\Omega}$ are the weighting functions of frictional force perpendicular to radial direction, where they are not necessarily equal as their direction could be different. Similar to the isotropic model, the fluctuation-dissipation theorem requires the relation $\sigma_{\parallel} = \sigma_{\perp} = 2k_BT$ and relates the weighting functions of W_R to W_D, such that $W_R^{\parallel} = \sqrt{W_D^{\parallel}}$ and $W_R^{\perp,\Omega} = \sqrt{W_D^{\perp,\Omega}}$.

In contrast to the isotropic model, the EOM of the anisotropic model depends on both pair separation and relative orientation. The optimized parameters of the AMZDPD model are shown in Table(A.1) in the Appendix. The results are presented and analysed in the next section.

3.4.2. Performance of the model

In this section, I present and discuss the simulation results of the anisotropic dissipative particle dynamics model via the MZ formulation (AMZDPD), employing benzene as an example. The results of the AMZDPD model is compared with the reference atomistic molecular dynamics and also other coarse-graining methods, e.g., Martini 3[116], isotropic Mori-Zwanzig dissipative particle dynamics (MZDPD)[100] and Gay-Berne coarse-graining(GB-CG)[102, 103], to illustrate that the AMZDPD model yields a better performance in terms of both static and dynamical properties. The simulation for

all models were performed with 1000 benzene molecules in 0.1ns, and the computational speeds are shown in table(3.1).

Table 3.1.: Computational speed of different models for 1000 benzene in 0.1ns

Models	CPU time (second)
Atomistic MD	7817.22
Martini 3	108.66
MZDPD	76.63
GB-CG	102.05
AMZDPD	276.03

Martini3 is a CG forcefield which is widely used in biomolecular simulations. Martini employs a four-to-one mapping scheme (on average four heavy atoms and associated hydrogen atoms are mapped into one CG bead), and is parameterized using a mixed top-down and bottom-up strategy by matching the thermodynamic partitioning data. Non-bonded interactions between the neutral beads in Martini are only described by the Lennard-Jones potentials, while the charged beads include the Coulomb interactions. For an aromatic ring compound, such as benzene, 2-to-1 atoms-to-bead mappings are employed in the Martini 3 model[117]. Benzene is described by a three-bead model, with each bead representing the two consecutive carbon atoms and the associated hydrogen atoms. Based on the top-down approach, a bond length of 0.29nm is used, resulting in a mass density for liquid benzene of $0.890 gcm^{-3}$, which is in a good agreement with the experimental value of $0.877 gcm^{-3}$.

The isotropic Mori-Zwanzig Dissipative particle dynamics (MZDPD) is a bottom-up coarse-graining approach that constructs mesoscopic forcefield directly from the microscopic dynamics. By grouping a cluster of atoms into a spherical CG particle, the interactions between the neighbouring clusters are computed. Based on the MZ formalism, the effective dynamics of the mesoscopic system is projected directly from the underlying atomistic dynamics. Since MZDPD employs spherical representation, the conservative and the non-conservative interactions are only distance-dependence. The inclusion of the anisotropy is the main difference between the MZDPD and AMZDPD model.

Gay-Berne coarse-graining(GB-CG) is a bottom-up force matching method[103] that treats molecules as soft uniaxial ellipsoidal particles interacting via a

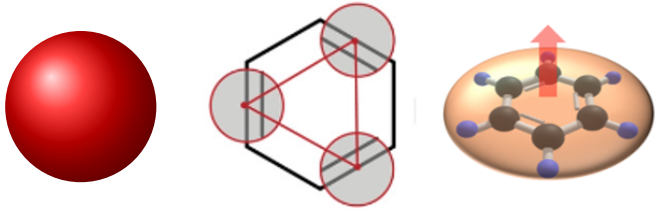

Figure 3.14.: Schematic diagram of the mapping scheme of different CG models to coarse-grain a benzene molecule: MZDPD employs spherical representation, Martini3 uses 2-to-1 atoms-to-bead mappings, and GB-CG and AMZDPD employ oblate ellipsoidal CG bead.

generalized anisotropic GB potential[101]. The CG potential parameters are extracted by comparing the cluster COM trajectories with the underlying atomistic trajectories. For each snapshot, the interacting force between the ellipsoid particle pairs was computed in terms of the separation and relative orientation. The conservative force is parameterized in the same way as the AMZDPD model by evaluating the potential of mean force from ensemble averages. The difference between GB-CG and AMZDPD is that the dynamics of GB-CG is determined by the Nosé–Hoover thermostat, whereas that of AMZDPD is determined by the non-conservative forces, which compensate the missing degrees of freedom during coarse-graining.

3.4.2.1. Static properties

In order to assess the performance of static properties of a CG model, the radial distribution functions (RDF) is used to analyse the local structure of benzene melt by comparing with the reference atomistic MD. The RDF is defined as

$$g(R) = \frac{P(R)}{n(R)}, \tag{3.47}$$

where $P(R)$ is the probability to find another molecule at a distance R, and $n(R)$ is normalization factor such that the RDF becomes 1 for large separations in a homogeneous system.

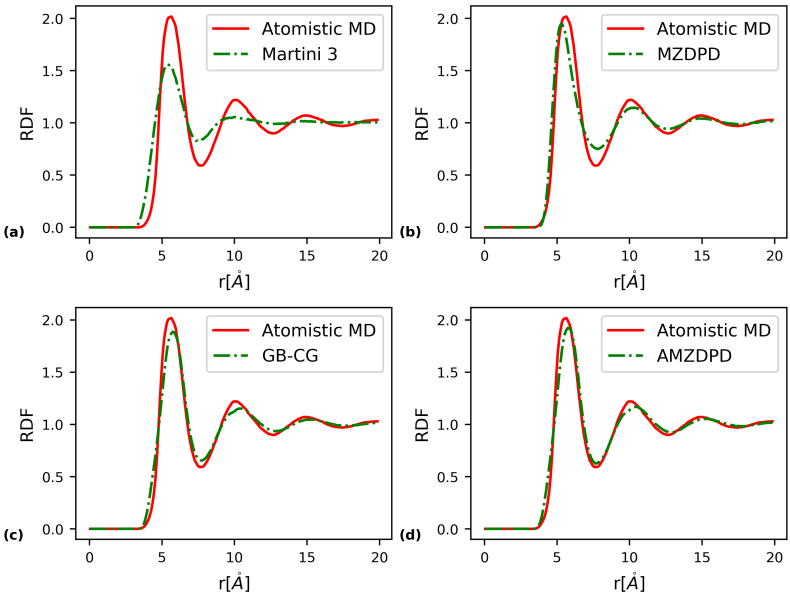

Figure 3.15.: The radial distribution function (RDF) of (a) Martini3 (b) isotropic dissipative particle dynamics via Mori-Zwanzig formalism(MZDPD) (c) Gay-Berne coarse grained(GB-CG) (d) anisotropic dissipative particle dynamics via Mori-Zwanzig formalism (AMZDPD) in comparison with the MD result

The results for the RDF of the different CG methods are shown in fig.(3.15). The RDF result of Martini 3 is depicted in fig.(3.15a), which shows a less structured local environment than the atomistic MD. Since the benzene molecule is represented by three spherical CG particles in the Martini3 model, this mapping scheme is not flexible enough to adjust the length or the width of the molecule separately. When the radius of the CG bead is increased, the width and length of molecule are both increased. The interaction strength of face-to-face or side-to-side orientation are closely related to the size and also not flexible to adjust independently. Furthermore, the Martini3 parameters are extracted using the top-down approach, there is no direct correlation between the forcefield and local environment structure. Due to the inaccurate representation of the size, the shape and the corresponding interaction strength, Martini3 has shifted peaks in the RDF and the intensity of the peaks is also much reduced.

Fig.(3.15b) depicts the RDF result of MZDPD. As the parameters of the MZDPD model are extracted from the bottom-up force-matching approach, the structure of the RDF curve of the MZDPD improves. This allows the forcefield to capture the atomistic details directly and more accurately reproduce the local structure. However, since the MZDPD model uses spherical representation, the anisotropic details of the CG particles are completely lost. For example, the face-to-face and the side-to-side orientation are different in the atomistic scale, but MZDPD is unable to distinguish the differences, resulting in significant error due to the information loss.

In fig.(3.15c), the RDF of GB-CG model shows more accurate results for both peak position and intensity. GB-CG possesses the flexibility to tune the parameters of the generalized anisotropic GB potential, which represents the length, width, and well-depth of the CG pairs, to approximate the potential of mean force. GB-CG can accurately describe the molecule's size, shape and interaction strength, and thus the local environment structures are reproduced as the atomistic details from the MD data are captured. However, as the interaction in CG level is generally softer, the empirical fitting approach results in a small but noticeable reduction in the peak intensity of the GB-CG model.

The RDF of the AMZDPD model is shown in fig.(3.15d). Since the frictional force and stochastic force in the AMZDPD affect only the dynamical properties, they do not contribute to the local structural properties. The conservative forcefield of AMZDPD and GB-CG implemented in this thesis are identical, therefore this gives the same RDF results for them. The small deviation between the AMZDPD and GB-CG model shown in the figure is due to the uncertainties, which can be minimized by taking more ensembles into account.

3.4.2.2. Dynamical properties

To assess the performance of dynamical properties of a CG model, the velocity auto-correlation function (VACF) is computed for the evaluation. VACF is a time-correlation function, which describes the dynamical correlation in molecular motion in liquids, and is very useful in both theoretical and experimental studies of dynamical and transport properties of liquids. The

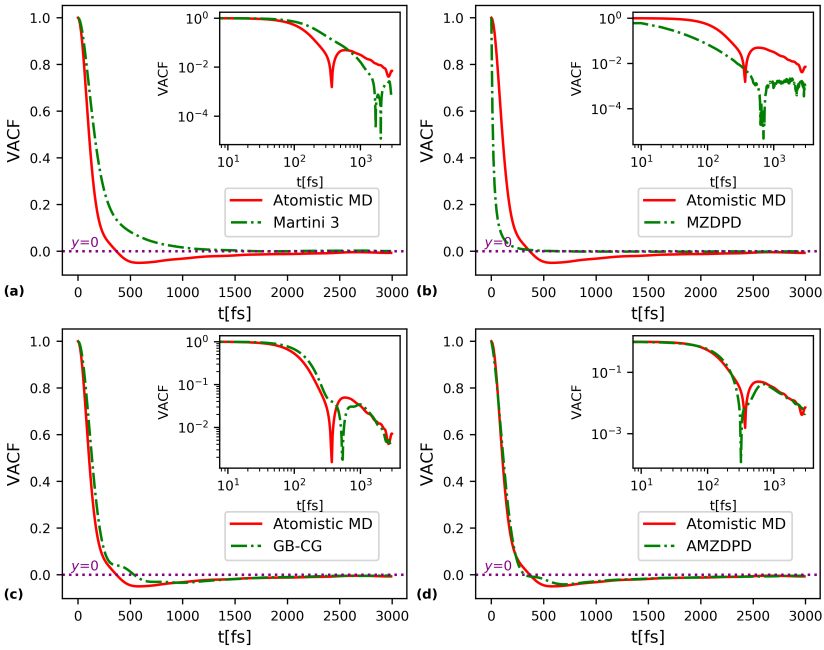

Figure 3.16.: The velocity auto-correlation function (VACF) of (a) Martini3 (b) isotropic dissipative particle dynamics via Mori-Zwanzig formalism (MZDPD) (c) Gay-Berne coarse grained(GB-CG) (d) anisotropic dissipative particle dynamics via Mori-Zwanzig formalism (AMZDPD) in comparison with the MD result

expression of the normalized VACF is given by the expectation value of the relative velocity of a particle pair separated by a time interval t

$$C_v(t) = \frac{\langle \mathbf{V}(t) \cdot \mathbf{V}(0) \rangle}{\langle \mathbf{V}(0) \cdot \mathbf{V}(0) \rangle}, \tag{3.48}$$

For short timescales, the particle exhibits ballistic behavior, where the VACF decays exponentially. For long timescales, the velocity of the particle pair decorrelates and the VACF eventually decays to zero. The oscillation of VACF results from the correlated motion of the particles when the particles are tightly packed.

The results of the VACF of all CG models and the reference MD are shown in fig.(3.16). Fig.(3.16a) shows the VACF results of Martini3, which illustrates

large differences between Martini 3 and the reference MD. The main difference is that there is no negative region in the Martini3 VACF curve. The negative value of VACF indicates a persistent tendency of the diffusing molecules to invert their direction of motion and remain localized. In contrast to the reference MD, the CG benzene pair in Martini3 shows a higher tendency to diffuse away from one another instead of oscillating in the local region. The error of Martini 3 in dynamical behaviour could be due to a too soft potential. The inaccurate description of the CG potential, in particular the interaction strength, in Martini3 results in too soft interactions between the benzene pairs. When the molecules interact with a very soft environment, they would easily diffuse away from the local region. As a result, there is a significant error in the dynamical behaviour for the Martini3 model.

The VACF result of MZDPD is depicted in fig.(3.16b), where it still shows a clear differences with the reference MD. For the VACF curve of MZDPD, it decays rapidly in short time and this indicates that the frictional force is too strong. Since the MZDPD employs a spherical representation, the CG particles lose the anisotropic properties. In an anisotropic system, particles are able to rotate until reaching an energetically favourable orientation. However, an isotropic system, like MZDPD model, does not possess this anisotropic property and instead averages the ensembles of all orientations. As the MZDPD averages of all possible orientation of a spherical particle pair, the particle experiences a stronger frictional force. As a result, the velocity of the CG particle pair decorrelates very quickly and there is also no negative region in the MZDPD's VACF curve. Without the orientation-dependence, the MZDPD model exhibits significant deviation in the dynamical behaviour.

The VACF of the GB-CG in fig.(3.16c) shows a better agreement with the dynamical behaviour of the reference MD , where the negative region in the VACF is presence. Since the potential of the GB-CG is constructed directly from the atomistic trajectories, the interaction strength is more accurately described and the potential of GB-CG is relatively harder than that of Martini3. Moreover, the frictional force in the GB-CG is softer than that of the MZDPD by introducing the anisotropy into the system. However, there are still errors in the dynamical behaviour between the GB-CG and the reference MD, especially in the short-time regime, where the GB-CG's VACF decays much slower and reaches a less negative minimum compared to the reference MD. The slow decay in the VACF curve indicates the change of particle's velocity is small, which implies the CG particle experiences less frictional force to hinder its motion. Since the GB-CG simulation is performed in the

NVT ensemble, each atom is coupled to a heat bath with a fluctuating term and a frictional term to maintain the system's temperature. As a result, the dynamical behaviour in the GB-CG does not capture directly from the microscopic system, resulting in an inaccurate description of the dynamical motion in the GB-CG model.

Among the CG models, the AMZDPD shows the best results and is in good agreement with the reference MD simulation, as shown in fig.(3.16d). The AMZDPD model projects the fast degrees of freedom in the microscopic system systematically into the dissipative and the stochastic term of the non-conservative forcefield at the CG level. Therefore, the model is able to reproduce the dynamical behaviour in the short time regime. Yet, there is a deviation in the minimum of the VACF curve. This suggests the CG forcefield is softer than that of the reference MD, which results in a weaker backscattering effect.

In order to analyse the dynamical performance of CG methods with respect to a physical observable, the diffusion constant D is computed from the non-normalized VACF via the Green-Kubo relations

$$D = \frac{1}{3}\int_0^\infty \langle \mathbf{V}(t) \cdot \mathbf{V}(0) \rangle dt. \tag{3.49}$$

Using the VACF data, the diffusivity can be computed in both atomistic MD and CG methods. The results are presented in fig(3.17). The diffusivity curves converge in long time limit and this gives the diffusion constant value for different models. As shown in table(3.2), the AMZDPD model gives the value of 2.28 which is the method that comes closest to the MD value 2.20 with a error of 3.6%. This is also consistent with the VACF result, where the AMZDPD model outperforms all other CG methods used in this thesis.

Table 3.2.: Diffusion constant of different models

Model	Diffusion constant D (error %)
Atomistic MD	2.20
Martini 3	7.41(+237)
MZDPD	0.99(-55)
GB-CG	4.35(+97.7)
AMZDPD	2.28(+3.6)

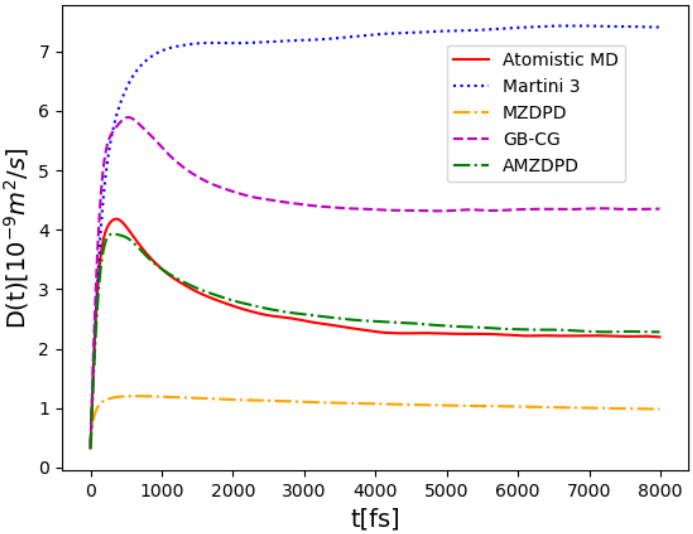

Figure 3.17.: Diffusivity value of different CG methods in comparison with the MD result

4. Simulation of mesoscopic phenomena in soft matter

Mesoscopic phenomena refer to phenomena that occur at a spatio-temperal scale ranging from $10-10^4$nm and $1-10^6$ns. At this scale, both microscopic and macroscopic features play significant roles, making modelling of mesoscopic phenomena is highly challenging. In the previous chapter, the MZDPD model was introduced to simulate mesoscopic phenomena, where it is able to capture the atomistic details and reproduce consistent dynamical properties. Apart from the MZDPD model, atomistic MD and continuum model can be applied to qualitatively model particular mesoscopic systems using specific schemes. In this chapter, I will present three examples of the mesoscopic phenomena simulation using three different models: the AMZDPD model discussed in ch.(3); a continuum model; and an atomistic MD.

4.1. Crystallization of pentacene

Crystallization of organic molecules is an important mesoscopic phenomena in organic material production and has attracted interest from various fields such as organic electronics[35, 118] and pharmaceutical research[119, 120]. Crystallization is a process based on the molecular self-assembly, where the components spontaneously form ordered aggregates[34]. Self-assembly is scientifically important as it enables the formation of complex structures in biological system[121], including lipid membranes, structured nucleic acids, and folded proteins, and the formation of regular structures for various materials, such as molecular crystals[122] and liquid crystals[123].

Organic semiconductors (OSC) are vital for the production of high-performance organic electronic devices in organic electronics. Specifically, organic thin-film transistor(OTFT) is a key component that utilize an electric field to control

the current across a semiconductor thin film[124, 125]. To fabricate OTFT, OSCs are deposited on a substrate and then crystallized to form the organic thin film. To understand the crystallization of organic molecules, numerous studies have been carried out [120, 126]. Moreover, atomistic MD simulations have been employed to study the order-emerging stage of crystallization in the solution of pentacene and its derivatives[118].

However, crystallization is a mesoscopic behaviour, in which the scales of the self-assembly process could range from nanometers to micrometers. Atomistic MD enables the study of self-assembly mechanism at molecular level, but it is computationally demanding for it to analyze the effects of crystallization on a larger scale. Moreover, the anisotropic effect is eliminated in most CG models, the crystallization of CG particles has not yet been achieved. Here, the system of pentacene is considered, and the AMZDPD approach presented in ch.(3) is employed to study the self-assembly and crystallization of pentacene at the CG level.

4.1.1. Anisotropic CG model for pentacene

In the previous chapter, the AMZDPD model was demonstrated using benzene as an example. Benzene is a molecule that is symmetric along the plane vector, such that the orientation of the CG benzene is characterized only by the plane vector. However, pentacene molecule has three principal axes with different lengths. As a result, the anisotropic model is reformulated to describe the dissimilar ellipsoidal CG particle, which is characterized by three principal semi-axes of length L_a, L_b and L_c, as shown in fig.(4.1).

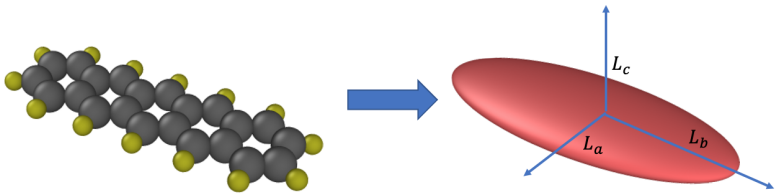

Figure 4.1.: Schematic diagram of coarse-graining a pentacene molecule, in which a pentacene is represented by a dissimilar ellipsoidal CG particle with principal semi-axes of length L_a, L_b and L_c.

The Lennard-Jones interaction between the dissimilar ellipsoidal CG particles[127] is rewritten as

$$U_{GB}(\mathbb{R}_I, \mathbb{R}_J, \mathbf{R}_{IJ}) = U_r(\mathbb{R}_I, \mathbb{R}_J, \mathbf{R}_{IJ}, \gamma) \cdot \eta(\mathbb{R}_I, \mathbb{R}_J) \cdot \chi(\mathbb{R}_I, \mathbb{R}_J, \mathbf{R}_{IJ}), \tag{4.1}$$

where $\mathbb{R}_I$ and $\mathbb{R}_J$ are the rotational transformation from the simulation box frame to the body frame of the CG particle, η and χ are two orientation-dependent functions, and U_r is the shifted distance dependent interaction which is given by

$$\begin{aligned} U_r(\mathbb{R}_I, \mathbb{R}_J, \mathbf{R}_{IJ}, \gamma) &= 4\epsilon(\varrho^{12} - \varrho^6), \\ \varrho &= \frac{\sigma}{h_{IJ}(\mathbb{R}_I, \mathbb{R}_J, \mathbf{R}_{IJ}) + \gamma\sigma}, \end{aligned} \tag{4.2}$$

where ϵ is the effective interaction strength, σ is the minimum effective particle radii, $h_{IJ}(\mathbb{R}_I, \mathbb{R}_J, \mathbf{R}_{IJ})$ is the distance of closest approach between the two particles, and γ is the shift parameter.

The first orientation-dependent function η is defined as

$$\begin{aligned} \eta &= [\frac{2s_I s_J}{\det(\mathbb{G}_{IJ})}]^{1/2}, \\ s &= (L_a L_b + L_c L_c)(L_a L_b)^{1/2}, \end{aligned} \tag{4.3}$$

where $\mathbb{G}_{IJ}$ is the sum of the form matrix in eq.(3.42), i.e. $\mathbb{G}_{IJ} = \mathbb{M}_I + \mathbb{M}_J$. A relative energy matrix $\mathbb{E} = diag(\epsilon_a^{-1/2}, \epsilon_b^{-1/2}, \epsilon_c^{-1/2})$ represents the relative interaction strength, i.e. ϵ_a, ϵ_b, ϵ_c, with respect to the orientation along the principal semi-axes. The second orientation-dependent function χ is given by

$$\begin{aligned} \chi &= [2\mathbf{e}_{IJ}\mathbb{B}_{IJ}^{-1}\mathbf{e}_{IJ}]^2, \\ \mathbb{B}_{IJ} &= \mathbb{R}_I^T\mathbb{E}_I\mathbb{R}_I + \mathbb{R}_J^T\mathbb{E}_J\mathbb{R}_J = \mathbb{B}_I + \mathbb{B}_J, \end{aligned} \tag{4.4}$$

where $\mathbf{e}_{IJ}$ is the unit vector of the radial distance between particle I and J.

Moreover, due to the quadrupole moment of the pentacene molecule, the electrostatic interaction between dissimilar ellipsoidal CG particles is given by

$$U_{emp} = \frac{\sum_{ij} Q_{I,ij}\mathbf{e}_{IJ,i}\mathbf{e}_{IJ,j} \sum_{i'j'} Q_{J,i'j'}\mathbf{e}_{IJ,i'}\mathbf{e}_{IJ,j'}}{|\mathbf{R}_{IJ}|^5}, \tag{4.5}$$

where $Q_{I,ij}$ and $Q_{J,ij}$ are the elements of the quadrupole moment tensor of particle I and J with the Cartesian components i and j, i.e. $i, j = x, y, z$.

Similarly, the modified GB functional that describes the frictional interaction between the dissimilar ellipsoidal CG particles is rewritten as

$$\begin{gathered} U_{mrGB}(\mathbb{R}_I, \mathbb{R}_J, \mathbf{R}_{IJ}) = U_f(\mathbb{R}_I, \mathbb{R}_J, \mathbf{R}_{IJ}, \gamma) \cdot \eta(\mathbb{R}_I, \mathbb{R}_J) \cdot \chi(\mathbb{R}_I, \mathbb{R}_J, \mathbf{R}_{IJ}), \\ U_f(\mathbb{R}_I, \mathbb{R}_J, \mathbf{R}_{IJ}, \gamma) = 4\epsilon\varrho^8, \end{gathered} \tag{4.6}$$

where the functional U_f is modified to match the profile of the frictional interaction as presented in the previous chapter. As a result, the equation of motion for the dissimilar ellipsoidal CG particles is given by eq.(3.45). The main difference between this model and the model presented in ch.(3)is the expression of the fitting function. Since the dissimilar ellipsoidal CG particles have principal semi-axes with different lengths, the fitting function used in this model has additional parameters to accurately capture the anisotropic behaviour of the dissimilar ellipsoidal particles.

4.1.2. Parameterization of the CG model

To parameterize the pentacene system in the AMZDPD model, I followed the procedure in ch.(3), where the conservative force and dissipative force are extracted from the MD trajectories and then approximated using force-matching approach. In order to extract the atomistic information of a pentacene system, an all-atom MD simulation with 400 pentacene molecules was performed. The forcefield parameters were obtained from the GROMOS forcefield[128] and the cutoff of both Lennard-Jones potential and Coulomb potential are $12\mathring{A}$. The simulation was performed in a periodic simulation box with a length of $52.20\mathring{A}$, resulting in a density of $1.3g/cm^3$. NVT simulations were performed to generate the MD trajectories, which were then used to extract the atomistic data of the system and construct the CG forcefield.

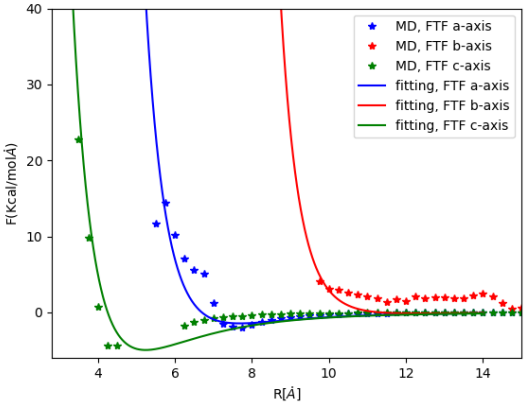

Figure 4.2.: Results of fitting the conservative force between pentacene pair with the sum of the GB force and the quadrupole interaction

The average force was computed in terms of the pair separation and related orientation using the binning method. As the dissimilar ellipsoidal CG particles lack symmetry, the relative orientation between a pair is more complex than the oblate ellipsoidal pair. In this thesis, only the face-to-face and T-shape configurations are considered in the parameterization procedure. The conservative forcefield for the dissimilar ellipsoidal CG particles was then approximated by the sum of the gradient of the GB potential in eq.(4.1) and the quadrupole potential in eq.(4.5). The fitting results of the conservative force are presented in fig.(4.2).

I also followed the parameterization procedure for the non-conservative forcefield presented in the last chapter. The memory kernel was computed using the time correlations of the fluctuating force in terms of the pair separation and relative orientation. To obtain the frictional coefficient, the integration of the correlation function was computed with an upper time cutoff of $60fs$. The frictional coefficient was then approximated by the gradient of the modified GB functional in eq.(4.6). The fitting results of the frictional kernel are shown in fig.(4.3). The optimized parameters for the pentacene molecule in the AMZDPD model can be found in the table(A.2) in the Appendix.

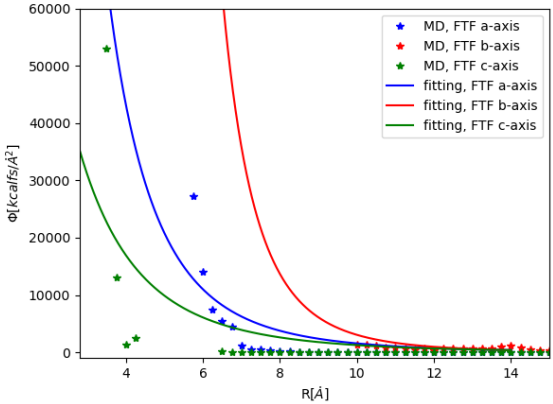

Figure 4.3.: Results of fitting the frictional coefficient between pentacene pair with the modified GB functional

4.1.3. Self-assembly of dissimilar ellipsoidal CG particles

In order to quantify the degree of crystallization of a pentacene system, two order parameters are considered: the second-rank orientational order parameter $\langle P_2 \rangle$, also called the nematic order parameter, and the herringbone order parameter $\langle S_h \rangle$[129].

$\langle P_2 \rangle$ indicates the long-range orientational order of the molecular structure along a specific direction. It is calculated using the order parameter tensor T, which is commonly used to study the order of nematic liquid crystals

$$T_{\alpha\beta} = \frac{1}{2N} \sum_{i}^{N} (3e_{i\alpha}e_{i\beta} - \delta_{\alpha\beta}), \tag{4.7}$$

where $e_{i\alpha}$ and $e_{i\beta}$ are the unit vectors of the principal axis of ellipsoid i in the simulation box frame, i.e. $\alpha, \beta = a, b, c$. By considering all ellipsoidal particles in the system, T can be computed, and the value of the order parameter $\langle P_2 \rangle$ is obtained from its largest eigenvalue. $\langle P_2 \rangle = 1$ indicates perfectly aligned vectors, while $\langle P_2 \rangle = 0$ implies random orientations.

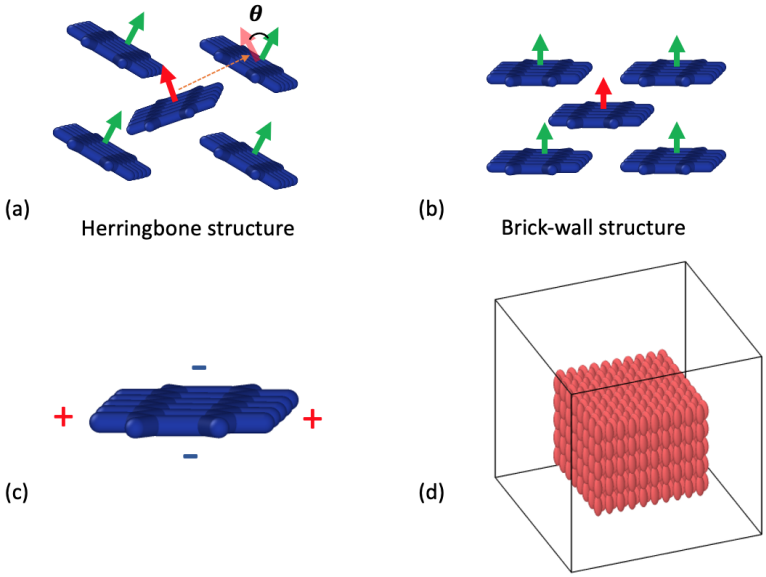

Figure 4.4.: Schematic diagram of (a) the herringbone structure of the perfect pentacene crystal (b) the brick-wall structure formed using the AMZDPD model (c) the quadrupole moment of the pentacene molecule (d) the pentacene crystal with herringbone structure used as the initial configuration in the simulation.

$\langle S_h \rangle$ indicates the short-range order of the herringbone structure in a local region

$$S_h(\theta) = \frac{1}{4} \sum_{i=1}^{4} sin\theta_{i0}, \tag{4.8}$$

where θ is the herringbone angle between the π-plane (c-axis) of a central molecule and the π-plane of the neighbouring molecules, as shown in fig.(4.4). To compute the herringbone order parameter, four nearest neighbouring molecules are chosen within a cutoff distance of $6\mathring{A}$ from the central molecule. When S_h=1, it indicates a perfect T-shape structure, whereas S_h=0 indicates a π-stacking structure.

For a perfect pentacene crystal, the pentacene molecules form the herringbone structure with herringbone angle of 51.3°, resulting in a value of $\langle S_h \rangle$=0.781. Moreover, the value of the long-range order parameter $\langle P_2 \rangle$ along the a-axis

is $\langle P_a \rangle$ = 0.632 and along the b-axis is $\langle P_b \rangle$ = 0.996. In the simulation, the system started with an initial configuration of a perfect pentacene crystal with herringbone structure. If the herringbone structure remains throughout the simulation, it indicates the crystal structure is energetically favourable and the crystallization of the CG pentacene is achieved. Otherwise, the AMZDPD model fails to reproduce the crystallization of pentacene if the crystal melts throughout the simulation.

The results of the crystallization of CG pentacene is presented in fig.(4.5). Fig.(4.5a) shows the change of the order parameters over time and fig.(4.5b) shows the energy function of two CG pentacene in the FTF and T-shape configuration with varying distance. Since the FTF configuration has a lower energy minimum than the T-shape configuration, it is more energetically favourable. As a result, in the simulation, $\langle S_h \rangle$ decreases to near zero, and both $\langle P_a \rangle$ and $\langle P_b \rangle$ increase to near one. This indicates that the herringbone structure of the pentacene crystal is destroyed, and the CG pentacene molecules rotate and rearrange to the FTF configuration, which is the lowest energy state. As a result, the CG pentacene molecules self-assemble to form the brick-wall structure instead of the herringbone structure.

The lowest energy state of the Gay-Berne interaction is the FTF configuration, whereas that of the quadrupole interaction was the T-shape configuration. As a result, the formation of the brick-wall structure in the simulation is due to the dominance of the Gay-Berne interaction. In order to make the quadrupole interaction dominant over the Gay-Berne interaction, the quadrupole interaction is increased. Fig.(4.5c) and fig.(4.5d) show the change of the order parameters over time and the energy function of the FTF and T-shape configurations after increasing the quadrupole interaction by a factor of 10. Although the quadrupole interaction is ten times stronger, the energy minimum of the FTF configuration is still lower than that of the T-shape configuration, as shown in fig.(4.5d). As a result, herringbone order parameter $\langle S_h \rangle$ in fig.(4.5c) is slightly higher than that in fig.(4.5a), but it is still close to zero. Therefore, the CG pentacene molecules still form the brick-wall structure even after increasing the quadrupole interaction by ten times.

Fig.(4.5e) and fig.(4.5f) depict the change of the order parameters over time and the energy function of the FTF and T-shape configuration after increasing the quadrupole interaction by a factor of 25. In fig.(4.5f), the T-shape configuration has a lower energy minimum than the FTF configuration. As a result, the herringbone order parameter $\langle S_h \rangle$ at T=0.5ns in fig.(4.5e) has a value of 0.290,

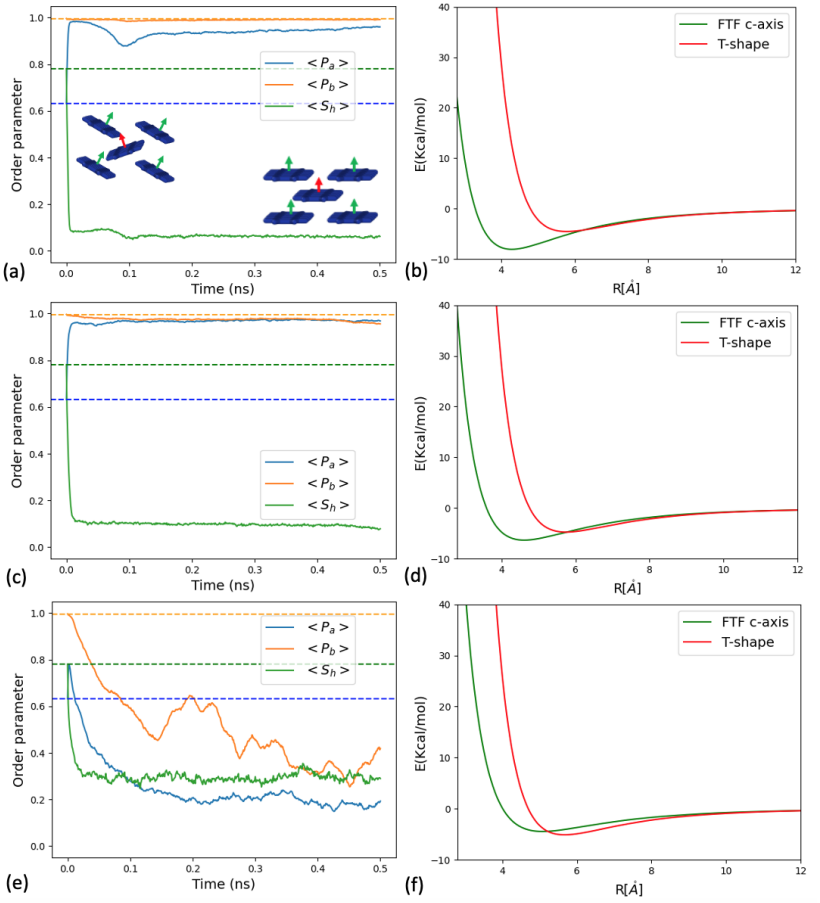

Figure 4.5.: The change of order parameters over time for the system with quadrupole interaction with factor of (a) 1, (c) 10, (e) 25. The dotted lines indicate the order parameters of a perfect pentacene crystal with herringbone structure, where $\langle S_h \rangle$=0.781, $\langle P_a \rangle$ = 0.632, $\langle P_b \rangle$ = 0.996. The energy function of the FTF and T-shape configuration for the system with quadrupole interaction with factor of (b) 1, (d) 10, (f) 25.

indicating that some CG pentacene molecules form the herringbone structure. However, more energy is introduced into the system when the quadrupole interaction increases, and excessive energy can destroy the crystal structure. As a result, long-range order parameters $\langle P_a \rangle$ and $\langle P_b \rangle$ decrease over time, indicating that the crystal melts.

In this section, the AMZDPD model developed in ch.(3) is applied to model the crystallization of pentacene using dissimilar ellipsoidal CG particles. To investigate the ability of the AMZDPD approach to simulate pentacene crystallization , the simulation started with a perfect pentacene crystal with the herringbone structure. If the AMZDPD approach fails to reproduce the crystallization, it would be indicated by the melting of the pentacene crystal. In the simulation, due to the dominance of the GB interaction over the quadrupole interaction, the CG pentacene molecules rearrange from the herringbone structure to the brick-wall structure. Increasing the quadrupole interaction allows some CG pentacene to form the local herringbone structures, but the long-range crystal structure is lost as excessive energy is introduced into the system. This indicates that the description of the GB interaction and quadrupole interaction in the AMZDPD model may not be accurate. The failure of the AMZDPD model in simulating pentacene crystallization could be attributed to the use of the GROMOS forcefield in the atomistic system, which does not account for the quadrupole moment of the pentacene molecule. Consequently, the construction of the mesoscopic system is based on an incorrect representation of the atomistic system. Despite the failure to accurately model the crystallization of pentacene, the AMZDPD model demonstrates the self-assembly of pentacene molecules to form a organized brick-wall structure at the CG level.

4.2. Deposition of polymer fiber in electrospinning

Nanoscale additive manufacturing(AM) is a method of fabricating complex nanoscale structures via self-assembly or directed assembly.[130–132]. Compared to conventional subtractive manufacturing methods, AM offers greater flexibility and programmability in fabricating complex structural architectures.[133]. As a result, AM has gained significant interests in various fields, such as sensors[134, 135], energy devices[136, 137], and biomedical applications[138–140]. There are several available additive nanomanufacturing

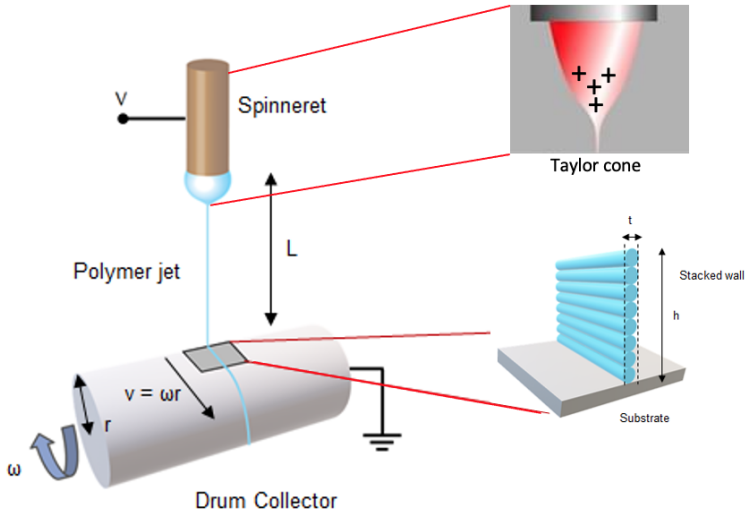

Figure 4.6.: Schematic diagram of the electrospinning experimental setup. The top right panel illustrates the formation of the Taylor cone. The bottom right panel shows the electrospinning fiber deposition (adapted from [144] with permission from the Wiley Online Library).

technologies, such as e-beam lithography[141], direct laser writing[142], and direct ink writing[143]. Among these options, near-field electrospinning (NFES) has emerged as a promising approach for rapid, scalable, and flexible fabrication of complex 3D structures with programmable properties.

Electrospinning[145, 146] is a continuous nanofiber production technique driven by an electric field between a metallic nozzle and a grounded substrate, as depicted in fig.(4.6). In this process, electric charges induced by the electric field accumulate on the surface of the droplet. The electric force pulling the charged droplet towards the substrate competes with surface tension, which tends to maintain its shape, resulting in the formation of Taylor cone[147]. When the electric force exceeds the surface tension, the surface of the droplet breaks and ejects an electrified thin jet. In conventional electrospinning, the nanofiber deposition is inaccurate due to the bending instability[148]. In order to improve the controllability of fiber collections, near-field electrospinning was developed by reducing the operating distance and applied electric field[149, 150]. Thus, the nanofibers can be precisely controlled by depositing them before the whipping motion.

NFES offers several advantages, including high speed (>20cm/s), high resolution (<100nm), and applicable to a wide range of materials such as polymers[151, 152], carbon[153, 154] and metal oxides[155, 156]. However, the major limitation of NFES is the accumulation of charges in the deposited fibers. During the fiber deposition, the in-flight fibers tend to stack on top of the deposited fibers in a self-aligned manner[157–159], enabling the formation of wall-like structures. When the charge dissipation is slow, the residual charges accumulate within the fibers. This can result in electric repulsion between fibers, limiting the self-alignment of the fibers and the effectiveness of the NFES process.

4.2.1. Continuum model for charge transport

In order to model the charge transport within the fiber of the NFES process, a charge transport model in a dielectric medium[160] is employed, in which the charge is transferred from the deposited fiber to the grounded substrate under an external electric field. The dielectric charge transport models have been used to study the dynamics of space charges in various dielectric materials, e.g. charge injection in dielectric thin film[161], polyethylene[162], and space charge accumulation in high voltage cable[163, 164].

Due to the symmetry along the radial direction, the charge transport is assumed to be only along the vertical z-direction, and thus a one-dimensional model is employed in this thesis, as presented in fig.(4.7a). Considering the 1D fiber has an infinitesimal small width dx and height h and is stacked on top of the deposited fiber wall for each deposition time t_d. The charge distribution of the 1D fiber is described by a Gaussian distribution

$$\rho(z) = \rho_0 e^{-\frac{1}{2}\left(\frac{z-(h-w)}{\sigma}\right)^2}, \tag{4.9}$$

where ρ_0 denotes a charge constant that determines the charge density of the fiber, w and σ denote the width and standard deviation of the Gaussian distribution, respectively.

As only one of the charge carriers is dominant in the electrified jet of NFES, only positive charge is considered in the charge transport model here. The following set of coupled equations describes the dynamics of the positive charge carriers in the deposited fibers:

1) Transport equation

$$\mathbf{J}(z,t) = \mu \mathbf{E}(z,t)\rho(z,t) - D\nabla\rho(z,t), \tag{4.10}$$

2) Continuity equation

$$\frac{\partial \mathbf{J}(z,t)}{\partial z} + \frac{\partial \rho(z,t)}{\partial t} = 0, \tag{4.11}$$

3) Poisson equation

$$\frac{\partial \mathbf{E}(z,t)}{\partial z} = \frac{\rho(z,t)}{\epsilon\epsilon_0}, \tag{4.12}$$

where $\mathbf{J}$ is the transport current, $\mathbf{E}$ is the electric field strength, ρ is the charge density, μ is the mobility of the charge carriers, D is the diffusivity of the charge carriers, ϵ is the dielectric constant, and ϵ_0 is the permittivity of vacuum. On the right-hand side of eq.(4.10), the first term and the second term corresponds to the drift flux and diffusion flux, respectively.

As illustrated in fig.(4.7b), charges can be stored in the trapped states of polymeric materials for a long time[36]. These trapped states are typically determined by the crystallinity[165], polymer structure[166], and the presence of additives[167]. In order to introduce the trapped and mobile states into the model, the total charge density is divided into trapped and mobile states

$$\rho = \rho_t + \rho_f, \tag{4.13}$$

where ρ_t is the charge density in the trapped states and ρ_f is the charge density in the mobile states. Furthermore, the source terms of the trapped states and the mobile states are given by

$$S_t = R_{f\to t}\rho_t(1 - \frac{\rho_t}{N_t}) - R_{t\to f}\rho_f, \tag{4.14}$$

$$S_f = -R_{f\to t}\rho_t(1 - \frac{\rho_t}{N_t}) + R_{t\to f}\rho_f, \tag{4.15}$$

where $R_{f\to t}$ is the rate of charge transfer from the mobile state to the trapped state, $R_{t\to f}$ is the rate of charge transfer from the trapped state to the mobile state, and N_t is the density of the trapped state.

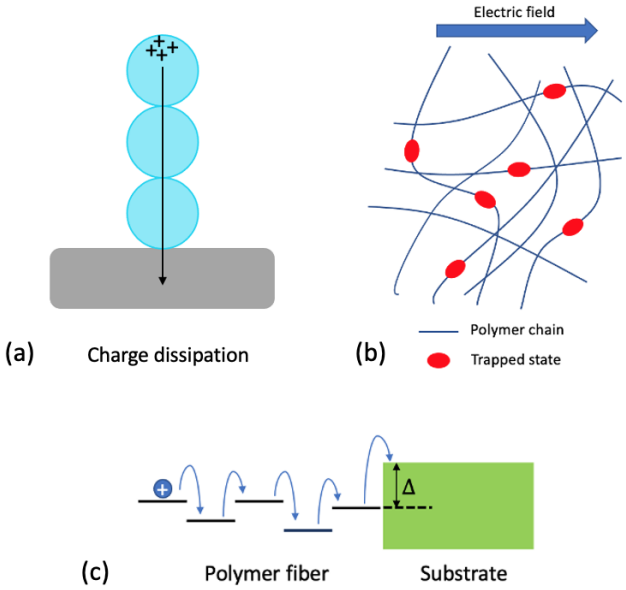

Figure 4.7.: Schematic diagram of (a) charge transport from the top of the deposited structure down to the grounded substrate (b) trapped state inside the polymeric material (c) charge injection from the polymeric material to the substrate material through an energy barrier along the interface.

As a result, the continuity equation in eq.(4.11) can be split into the trapped and mobile states

$$\frac{\partial \rho_t(z,t)}{\partial t} = S_t, \tag{4.16}$$

$$\frac{\partial \mathbf{J}(z,t)}{\partial z} + \frac{\partial \rho_f(z,t)}{\partial t} = S_f. \tag{4.17}$$

At the interface between the deposited fiber and the grounded substrate, the charges are transported from one material to another via a hopping

mechanism, as shown in fig.(4.7c), in which the charges have to overcome an energy barrier. As a result, a current boundary condition at the fiber/substrate interface is proposed as

$$\mathbf{J}(z=0,t) = \mu \mathbf{E}(0,t)\rho(0,t)exp(-\frac{\Delta}{k_B T}), \tag{4.18}$$

where Δ denotes the energy barrier, k_B denotes the Boltzmann constant and T denotes the temperature.

To validate the charge transport model, it is compared with an NFES experimental setup. As shown in fig.(4.6), a stainless steel needle is positioned at a short distance(1-2 mm) above a rotating grounded drum, and a substrate is placed on the rotating drum to collect the depositing nanofiber. As a result, the short distance minimizes the fiber deflection and enables layer-by-layer deposition. The drum has a diameter of 14 cm and rotates at a speed of 100 cm/s, which is equivalent to the deposition rate of $440ms^{-1}$. A voltage of 900-1000V is applied to the needle while the drum is grounded. Additionally, polyethylene oxide (PEO) is employed as the electrospinnable polymer feedstock, with a solvent consisting of 40% methanol and 60% water.

The model parameters are presented in tab(A.3) in the Appendix. In order to reduce the computational cost, a system with a smaller operating distance, i.e. L=300μm, between the needle and the substrate and a rescaled voltage, i.e. V=187.5V, was employed in the simulation. In the implementation, the charge transport model is based on the continuum model, in which the system is divided into many grids and the charge density of the grids is computed at each timestep. The workflow of the simulation follows the algorithm of the general grid-based models presented in fig.(2.13).

4.2.2. Charge dissipation in polymer fiber

In order to investigate the effect of the trapped state on charge dissipation, the change of total charges inside the deposited polymer fiber i) without the trapped state and ii) with the trapped state are computed over time. As in eq.(4.9), the charge distribution in the fiber at initial time $t = 0$ is described by a Gaussian distribution at its surface. For the fiber without the trapped state, all charge carriers are in the mobile states, i.e. $\rho_f = \rho$ and $\rho_t = 0$. Additionally, the rate of charge transfer from the mobile state to the trapped

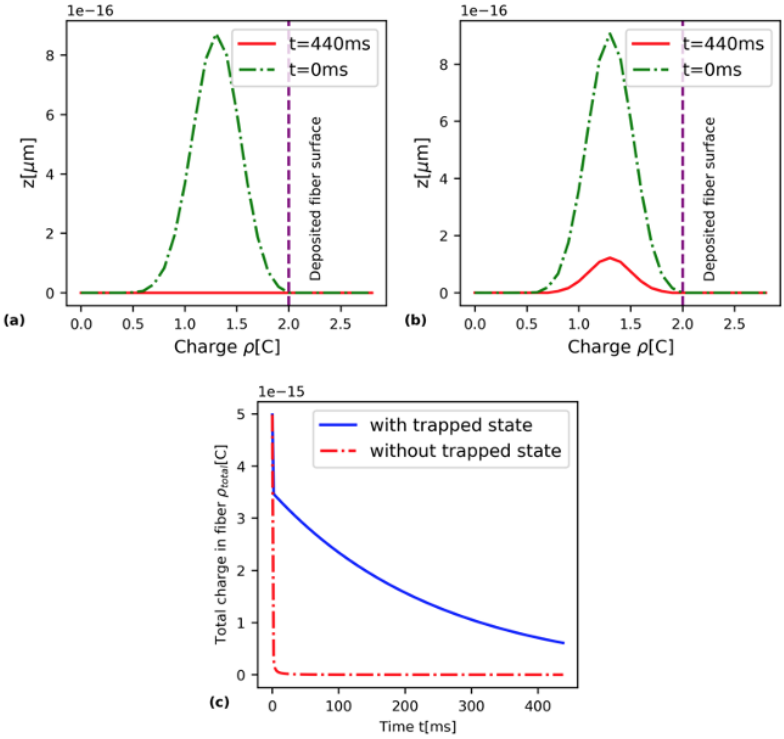

Figure 4.8.: The charge distribution of the deposited fiber a) without the trapped state and b) with the tapping state at $t = 0ms$ and $t = 440ms$ and (c) the change of total charges inside the deposited fiber over time

state or from the trapped state to the mobile state is both zero, i.e. $R_{f\to t} = 0$ and $R_{t\to f} = 0$. For the fiber with the trapped state, I set 30% of the charge carriers in the mobile states while the remaining in the trapped states at $t = 0$, i.e. $\rho_f = 0.3\rho$ and $\rho_t = 0.7\rho$. Moreover, the value of $R_{f\to t}$ and $R_{t\to f}$ are presented in table(A.3).

Fig.(4.8a) and (4.8b) depict the charge distribution inside the deposited fiber at $t = 0ms$ and $t = 440ms$ i) without the trapped state and ii) with the trapped state, respectively. The charge distribution of both systems are the same at initial time $t = 0ms$. The charge distribution of the system without the

trapped state falls to zero after 400ms, while the charge distribution of the system with the trapped state decays but remains non-zero.

Fig.(4.8c) shows the change of total charge in the deposited polymeric fiber over time. For the curve without the trapped state, the total charge quickly decreases to zero within 20ms. Under an electric field, the charges are rapidly dissipated since they can move from the fiber surface to the substrate at a high velocity without being trapped. Because of the contribution of the mobile charges, the curve with the trapped state decays at almost the same rate as the curve without the trapped state at the beginning. After a few milliseconds, the decay rate slows down as most of the charge carriers are in the trapped states. As a result, the residue charge in the system with trapped state is non-zero after t=440ms, implying that charges accumulate.

4.2.3. Breakdown of fiber self-alignment

In the previous section, I demonstrated that the charge accumulation results from the trapped state of charge carriers within the polymeric material. In this section, a charged polymer fiber deposits on top of the deposited structure for every 440ms. The charge distribution in every newly deposited fiber is described a Gaussian distribution in eq.(4.9), where 30% of the charge is in the mobile states and 70% is in the trapped states. To analyze the electromechanical behaviour of the charged fiber deposition, the electric field at the deposited fiber surface E_{sur} is computed over time. As the in-flight polymer fiber is positively charged, a negative value of the surface E-field indicates an attractive interaction between the in-flight fiber and the deposited fibers, whereas a positive value indicates a repulsive interaction.

Fig.(4.9a) shows the charge distribution inside the deposited fibers at t=2200ms, just before the deposition of the fifth layer. In the deposited fiber, charges are continuously transferred between the trapped states and the mobile states. When the charges are in the mobile states, they move rapidly toward the substrate. The charge distribution of the earlier deposited layers has a lower peak value and is shifted nearer to the substrate z=0 as more charges have been transferred from the trapped to the mobile states in the earlier deposited layers. Moreover, the charge density at the interface between the deposited layer and the substrate is non-zero, indicating some charges accumulate along the interface.

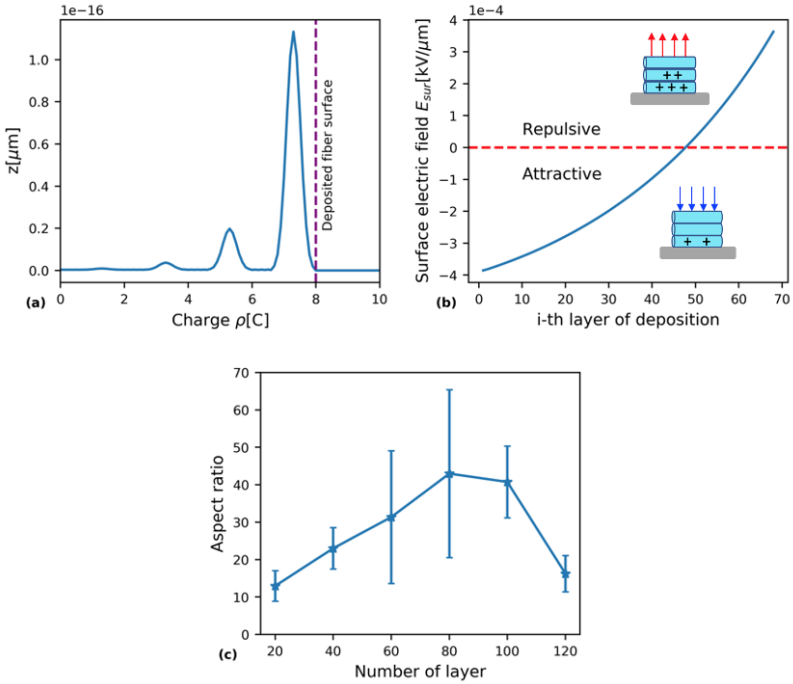

Figure 4.9.: (a) The charge distribution inside the deposited structure with four layers at 2200ms, (b) the electric field at the surface of deposited structure before the deposition of the i-th layer polymer fiber, (c) the experimental results of the aspect ratio of the wall structure with the number of deposited layers.

The surface electric field E_{sur} before the deposition of the i-th layer, i.e. $i = 1, 2, 3 \ldots$, is depicted in fig.(4.9b). The surface E-field is negative when there are only a few layers, so that the in-flight fiber is attracted by the deposited layers. Although the positive residual charges are present within the deposited fiber, the charges inside are shielded by the dielectric property of the polymeric material. As a result, the electrostatic force enables stacking the positively charged in-flight fibers on top of the wall structure, a process known as self-alignment stacking[157]. This allows the nanofibers to form an organized structure among themselves without external direction. Since the charges dissipate at a rate slower than the charge added by the fiber deposition, accumulated charges inside the wall structure increase with the number of

deposited layer. Thus, the surface E-field also increases with the number of deposited layer. After a certain number of layers, the dielectric medium is not able to shield all residual charges and the surface E-field eventually becomes positive, where the in-flight polymer fiber is then repelled by the deposited fibers. The self-alignment of the fiber deposition breaks down, and the polymer fibers are not able to stack smoothly on top of the wall structure, limiting the control of the printing. According to the simulation results, the first layer with positive surface E-field, which is referred as the breakdown layer, is 49.

In order to verify the simulation result, it is compared to an aspect ratio in the experiment, which is a ratio of the height to the thickness of the wall structure formed by the deposited fiber. The aspect ratio is typically used to quantify the controllability of fiber deposition. The experimental results of the aspect ratio with increasing number of deposited layers are shown in fig.(4.9c). When there are few layers in the wall structure, the aspect ratio gradually increases, implying that the fibers are deposited in a self-aligned manner. The aspect ratio starts to decrease after 80 layers, indicating that the self-alignment breaks down. When comparing the simulation results (>49 layers) to the experimental results (>80 layers), the simulation qualitatively agrees with the experiment by showing the breakdown of the fiber self-alignment.

4.2.4. Effect of substrate materials

The substrate in a typical NFES setup is usually made of a material other than the polymer fiber. Due to the material mismatch, the charges in the polymer medium have to overcome a material-dependent energy barrier in order to transport to the substrate. As a result, an energy barrier at the interface between the deposited fibers and substrate is introduced by implementing a current boundary condition as in eq.(4.18). The system used here is identical to the system in sec.(4.2.3), while the current boundary condition at z=0 is implemented with an energy barrier ranging from 0eV to 0.9eV at 300K. When there is no energy barrier Δ=0eV, the system is equivalent to the system in sec.(4.2.3).

Fig.(4.10a) shows the charge distributions in the deposited structure with energy barriers of Δ=0eV,0.1eV, and 0.2eV at t=2200ms. Since only charges with sufficient energy can pass through the energy barrier, the remaining charges are trapped and accumulate along the interface. Increasing the energy

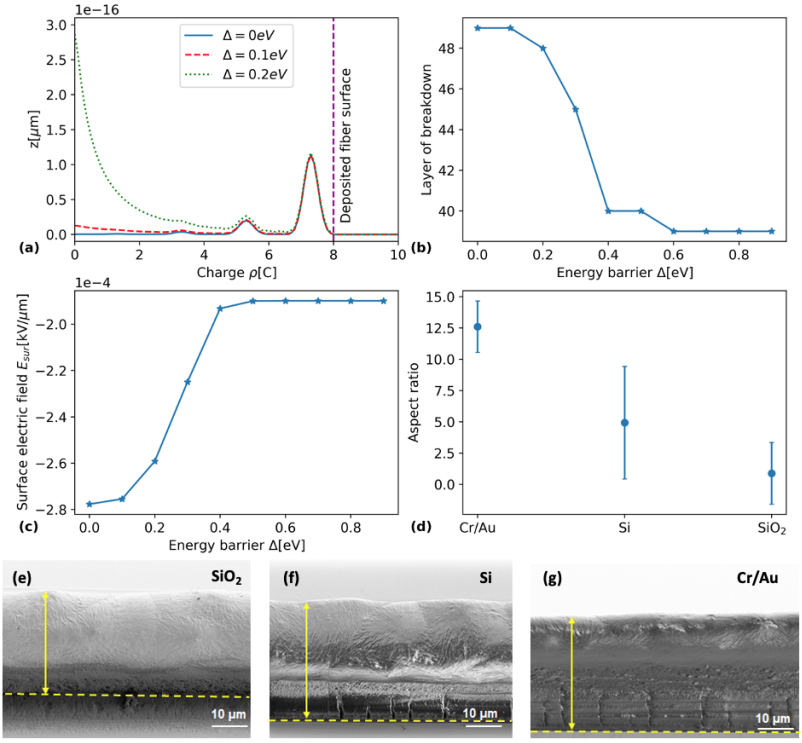

Figure 4.10.: (a) The charge distribution inside the wall structure with different energy barriers at t=2200ms, (b) the layer of breakdown with varying height of energy barrier and (c) the surface electric field of the wall structure at t=8800ms(before the deposition of the 20-th layer) with varying height of energy barrier. (d) The experimental results of the aspect ratio with different substrate material, (e)-(g) show the scanning electron microscope (SEM) images of the wall structure using SiO2, Si and Ar/Cu as the substrate, respectively ((e)-(g) reproduced from [144] with permission from the Wiley Online Library).

barrier leads to more charges accumulate along the interface, therefore the curve Δ=0.2eV has a higher charge density than the curve Δ=0.1eV and 0eV at the interface.

Fig.(4.10b) depicts the breakdown layer of the fiber deposition with varying energy barrier, while fig.(4.10c) depicts the surface E-field before the deposition of the 20-th layer with varying energy barrier. When there is no energy

barrier, i.e. Δ=0, the breakdown layer of the self-alignment is 49, as discussed in the previous section, and the surface E-field is also the most negative. As the dielectric medium can shield the accumulated charges, a slight increase in the barrier, i.e. Δ=0.1eV, has no significant impact on the breakdown layer or the surface E-field. When the energy barrier increases further, the breakdown layer clearly decreases and the surface E-field clearly increases. The dielectric medium is unable to completely shield all residual charges, so that the inner residual charges contribute to the electric field at the surface of the wall structure, hindering the self-alignment of the fiber deposition. When the energy barrier is very high, all charges are unable to pass through. As a result, the breakdown layer and the surface E-field are not significantly affected by further increases in the energy barrier after a certain value.

In order to validate the simulation results, it is compared with the experimental results, where the aspect ratio and the scanning electron microscope (SEM) images of the 20-layer structures on three different substrate materials, i.e. i) insulator(SiO_2) ii) semiconductor(Si) iii) conductor(Cr/Au), are presented in fig.(4.10d) and fig.(4.10e-g), respectively. For the conductor substrate, the charges are injected from the polymer medium to the conduction band of the conductive material, so that they can be easily transferred to the substrate. As a result, the conductor substrate is equivalent to the system without energy barrier and has the best aspect ratio among all substrates. For the semiconductor and the insulator substrates, the charges are injected from the polymer to the substrate via the hopping mechanism. This corresponds to the system with an energy barrier, where only charge with sufficient energy can activate the transport process. Therefore, the semiconductor/insulator substrate has a lower aspect ratio as less charges possess sufficient energy, and the charges accumulate along the interface.

In this section, I presented a continuum model to simulate the charge transport, dissipation, and accumulation within polymeric fibers in NFES. Within the framework of the grid-based model, 1) the trapped state and the mobile state of charge carrier and 2) the energy barrier along the interface was introduced into the continuum model to capture the behaviour of the charges in polymeric medium. As a result, this allows to investigate the charge dynamics in the solidified electrospinning fibers under an external electric field and the electromechanical behaviour of the charged fiber deposition in the NFES process.

4.3. Poling of electro-optical materials

Due to the increasing demand for high-speed information processing, optical communications have been developed rapidly in the recent years, in which the high-bandwidth electro-optical (EO) modulator is a key component of its development[168]. An EO modulator is a device that converts electrical signals into optical signals driven by a low voltage, and can be applied to optical communications, optical signal processing[169], and optical metrology[170]. In order to achieve better performance, an EO modulator should possess a high modulation efficiency, which means it can produce a large phase shift with a small driving voltage and device length.

In this section, a Mach–Zehnder modulator(MZM) is considered to demonstrate the modulation efficiency of an optical device. As shown in fig(4.11), the MZM is used to determine the relative phase shift variations between two light beams derived by splitting light from a single source. The modulation efficiency of the MZM is quantified by the product $U_\pi L$, where L is the phase shifter length and U_π is the voltage necessary to achieve a phase shift of π between the optical signals at the output of the MZM arms[37].

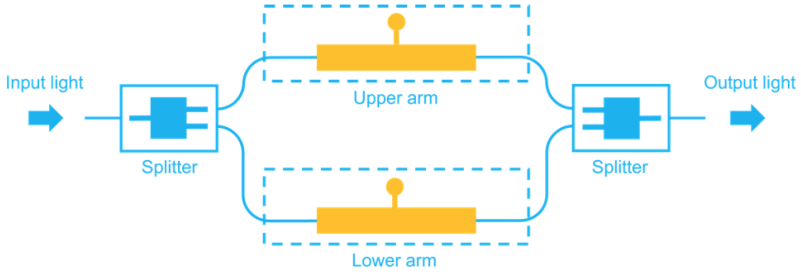

Figure 4.11.: Schematic diagram of the Mach–Zehnder modulator, in which the phase difference of light in upper and lower arm produces modulation effect (graphics from Luceda Photonics).

In EO modulators, the performance is typically determined by the electro-optical materials, which exhibits change in the optical properties in response to an electric field. The electro-optical effect of an EO material is quantified by the EO figures of merit $n^3 r_{33}$, where n is the refractive index and r_{33} is the EO coefficient. These EO figures of merit are inverse proportional to the modulation efficiency, meaning that materials with stronger non-linear

optical effects result in more efficient phase shifts during modulation. Organic non-linear optical chromophores have been widely studied to achieve a high EO coefficient[171], in which the EO coefficient of chromophores depends on the density, hyperpolarizability, and orientation of the chromophores[172]

$$r_{33} \propto N\beta\langle cos^3\theta\rangle, \tag{4.19}$$

N denotes the density of the system, β denotes the hyperpolarizability, and $cos\theta$ denotes the orientation of the chromophores. Among the high efficient EO modulators, silicon-organic hybrid (SOH) devices, which combine organic EO materials (chromophores) with silicon photonic waveguide structures, show promising low $U_\pi L$ values down to 0.5Vmm[173].

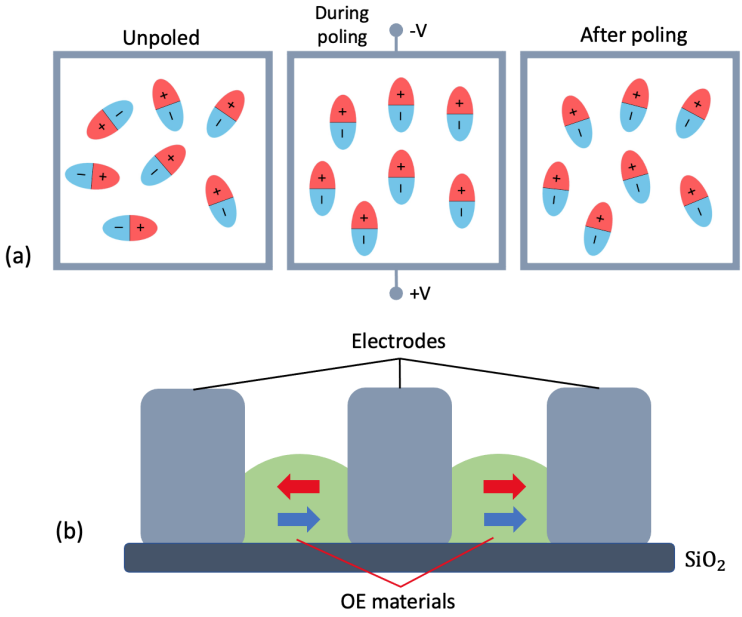

Figure 4.12.: (a) Illustration of the poling process, in which the EO materials are aligned by applying external electric field. (b) Illustration of a silicon-organic hybrid (SOH) devices, where the EO materials are aligned by applying poling field (blue arrows) and then exhibit large phase shift by applying modulation field (red arrows).

To activate the modulation with a non-zero EO coefficient, the chromophores, which are initially randomly orientated, can be aligned through a poling

process[37]. During poling, the SOH chip is heated above the glass transition temperature T_g of the chromophores, and a DC voltage is applied across the electrodes to align the dipoles of the chromophores in the two slots, as presented in fig.(4.12). By subsequently cooling the device while maintaining the DC poling field, the orientation of the chromophores is preserved at room temperature.

4.3.1. Atomistic model for chromophores poling

To model the poling process of the chromophores system, atomistic MD simulations are employed. The system under consideration consists of co-polymer with three different monomers: MMA, AdMA, and HEMA, in a ratio of 40:50:10, as shown in fig.(4.13). The chromophore functional group is attached to the HEMA monomer via a linker. Three types of linkers are considered: IPDI, TDI, and HMDI, as depicted in fig.(4.13). However, the timescales required for the alignment of the polymer system are typically beyond the limits of atomistic simulation. To make the simulation computationally feasible for studying the poling behaviour, a virtual system of chromophores is employed, as illustrated in fig.(4.14). Instead of considering the entire polymer chain, I considered the oligomers with 5 repeating units of MMA and AdMA, as well as the HEMA with the connecting chromophores. The HEMA monomers are fixed at specific positions with springs, allowing the dipolar chromophores to rotate but not translate under an electric field. The virtual system is more flexible than the polymer system, enabling the atomistic MD simulations to study the poling behaviour effectively.

During the simulation, the chromophore system was initially heated above the glass temperature T_g, and an external electric field was applied to align the dipolar chromophores during the poling process. The NPT ensemble was performed throughout the simulation. For the first 0.1ns, the temperature of the system was increased from 300K to the poling temperature T_p. The poling electric field E_p was then applied to the system at T_p, causing the chromophores to orient along the electric field. In the end, the system was cooled down to 300K while maintaining a constant electric field E_p.

In order to study the alignment of the chromophores, the angle θ between the dipole moment of the chromophores and the electric field was computed

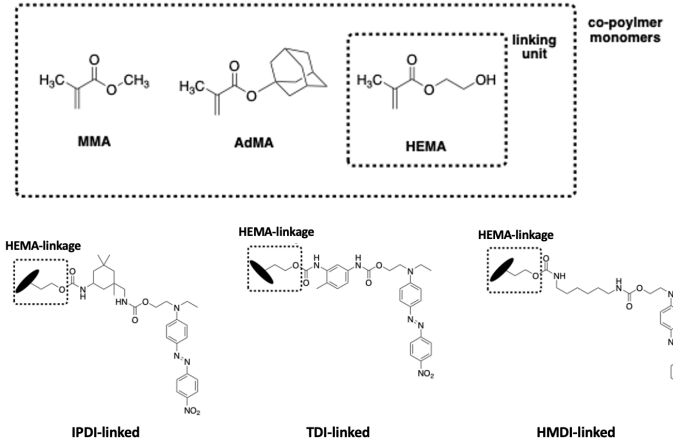

Figure 4.13.: Chemical structure of MMA, AdMA, and HEMA in the co-polymer system, and the chromophores are linked to the HEMA monomer with three different linkers: IPDI, TDI, and HMDI.

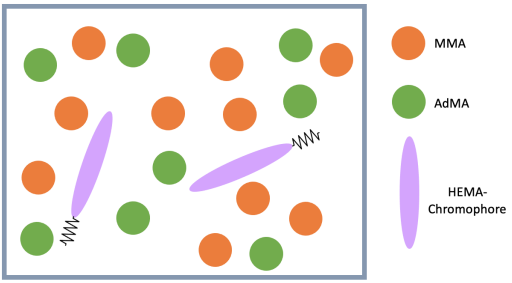

Figure 4.14.: Schematic diagram of the virtual system in which a polymer chain is divided into oligomers and side-chain segments with fixed position by spring.

$$cos\theta = \sum_i q_i \mathbf{r}_i \cdot \mathbf{E}_p \tag{4.20}$$

where q_i and $\mathbf{r}_i$ are the partial charge and position of atom i in the chromophores. In this thesis, $cos^3\theta$ is considered as a measure of the alignment of the chromophore system, as it can be directly related to the EO coefficient in eq.(4.19).

To prepare the simulation, the oligomers and side-chains were prepared by automated forcefield topology builder (ATB)[174] and the forcefield parameters were obtained from the GROMOS forcefield[128]. The initial configurations of the system were generated using PACKMOL[175] and the simulations were performed in LAMMPS[107]. Moreover, the computation of the alignment was obtained from the ensemble average to minimize the errors and fluctuations.

4.3.2. Effect of types of linker

Here I performed the poling simulation of the chromophores with different linkers with E_p=0.2$V\mathring{A}^{-1}$ and T_p=500K. Fig.(4.15) illustrates the evolution of the side-chain alignment $\langle cos^3\theta \rangle$ over time. For the first 20ns, the temperature is increased to T_p and an electric field is applied at E_p, so that the chromophores are flexible to orient along the electric field. As a result, the alignment $\langle cos^3\theta \rangle$ increases with time until reaches a constant value. The alignment cannot be increased further since the neighbouring molecules hinder the movement of the side-chains in a dense system. Moreover, the fluctuation of the curve indicates the competition between the effect of the thermal fluctuation and the electric field on the configuration of the system. After 20ns, the system is cooled to 300K while the electric field is maintained. The alignment of the sidechains remains constant as the sidechains are less flexible to orient when the temperature decreases. As a result, the system is "frozen" and the alignment of the chromophores is preserved after the poling process.

To compare the modulation efficiency of different organic EO materials, fig.(4.15a) shows the alignment of chromophores with different linkers in poling, and (4.15b) and table(4.1) shows the average alignment of the chromophores with different linkers after poling from 20ns to 30ns. The alignment values $\langle cos^3\theta \rangle$ of TDI-, IPDI-, and HMDI-linked chromophores are 0.1625, 0.1519, and 0.1414, respectively. The differences in alignment among different linkers are small, possibly due to the thermal fluctuations in the system. Therefore, there is no clear influence for using different linkers in the chromophores poling process.

Table 4.1.: Average alignment of chromophores with different linkers over time after poling

Linkers	$\langle cos^3\theta \rangle$
TDI	0.1625
IPDI	0.1519
HMDI	0.1414

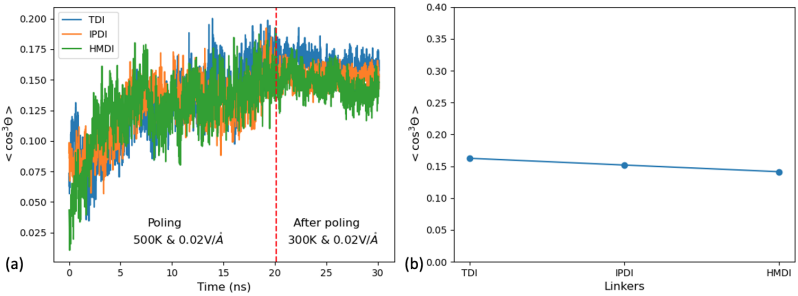

Figure 4.15.: (a)Alignment of the chromophores with different linker types over time (b) average alignment of the chromophores with varying linkers after poling

4.3.3. Effect of poling temperature

The effect of poling temperature on chromophore poling is investigated here, where the HMDI-linked system is employed with E_p=0.02$V\mathring{A}^{-1}$ and varying T_p, i.e. 300K, 400K, and 500K. The alignment of chromophores over time with varying T_p is depicted in fig.(4.16a) and the average alignment after poling with varying T_p is presented in fig.(4.16b) and table(4.2). For T_p=300K, this corresponds to the system remains at constant temperature without applying poling temperature. Therefore, the curve of 300K does not increase with time and the value of the average alignment over time is given by 0.0535, which is close to zero. For the curve T_p=400K, the alignment of the chromophores is slightly higher than the curve of 300K and the value of average alignment after poling is only 0.0592, which is also close to zero. Although the system is heated to 400K, the poling temperature is still below the glass temperature. As a result, below the glass temperature, the system is still rigid, limiting the sidechains to move and align. For T_p=500K, the alignment of the chromophores increases rapidly in a short time until reaching a constant value. Since T_p=500K is above the glass temperature, the system is flexible and the sidechains are able to

move and align along the electric field, resulting in the average alignment with a value of 0.1414. This implies the alignment of the EO materials can be achieved only above the glass temperature in the poling process.

Table 4.2.: Average alignment of chromophores with varying poling temperature over time after poling

Poling temperature T_p (K)	$\langle cos^3\theta \rangle$
300	0.0535
400	0.0592
500	0.1414

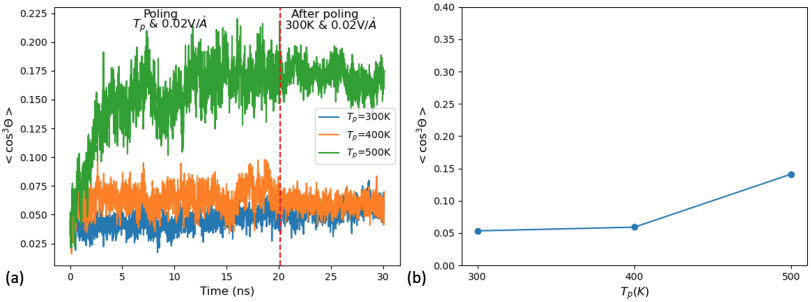

Figure 4.16.: (a) Alignment of the chromophores with varying poling temperature over time (b) average alignment of the chromophores with varying poling temperature after poling

4.3.4. Effect of poling field

In the end, the effect of poling field on the chromophores alignment during poling is studied. Here a HMDI-linked system with T_p=500K and varying E_p, i.e. 0.01V/Å, 0.02V/Å, and 0.03V/Å, is considered. Fig.(4.17a) shows the results of the chromophores alignment with varying E_p and the average alignment after poling with varying E_p is presented in fig.(4.17b) and table(4.3). For E_p=0.01V/Å, the chromophores alignment does not increase with time. As the poling field is too low, the thermal fluctuation of the sidechains is stronger than the electric force on them. As a result, the chromophores do not show any alignment and the average alignment after poling is only 0.0452. For E_p=0.02V/Å, the alignment of the chromophore increases with time and the

value of the average alignment after poling is 0.1414. When a stronger poling field is applied to the system, the effect of the electric force dominates over the thermal fluctuation, enabling the dipolar groups of the sidechains to orient along the electric field. Thus, this results in a higher alignment value. For E_p=0.03V/$\mathring{A}$, the alignment increases more rapidly than that of 0.02V/$\mathring{A}$, resulting in a higher value of average alignment after poling, which is 0.2489. When the poling field increases, the electric field introduces more energy into the system to align the dipolar chromophores along the applied field. Therefore, the higher the electric field, the higher the alignment of the organic EO materials. This is also in agreement with the previous experimental study, in which the EO figures of merit $n^3 r_{33}$ increases linearly with the poling field [176].

Table 4.3.: Average alignment of chromophores with varying poling field over time after poling

Poling field E_p (V/$\mathring{A}$)	$\langle cos^3\theta \rangle$
0.01	0.0452
0.02	0.1414
0.03	0.2489

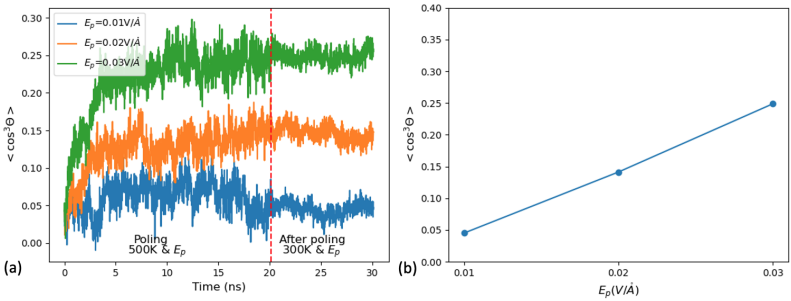

Figure 4.17.: (a) Alignment of the chromophores with varying poling field over time (b) average alignment of the chromophores with varying poling field after poling

In this section, the atomstic MD simulations are employed to investigate the molecular alignment of organic EO materials in poling. Due to the computational limitation of the atomistic MD for simulating the mesoscopic behaviour, a virtual system is considered here. In the virtual system, the polymer chain is divided into oligomers, and the sidechains are fixed at particular positions with springs. As a result, the sidechains are more flexible to orient

compared to the entire polymer chain, allowing the atomistic MD to simulate chromophores alignment under an external electric field. By using the virtual system scheme, the effects of different linkers, poling temperature, and poling field on the alignment of chromophores can be studied. As a result, the behaviour of the EO materials in poling can be better understood. This approach enables the exploration of EO materials in the poling process, providing insights for the fabrication of effective EO modulators.

5. Summary and outlook

5.1. Summary

Mesoscopic behaviour in soft matter is typically triggered by molecular interactions and exhibits properties at the macroscopic scale. This implies that mesoscopic phenomena cover a wide range of scales. Therefore, it is challenging for theoretical models to study the mescosopic effects. In order to model mesoscopic behaviour in soft matter systems, various approaches, such as the CG model and the DPD model, have been developed and successfully applied to different soft matter problems. However, these models have certain deficiencies when it comes to accurately capturing mesoscopic phenomena. The CG model shows inconsistent dynamical properties, while the DPD model lacks the chemical descriptions of the system. Therefore, there is a need for a proper derivation of coarse-graining.

In this thesis, a systematic formalism for coarse-graining is presented. In ch.(3), I employed the Mori-Zwanzig formalism, which divides the microscopic system into slow and fast degrees of freedom. The slow degrees of freedom are projected onto the collective variables as the conservative forces, while the fast degrees of freedom are approximated by dissipative and stochastic terms as the non-conservative forces in the mesoscopic system. This approach allows for the derivation of a closed equation of motion for the collective variables, capturing the chemical descriptions of the system and consistently reproducing long-time dynamical properties. One of the key results in this work is the development of an anisotropic DPD model using the MZ formalism. With an example of benzene, an appropriate forcefield was derived using ellipsoidal CG particles to represent benzene molecules. The interactions between the ellipsoidal particles are determined not only by their separation but also by their relative orientation. For the conservative forcefield, the pairwise conservative force was approximated by the sum of the Gay-Berne force and the electric multipole force. For the non-conservative forcefield,

I noted that it is not necessarily isotropic. A modified repulsive Gay-Berne functional, which is a GB-like functional without attractive part, was proposed to approximate the frictional force. In order to parameterize the complex conservative and frictional forcefields efficiently, a two-step parameterization was employed. Additionally, the stochastic force was obtained from the frictional force via the fluctuation-dissipation theorem. The performance of the AMZDPD model was evaluated by comparing it to other CG models, including Martini3, MZDPD and GB-CG. The AMZDPD model demonstrated outstanding performance in both static and dynamical properties. For the computed diffusion constant, the AMZDPD model outperforms the other CG models, with only a 3.6% error compared to the reference MD value.

In ch.(4), I presented the applications of three different models to three mesoscopic phenomena. The first example studied the crystallization process of pentacene using the AMZDPD model, where pentacene molecules were represented by dissimilar ellipsoidal CG particles. Crystallization is a mesoscopic phenomenon in which molecules interact, aggregate and self-assemble to form an ordered structure. The degree of crystallization was evaluated using the long-range nematic order parameter and the short-range herringbone order parameter. The results obtained from the AMZDPD model, however, shows incorrect predictions, with the CG pentacene self-assembling into a brick-wall structure instead of the expected herringbone structure. This discrepancy may be attributed to the construction of the mesoscopic system using an incorrect atomistic forcefield for crystallization process. Nevertheless, the AMZDPD model demonstrated the self-assembly of pentacene to form ordered structure at the CG level using anisotropic CG particles.

The second example used a continuum model to investigate the electromechanical mechanism of electrospinning fiber deposition. The residue charges inside the electrospinning polymer fibers determine the deposition process and the quality of 3d printing. In order to study the charge dynamics in polymeric medium, a one-dimensional charge transport model was employed. The results of the charge dissipation revealed that the trapped state of charge carrier is the main source of charge accumulation in polymeric medium. Moreover, the surface electric field of the deposited fibers was computed to analyze the electromechanical behaviour of the fiber deposition, and the break-down of the fiber self-alignment after a certain number of deposition was illustrated. The effect of different substrates on fiber deposition was also investigated, demonstrating that conductors yield the best deposition results, which is in good qualitative agreement with the experiment.

The last example employed the atomistic MD to study the poling process of electro-optical materials, specifically the chromophores. Poling is a mesoscopic process that aligns the dipolar functional groups under an external electric field, so that the non-linear optical effect of EO materials is activated. To simulate the poling process with atomistic MD, a virtual system was employed, where the polymer chain is divided into oligomers and side-chain segments with fixed position, increasing the flexibility of the side-chains to rotate. Various operating parameters, such as the linker types, poling temperature, and poling field, were varied to study the poling process of the chromophores. The results indicate that the linker type does not significantly influence the poling process, whereas the poling temperature shows a clear increase in the side-chain alignment when the system is above the glass temperature. Moreover, the alignment of side-chains increases with higher poling field as more energy is introduced into the system to align the dipolar groups.

To conclude this thesis, I have presented three different schemes for mesoscopic modelling. The modified atomistic MD and the modified continuum model discussed in ch.(4) are constructed from the limit of the atomistic and continuum scales, with introducing the artificial modifications into the system to describe the mesoscopic effects. In order to obtain physical and logical results from these artificial modifications, priori knowledge of the models, systems of interest, and the effects of the modification is necessary. Although there are some deficiencies, i.e. incorrect timescales or oversimplified interactions, these schemes are relatively easy to implement and can qualitatively model specific mesoscopic problems at a low computational cost. The AMZDPD model, on the other hand, is derived from a systematic formalism of coarse-graining, enabling to generate accurate and consistent results for mesoscopic modelling. In the example of benzene, it shows the ability to reproduce the static and dynamical properties quantitatively. Despite the need for further studies and improvements, this dynamically consistent CG approach shows great potential for studying various dynamical-related mesoscopic problems in soft matter, such as diffusion in polymer solutions, self-assembly of biomolecules, or phase transitions.

5.2. Outlook

As shown in this work, the developed AMZDPD approach shows promising potential in mesoscopic modelling. However, there are a few issues that would be worth studying in order to improve or apply it to more complex systems. Firstly, the heterogeneous system should be studied when the model is applied to more complex systems. For instance, mixing rules, i.e. geometric mixing, could be a direction for modelling heterogeneous systems. Additionally, the intramolecular CG interaction is important when complex molecules require multiple CG particles to describe their structures. A possible improvement could be the implementation of distance- and orientation-dependent intramolecular CG potentials using the Boltzmann inversion method[177].

The complexity of parameterization is one of the bottlenecks for the AMZDPD model. To parameterize a system in the AMZDPD approach, it requires a significant amount of time to approximate the complex interactions. Moreover, the transferability from one system to another is limited. Recently, machine learning (ML) has demonstrated promising potential in mesoscopic modelling. Recent work proposed a ML framework to select CG representations based on variational auto-encoders, so that the CG mapping can be optimized automatically without priori considerations[66]. Another study proposed a CG forcefield constructed using an ML approach, which provides better approximation than conventional functional-forms forcefield as it includes multibody effects and nonlinearities automatically[178]. Therefore, machine learning could offer a possibility for further development of the AMZDPD model as well as mesoscopic modelling, as it enables automatic CG mapping and provides more efficient forcefield construction. With the advancement of computational power and the development of algorithm, mesosocpic modelling has enormous potential for applications in a wide range of fields, such as polymers, macromolecules, and biological systems.

Bibliography

1. Kleman, M. & Lavrentovich, O. D. *Soft matter physics: an introduction* (Springer, 2003).
2. Zhou, L.-Y., Fu, J. & He, Y. A review of 3D printing technologies for soft polymer materials. *Advanced Functional Materials* **30,** 2000187 (2020).
3. Friederich, P. *et al.* Toward design of novel materials for organic electronics. *Advanced Materials* **31,** 1808256 (2019).
4. Liu, J. *et al.* Recent advances in polymer electro-optic modulators. *Rsc Advances* **5,** 15784–15794 (2015).
5. Liu, M. *et al.* Recent developments in polydopamine: an emerging soft matter for surface modification and biomedical applications. *Nanoscale* **8,** 16819–16840 (2016).
6. Schiller, U. D., Krüger, T. & Henrich, O. Mesoscopic modelling and simulation of soft matter. *Soft matter* **14,** 9–26 (2018).
7. Wiese, O., Marenduzzo, D. & Henrich, O. Microfluidic flow of cholesteric liquid crystals. *Soft Matter* **12,** 9223–9237 (2016).
8. Wang, S.-Q., Ravindranath, S., Wang, Y. & Boukany, P. New theoretical considerations in polymer rheology: Elastic breakdown of chain entanglement network. *The Journal of chemical physics* **127,** 064903 (2007).
9. Rahman, A. Correlations in the Motion of Atoms in Liquid Argon. *Phys. Rev.* **136,** A405–A411 (2A Oct. 1964).
10. Jorgensen, W. L., Maxwell, D. S. & Tirado-Rives, J. Development and testing of the OPLS all-atom force field on conformational energetics and properties of organic liquids. *Journal of the American Chemical Society* **118,** 11225–11236 (1996).
11. Rappé, A. K., Casewit, C. J., Colwell, K., Goddard III, W. A. & Skiff, W. M. UFF, a full periodic table force field for molecular mechanics and molecular dynamics simulations. *Journal of the American chemical society* **114,** 10024–10035 (1992).

12. Tadmor, E. B., Miller, R. E. & Elliott, R. S. *Continuum mechanics and thermodynamics: from fundamental concepts to governing equations* (Cambridge University Press, 2012).

13. Levitt, M. & Warshel, A. Computer simulation of protein folding. *Nature* **253,** 694–698 (1975).

14. Warshel, A. & Levitt, M. Theoretical studies of enzymic reactions: dielectric, electrostatic and steric stabilization of the carbonium ion in the reaction of lysozyme. *Journal of molecular biology* **103,** 227–249 (1976).

15. Kmiecik, S. *et al.* Coarse-grained protein models and their applications. *Chemical reviews* **116,** 7898–7936 (2016).

16. Karimi-Varzaneh, H. A., Van Der Vegt, N. F., Müller-Plathe, F. & Carbone, P. How good are coarse-grained polymer models? A comparison for atactic polystyrene. *ChemPhysChem* **13,** 3428–3439 (2012).

17. Lee, O.-S., Cho, V. & Schatz, G. C. Modeling the self-assembly of peptide amphiphiles into fibers using coarse-grained molecular dynamics. *Nano letters* **12,** 4907–4913 (2012).

18. Hoogerbrugge, P. & Koelman, J. Simulating microscopic hydrodynamic phenomena with dissipative particle dynamics. *Europhysics letters* **19,** 155 (1992).

19. Espanol, P. & Warren, P. Statistical mechanics of dissipative particle dynamics. *Europhysics letters* **30,** 191 (1995).

20. Nikunen, P., Vattulainen, I. & Karttunen, M. Reptational dynamics in dissipative particle dynamics simulations of polymer melts. *Physical Review E* **75,** 036713 (2007).

21. Fedosov, D. A., Caswell, B. & Karniadakis, G. E. A multiscale red blood cell model with accurate mechanics, rheology, and dynamics. *Biophysical journal* **98,** 2215–2225 (2010).

22. Malevanets, A. & Kapral, R. Mesoscopic model for solvent dynamics. *The Journal of chemical physics* **110,** 8605–8613 (1999).

23. Gompper, G., Ihle, T., Kroll, D. & Winkler, R. Multi-particle collision dynamics: A particle-based mesoscale simulation approach to the hydrodynamics of complex fluids. *Advanced computer simulation approaches for soft matter sciences III,* 1–87 (2009).

24. Ripoll, M., Winkler, R. & Gompper, G. Star polymers in shear flow. *Physical review letters* **96,** 188302 (2006).

25. Succi, S. *The lattice Boltzmann equation: for fluid dynamics and beyond* (Oxford university press, 2001).

26. Chen, S. & Doolen, G. D. Lattice Boltzmann method for fluid flows. *Annual review of fluid mechanics* **30,** 329–364 (1998).

27. Schlijper, A., Hoogerbrugge, P. & Manke, C. Computer simulation of dilute polymer solutions with the dissipative particle dynamics method. *Journal of Rheology* **39,** 567–579 (1995).

28. Espanol, P. & Warren, P. B. Perspective: Dissipative particle dynamics. *The Journal of chemical physics* **146,** 150901 (2017).

29. Zwanzig, R. Ensemble method in the theory of irreversibility. *The Journal of Chemical Physics* **33,** 1338–1341 (1960).

30. Mori, H. Transport, collective motion, and Brownian motion. *Progress of theoretical physics* **33,** 423–455 (1965).

31. Español, P. Dissipative particle dynamics for a harmonic chain: A first-principles derivation. *Physical Review E* **53,** 1572 (1996).

32. Kushick, J. & Berne, B. J. Computer simulation of anisotropic molecular fluids. *The Journal of Chemical Physics* **64,** 1362–1367 (1976).

33. Gay, J. & Berne, B. Modification of the overlap potential to mimic a linear site–site potential. *The Journal of Chemical Physics* **74,** 3316–3319 (1981).

34. Whitesides, G. M. & Boncheva, M. Beyond molecules: Self-assembly of mesoscopic and macroscopic components. *Proceedings of the National Academy of Sciences* **99,** 4769–4774 (2002).

35. Sirringhaus, H. 25th anniversary article: organic field-effect transistors: the path beyond amorphous silicon. *Advanced materials* **26,** 1319–1335 (2014).

36. Collins, G., Federici, J., Imura, Y. & Catalani, L. H. Charge generation, charge transport, and residual charge in the electrospinning of polymers: A review of issues and complications. *Journal of Applied Physics* **111,** 044701 (2012).

37. Koos, C. *et al.* Silicon-organic hybrid (SOH) and plasmonic-organic hybrid (POH) integration. *Journal of Lightwave Technology* **34,** 256–268 (2016).

38. Alder, B. J. & Wainwright, T. E. Studies in Molecular Dynamics. I. General Method. *The Journal of Chemical Physics* **31,** 459–466 (1959).

39. Koehl, P. & Levitt, M. A brighter future for protein structure prediction. *nature structural biology* **6,** 108–111 (1999).

40. Karplus, M. & McCammon, J. A. Molecular dynamics simulations of biomolecules. *Nature structural biology* **9,** 646–652 (2002).

41. Van Gunsteren, W. F. & Berendsen, H. J. Computer simulation of molecular dynamics: methodology, applications, and perspectives in chemistry. *Angewandte Chemie International Edition in English* **29,** 992–1023 (1990).

42. Krishna, S., Sreedhar, I. & Patel, C. M. Molecular dynamics simulation of polyamide-based materials–A review. *Computational Materials Science* **200,** 110853 (2021).

43. McWeeny, R. & Pickup, B. Quantum theory of molecular electronic structure. *Reports on Progress in Physics* **43,** 1065 (1980).

44. Born, M. & Heisenberg, W. Zur quantentheorie der molekeln. *Original Scientific Papers Wissenschaftliche Originalarbeiten,* 216–246 (1985).

45. Sun, L. & Hase, W. L. Born–Oppenheimer direct dynamics classical trajectory simulations. *Reviews in computational chemistry* **19,** 79–146 (2003).

46. Maple, J. R., Dinur, U. & Hagler, A. T. Derivation of force fields for molecular mechanics and dynamics from ab initio energy surfaces. *Proceedings of the National Academy of Sciences* **85,** 5350–5354 (1988).

47. Damm, W., Frontera, A., Tirado–Rives, J. & Jorgensen, W. L. OPLS all-atom force field for carbohydrates. *Journal of computational chemistry* **18,** 1955–1970 (1997).

48. Wang, J., Wolf, R. M., Caldwell, J. W., Kollman, P. A. & Case, D. A. Development and testing of a general amber force field. *Journal of computational chemistry* **25,** 1157–1174 (2004).

49. Fernandes, H. S., Cerqueira, N. M., Sousa, S. F. & Melo, A. A Molecular Mechanics Energy Partitioning Software for Biomolecular Systems. *Molecules* **27,** 5524 (2022).

50. Peskin, C. S. & Schlick, T. Molecular dynamics by the Backward-Euler method. *Communications on pure and applied mathematics* **42,** 1001–1031 (1989).

51. Verlet, L. Computer" experiments" on classical fluids. I. Thermodynamical properties of Lennard-Jones molecules. *Physical review* **159,** 98 (1967).

52. Swope, W. C., Andersen, H. C., Berens, P. H. & Wilson, K. R. A computer simulation method for the calculation of equilibrium constants for the formation of physical clusters of molecules: Application to small water clusters. *The Journal of chemical physics* **76,** 637–649 (1982).

53. Squire, D. R. & Salsburg, Z. W. Formulation of a Cell Model Using Periodic Boundary Conditions. *The Journal of Chemical Physics* **35,** 486–492 (1961).

54. Matthews, B. *Molecular Dynamics with Deterministic and Stochastic Numerical Methods* 2015.

55. Nosé, S. A unified formulation of the constant temperature molecular dynamics methods. *The Journal of chemical physics* **81,** 511–519 (1984).

56. Hoover, W. G. Canonical dynamics: Equilibrium phase-space distributions. *Physical review A* **31,** 1695 (1985).

57. Parrinello, M. & Rahman, A. Polymorphic transitions in single crystals: A new molecular dynamics method. *Journal of Applied physics* **52,** 7182–7190 (1981).

58. Shinoda, W., Shiga, M. & Mikami, M. Rapid estimation of elastic constants by molecular dynamics simulation under constant stress. *Physical Review B* **69,** 134103 (2004).

59. Plimpton, S. Fast parallel algorithms for short-range molecular dynamics. *Journal of computational physics* **117,** 1–19 (1995).

60. Berendsen, H. J., van der Spoel, D. & van Drunen, R. GROMACS: A message-passing parallel molecular dynamics implementation. *Computer physics communications* **91,** 43–56 (1995).

61. Phillips, J. C. *et al.* Scalable molecular dynamics on CPU and GPU architectures with NAMD. *The Journal of chemical physics* **153,** 044130 (2020).

62. Plimpton, S. Computational limits of classical molecular dynamics simulations. *Computational Materials Science* **4,** 361–364 (1995).

63. Voth, G. A. *Coarse-graining of condensed phase and biomolecular systems* (CRC press, 2008).

64. Rudzinski, J. F. & Noid, W. G. Investigation of coarse-grained mappings via an iterative generalized Yvon–Born–Green method. *The Journal of Physical Chemistry B* **118,** 8295–8312 (2014).

65. Noid, W. G. Perspective: Coarse-grained models for biomolecular systems. *The Journal of chemical physics* **139,** 09B201_1 (2013).

66. Wang, W. & Gómez-Bombarelli, R. Coarse-graining auto-encoders for molecular dynamics. *npj Computational Materials* **5,** 125 (2019).

67. Drouffe, J.-M., Maggs, A. & Leibler, S. Computer simulations of self-assembled membranes. *Science* **254,** 1353–1356 (1991).

68. Cooke, I. R., Kremer, K. & Deserno, M. Tunable generic model for fluid bilayer membranes. *Physical Review E* **72,** 011506 (2005).

69. Marrink, S. J., Risselada, H. J., Yefimov, S., Tieleman, D. P. & De Vries, A. H. The MARTINI force field: coarse grained model for biomolecular simulations. *The journal of physical chemistry B* **111,** 7812–7824 (2007).

70. De Jong, D. H. *et al.* Improved parameters for the martini coarse-grained protein force field. *Journal of chemical theory and computation* **9,** 687–697 (2013).

71. Toth, G. Effective potentials from complex simulations: a potential-matching algorithm and remarks on coarse-grained potentials. *Journal of Physics: Condensed Matter* **19,** 335222 (2007).

72. Li, W. & Takada, S. Characterizing protein energy landscape by self-learning multiscale simulations: Application to a designed β-hairpin. *Biophysical journal* **99,** 3029–3037 (2010).

73. Akkermans, R. L. & Briels, W. J. A structure-based coarse-grained model for polymer melts. *The Journal of Chemical Physics* **114,** 1020–1031 (2001).

74. Tschöp, W., Kremer, K., Batoulis, J., Bürger, T. & Hahn, O. Simulation of polymer melts. I. Coarse-graining procedure for polycarbonates. *Acta Polymerica* **49,** 61–74 (1998).

75. Noid, W., Chu, J.-W., Ayton, G. S. & Voth, G. A. Multiscale coarse-graining and structural correlations: Connections to liquid-state theory. *The Journal of Physical Chemistry B* **111,** 4116–4127 (2007).

76. Mullinax, J. & Noid, W. Reference state for the generalized Yvon–Born–Green theory: Application for coarse-grained model of hydrophobic hydration. *The Journal of chemical physics* **133,** 124107 (2010).

77. Van der Gucht, J. *Grand challenges in soft matter physics* 2018.

78. Green, M. S. Markoff random processes and the statistical mechanics of time-dependent phenomena. *The Journal of Chemical Physics* **20,** 1281–1295 (1952).

79. Song, S. *et al.* Transport dynamics of complex fluids. *Proceedings of the National Academy of Sciences* **116,** 12733–12742 (2019).

80. Ma, L., Li, X. & Liu, C. The derivation and approximation of coarse-grained dynamics from Langevin dynamics. *The Journal of chemical physics* **145,** 204117 (2016).

81. Groot, R. D. & Warren, P. B. Dissipative particle dynamics: Bridging the gap between atomistic and mesoscopic simulation. *The Journal of chemical physics* **107,** 4423–4435 (1997).

82. Espanol, P. Hydrodynamics from dissipative particle dynamics. *Physical Review E* **52,** 1734 (1995).

83. Hossain, M. & Steinmann, P. Continuum physics of materials with time-dependent properties: reviewing the case of polymer curing. *Advances in applied mechanics* **48,** 141–259 (2015).

84. Calamai, G. Batchelor, GK-An Introduction to Fluid Dynamics (1970).

85. De Groot, S. R. & Mazur, P. *Non-equilibrium thermodynamics* (Courier Corporation, 2013).

86. Haupt, P. On the mathematical modelling of material behavior in continuum mechanics. *Acta Mechanica* **100,** 129–154 (1993).

87. Pinnau, R. A review on the quantum drift diffusion model. *Transport Theory and Statistical Physics* **31,** 367–395 (2002).

88. Steinbach, I. Phase-field models in materials science. *Modelling and simulation in materials science and engineering* **17,** 073001 (2009).

89. David Müzel, S., Bonhin, E. P., Guimarães, N. M. & Guidi, E. S. Application of the finite element method in the analysis of composite materials: A review. *Polymers* **12,** 818 (2020).

90. Chen, L.-Q. Phase-field models for microstructure evolution. *Annual review of materials research* **32,** 113–140 (2002).

91. Davies, E. B. & Davies, E. B. *Spectral theory and differential operators* (Cambridge University Press, 1995).

92. Jacobi, C. G. Ueber eine neue Auflösungsart der bei der Methode der kleinsten Quadrate vorkommenden lineären Gleichungen. *Astronomische Nachrichten* **22,** 297–306 (1845).

93. Hijón, C., Español, P., Vanden-Eijnden, E. & Delgado-Buscalioni, R. Mori–Zwanzig formalism as a practical computational tool. *Faraday discussions* **144,** 301–322 (2010).

94. Lei, H., Caswell, B. & Karniadakis, G. E. Direct construction of mesoscopic models from microscopic simulations. *Physical Review E* **81,** 026704 (2010).

95. Akkermans, R. L. & Briels, W. J. Coarse-grained dynamics of one chain in a polymer melt. *The Journal of Chemical Physics* **113,** 6409–6422 (2000).

96. Chorin, A. J., Hald, O. H. & Kupferman, R. Optimal prediction with memory. *Physica D: Nonlinear Phenomena* **166,** 239–257 (2002).

97. Li, Z., Bian, X., Li, X. & Karniadakis, G. E. Incorporation of memory effects in coarse-grained modeling via the Mori-Zwanzig formalism. *The Journal of chemical physics* **143,** 243128 (2015).

98. Wang, Y., Noid, W. G., Liu, P. & Voth, G. A. Effective force coarse-graining. *Physical Chemistry Chemical Physics* **11,** 2002–2015 (2009).

99. Yoshimoto, Y. *et al.* Bottom-up construction of interaction models of non-Markovian dissipative particle dynamics. *Physical Review E* **88,** 043305 (2013).

100. Li, Z., Bian, X., Caswell, B. & Karniadakis, G. E. Construction of dissipative particle dynamics models for complex fluids via the Mori–Zwanzig formulation. *Soft Matter* **10,** 8659–8672 (2014).

101. Berne, B. J. & Pechukas, P. Gaussian model potentials for molecular interactions. *The Journal of Chemical Physics* **56,** 4213–4216 (1972).

102. Golubkov, P. A. & Ren, P. Generalized coarse-grained model based on point multipole and Gay-Berne potentials. *The Journal of chemical physics* **125,** 064103 (2006).

103. Tripathy, M., Agarwal, U. & Kumar, P. S. Toward Transferable Coarse-Grained Potentials for Poly-Aromatic Hydrocarbons: A Force Matching Approach. *Macromolecular Theory and Simulations* **28,** 1800040 (2019).

104. Tanis, I., Rousseau, B., Soulard, L. & Lemarchand, C. A. Assessment of an anisotropic coarse-grained model for cis-1, 4-polybutadiene: A bottom-up approach. *Soft Matter* **17,** 621–636 (2021).

105. Goujon, F. *et al.* Backbone oriented anisotropic coarse grains for efficient simulations of polymers. *The Journal of Chemical Physics* **153,** 214901 (2020).

106. Deng, M., Pan, W. & Karniadakis, G. E. Anisotropic single-particle dissipative particle dynamics model. *Journal of Computational Physics* **336,** 481–491 (2017).

107. Thompson, A. P. *et al.* LAMMPS-a flexible simulation tool for particle-based materials modeling at the atomic, meso, and continuum scales. *Computer Physics Communications* **271,** 108171 (2022).

108. Cleaver, D. J., Care, C. M., Allen, M. P. & Neal, M. P. Extension and generalization of the Gay-Berne potential. *Physical Review E* **54,** 559 (1996).

109. Kabadi, V. N. Molecular dynamics of fluids: the Gaussian overlap model II. *Berichte der Bunsengesellschaft für physikalische Chemie* **90,** 327–332 (1986).

110. Sagui, C., Pedersen, L. G. & Darden, T. A. Towards an accurate representation of electrostatics in classical force fields: Efficient implementation of multipolar interactions in biomolecular simulations. *The Journal of chemical physics* **120,** 73–87 (2004).

111. Applequist, J. Traceless cartesian tensor forms for spherical harmonic functions: new theorems and applications to electrostatics of dielectric media. *Journal of Physics A: Mathematical and General* **22,** 4303 (1989).

112. Stone, A. J. Electrostatic damping functions and the penetration energy. *The Journal of Physical Chemistry A* **115,** 7017–7027 (2011).

113. Kirkwood, J. G. The statistical mechanical theory of transport processes I. General theory. *The Journal of Chemical Physics* **14,** 180–201 (1946).

114. Brey, J. & Ordónez, J. G. Computer studies of Brownian motion in a Lennard-Jones fluid: The Stokes law. *The Journal of Chemical Physics* **76,** 3260–3263 (1982).

115. Pan, W., Caswell, B. & Karniadakis, G. E. Rheology, microstructure and migration in Brownian colloidal suspensions. *Langmuir* **26,** 133–142 (2010).

116. Souza, P. C. *et al.* Martini 3: a general purpose force field for coarse-grained molecular dynamics. *Nature methods* **18,** 382–388 (2021).

117. Alessandri, R. *et al.* Martini 3 Coarse-Grained Force Field: Small Molecules. *Advanced Theory and Simulations* **5,** 2100391 (2022).

118. Yoneya, M. Simulation of Crystallization of Pentacene and Its Derivatives from Solution. *The Journal of Physical Chemistry C* **125,** 2257–2263 (2021).

119. Tan, L., Davis, R. M., Myerson, A. S. & Trout, B. L. Control of heterogeneous nucleation via rationally designed biocompatible polymer surfaces with nanoscale features. *Crystal Growth & Design* **15,** 2176–2186 (2015).

120. Lemanowicz, M., Mielańczyk, A., Walica, T., Kotek, M. & Gierczycki, A. Application of Polymers as a Tool in Crystallization—A Review. *Polymers* **13,** 2695 (2021).

121. Ho, R.-M., Chiang, Y.-W., Lin, S.-C. & Chen, C.-K. Helical architectures from self-assembly of chiral polymers and block copolymers. *Progress in Polymer Science* **36,** 376–453 (2011).

122. Schwiebert, K. E., Chin, D. N., MacDonald, J. C. & Whitesides, G. M. Engineering the solid state with 2-benzimidazolones. *Journal of the American Chemical Society* **118,** 4018–4029 (1996).

123. Pardey, R. *et al.* Liquid crystal transition and crystallization kinetics in poly (ester imide) s. *Macromolecules* **27,** 5794–5802 (1994).

124. Rullyani, C., Sung, C.-F., Lin, H.-C. & Chu, C.-W. Flexible organic thin film transistors incorporating a biodegradable CO2-based polymer as the substrate and dielectric material. *Scientific reports* **8,** 8146 (2018).

125. Bi, S., He, Z., Chen, J. & Li, D. Solution-grown small-molecule organic semiconductor with enhanced crystal alignment and areal coverage for organic thin film transistors. *AIP Advances* **5,** 077170 (2015).

126. Ikeda, S. Molecular dynamics simulations of pentacene thin film growth: Stability of nuclei comprising standing molecules and their subsequent growth. *Applied Physics Express* **13,** 015508 (2019).

127. Everaers, R. & Ejtehadi, M. Interaction potentials for soft and hard ellipsoids. *Physical Review E* **67,** 041710 (2003).

128. Schmid, N. *et al.* Definition and testing of the GROMOS force-field versions 54A7 and 54B7. *European biophysics journal* **40,** 843–856 (2011).

129. Allen, M. P. & Tildesley, D. J. *Computer simulation of liquids* (Oxford university press, 2017).

130. Liashenko, I., Rosell-Llompart, J. & Cabot, A. Ultrafast 3D printing with submicrometer features using electrostatic jet deflection. *Nature communications* **11,** 753 (2020).

131. Zhang, B., He, J., Li, X., Xu, F. & Li, D. Micro/nanoscale electrohydrodynamic printing: From 2D to 3D. *Nanoscale* **8,** 15376–15388 (2016).

132. Sola, A., Trinchi, A. & Hill, A. J. Self-assembly meets additive manufacturing: Bridging the gap between nanoscale arrangement of matter and macroscale fabrication. *Smart Materials in Manufacturing* **1,** 100013 (2023).

133. Engstrom, D. S., Porter, B., Pacios, M. & Bhaskaran, H. Additive nanomanufacturing A review. *Journal of Materials Research* **29,** 1792–1816 (2014).

134. Sui, X., Downing, J. R., Hersam, M. C. & Chen, J. Additive manufacturing and applications of nanomaterial-based sensors. *Materials Today* **48,** 135–154 (2021).

135. Ruan, X. *et al.* Emerging applications of additive manufacturing in biosensors and bioanalytical devices. *Advanced Materials Technologies* **5,** 2000171 (2020).

136. Ahmed, A. *et al.* Toward High-Performance Triboelectric Nanogenerators by Engineering Interfaces at the Nanoscale: Looking into the Future Research Roadmap. *Advanced Materials Technologies* **5,** 2000520 (2020).

137. Sahu, M. *et al.* Additive manufacturing-based recycling of laboratory waste into energy harvesting device for self-powered applications. *Nano Energy* **88,** 106255 (2021).

138. Wang, Y., Gao, M., Wang, D., Sun, L. & Webster, T. J. Nanoscale 3D bioprinting for osseous tissue manufacturing. *International Journal of Nanomedicine,* 215–226 (2020).

139. Islam, M., Lantada, A. D., Mager, D. & Korvink, J. G. Carbon-Based Materials for Articular Tissue Engineering: From Innovative Scaffolding Materials toward Engineered Living Carbon. *Advanced Healthcare Materials* **11,** 2101834 (2022).

140. Smith, J. A. & Mele, E. Electrospinning and additive manufacturing: Adding three-dimensionality to electrospun scaffolds for tissue engineering. *Frontiers in Bioengineering and Biotechnology,* 1238 (2021).

141. Altissimo, M. E-beam lithography for micro-/nanofabrication. *Biomicrofluidics* **4,** 026503 (2010).

142. Hahn, V. *et al.* Rapid assembly of small materials building blocks (voxels) into large functional 3D metamaterials. *Advanced Functional Materials* **30,** 1907795 (2020).

143. Rocha, V. G., Saiz, E., Tirichenko, I. S. & Garcıa-Tuñón, E. Direct ink writing advances in multi-material structures for a sustainable future. *Journal of Materials Chemistry A* **8,** 15646–15657 (2020).

144. Sadaf, A. *et al.* Wall Microstructures of High Aspect Ratio Enabled by Near-Field Electrospinning. *Advanced Engineering Materials* **24,** 2101740 (2022).

145. Reneker, D. H. & Yarin, A. L. Electrospinning jets and polymer nanofibers. *Polymer* **49,** 2387–2425 (2008).

146. Xue, J., Wu, T., Dai, Y. & Xia, Y. Electrospinning and electrospun nanofibers: Methods, materials, and applications. *Chemical reviews* **119,** 5298–5415 (2019).

147. Yarin, A. L., Koombhongse, S. & Reneker, D. H. Taylor cone and jetting from liquid droplets in electrospinning of nanofibers. *Journal of applied physics* **90,** 4836–4846 (2001).

148. Reneker, D. H., Yarin, A. L., Fong, H. & Koombhongse, S. Bending instability of electrically charged liquid jets of polymer solutions in electrospinning. *Journal of Applied physics* **87,** 4531–4547 (2000).

149. Sun, D., Chang, C., Li, S. & Lin, L. Near-field electrospinning. *Nano letters* **6,** 839–842 (2006).

150. He, X.-X. *et al.* Near-field electrospinning: progress and applications. *The Journal of Physical Chemistry C* **121,** 8663–8678 (2017).

151. Park, J.-U. *et al.* High-resolution electrohydrodynamic jet printing. *Nature materials* **6,** 782–789 (2007).

152. Bisht, G. S. *et al.* Controlled continuous patterning of polymeric nanofibers on three-dimensional substrates using low-voltage near-field electrospinning. *Nano letters* **11,** 1831–1837 (2011).

153. Deng, J., Liu, C. & Madou, M. Ultra-thin carbon nanofibers based on graphitization of near-field electrospun polyacrylonitrile. *Nanoscale* **12,** 10521–10531 (2020).

154. George, D. *et al.* Fabrication of patterned graphitized carbon wires using low voltage near-field electrospinning, pyrolysis, electrodeposition, and chemical vapor deposition. *Microsystems & nanoengineering* **6,** 7 (2020).

155. Ruggieri, F. *et al.* Preparation of nitrogen doped TiO2 nanofibers by near field electrospinning (NFES) technique for NO2 sensing. *Sensors and Actuators B: Chemical* **179,** 107–113 (2013).

156. Lou, Z., Yang, X., Chen, H. & Liang, Z. Flexible ultraviolet photodetectors based on ZnO–SnO2 heterojunction nanowire arrays. *Journal of Semiconductors* **39,** 024002 (2018).

157. Luo, G. *et al.* Direct-write, self-aligned electrospinning on paper for controllable fabrication of three-dimensional structures. *ACS applied materials & interfaces* **7,** 27765–27770 (2015).

158. Zheng, G. *et al.* Precision deposition of a nanofibre by near-field electrospinning. *Journal of Physics D: Applied Physics* **43,** 415501 (2010).

159. Zheng, G. *et al.* High-aspect-ratio three-dimensional electrospinning via a tip guiding electrode. *Materials & Design* **198,** 109304 (2021).

160. Alison, J. & Hill, R. A model for bipolar charge transport, trapping and recombination in degassed crosslinked polyethene. *Journal of Physics D: Applied Physics* **27,** 1291 (1994).

161. Al-Dhahir, I. *et al.* Electrostatic Tuning of Ionic Charge in SiO2 Dielectric Thin Films. *ECS Journal of Solid State Science and Technology* **11,** 063010 (2022).

162. Le Roy, S. & Hoang, M. A bipolar charge transport model to simulate the impact of nanometric scale processes on the space charge behaviour in polyethylene. *Journal of Physics D: Applied Physics* **55,** 465303 (2022).

163. Boufayed, F. *et al.* Models of bipolar charge transport in polyethylene. *Journal of applied physics* **100,** 104105 (2006).

164. Cai, X., Lin, X., Yu, J. & Lu, Z. Modeling of space charge dynamics in polyethylene under AC stress based on bipolar charge transport model. *Materials Research Express* **7,** 115305 (2020).

165. Thyssen, A., Almdal, K. & Thomsen, E. V. Electret stability related to the crystallinity in polypropylene. *IEEE Transactions on Dielectrics and Electrical Insulation* **24,** 3038–3046 (2017).

166. Mishra, A. Studies of polymer electrets. II. Factors governing the stabilities of homoelectrets obtained from polystyrene and its derivatives. *Journal of Applied Polymer Science* **27,** 1107–1118 (1982).

167. Mohmeyer, N. *et al.* Additives to improve the electret properties of isotactic polypropylene. *Polymer* **48,** 1612–1619 (2007).

168. Kaminow, I. P., Li, T. & Willner, A. E. *Optical fiber telecommunications VB: systems and networks* (Elsevier, 2010).

169. Khilo, A. *et al.* Photonic ADC: overcoming the bottleneck of electronic jitter. *Optics Express* **20,** 4454–4469 (2012).

170. Weimann, C., Lauermann, M., Hoeller, F., Freude, W. & Koos, C. Silicon photonic integrated circuit for fast and precise dual-comb distance metrology. *Optics express* **25,** 30091–30104 (2017).

171. Li, M. *et al.* Poling efficiency enhancement of tethered binary nonlinear optical chromophores for achieving an ultrahigh n 3 r 33 figure-of-merit of 2601 pm V- 1. *Journal of Materials Chemistry C* **3,** 6737–6744 (2015).

172. Zou, J., Zhang, D., Chen, W. & Luo, J. Optimizing the vectorial component of first hyperpolarizabilities of push–pull chromophores to boost the electro-optic activities of poled polymers over broad telecom wavelength bands. *Materials Advances* **2,** 2318–2327 (2021).

173. Koeber, S. *et al.* Femtojoule electro-optic modulation using a silicon–organic hybrid device. *Light: Science & Applications* **4,** e255–e255 (2015).

174. Malde, A. K. *et al.* An automated force field topology builder (ATB) and repository: version 1.0. *Journal of chemical theory and computation* **7,** 4026–4037 (2011).

175. Martınez, L., Andrade, R., Birgin, E. G. & Martınez, J. M. PACKMOL: A package for building initial configurations for molecular dynamics simulations. *Journal of computational chemistry* **30,** 2157–2164 (2009).

176. Kieninger, C. *et al.* Ultra-high electro-optic activity demonstrated in a silicon-organic hybrid modulator. *Optica* **5,** 739–748 (2018).

177. Ricci, M., Roscioni, O. M., Querciagrossa, L. & Zannoni, C. MOLC. A reversible coarse grained approach using anisotropic beads for the modelling of organic functional materials. *Physical Chemistry Chemical Physics* **21,** 26195–26211 (2019).

178. Wang, J. *et al.* Machine learning of coarse-grained molecular dynamics force fields. *ACS central science* **5,** 755–767 (2019).

A. Appendix

A.1. Range and strength parameter in Gay-Berne functional

The range parameter $\sigma(\mathbf{e}_{IJ}, \mathbf{u}_I, \mathbf{u}_J)$ is given by

$$\sigma(\mathbf{e}_{IJ}, \mathbf{u}_I, \mathbf{u}_J) = \sigma_0 [\{ \frac{\chi\alpha^2(\mathbf{u}_I \cdot \mathbf{e}_{IJ}) + \chi\alpha^{-2}(\mathbf{u}_J \cdot \mathbf{e}_{IJ}) - 2\chi^2(\mathbf{u}_I \cdot \mathbf{e}_{IJ})(\mathbf{u}_J \cdot \mathbf{e}_{IJ})(\mathbf{u}_I \cdot \mathbf{u}_I)}{1 - \chi^2(\mathbf{u}_I \cdot \mathbf{u}_I)^2} \}]^{-\frac{1}{2}}, \tag{A.1}$$

where

$$\sigma_0 = \sqrt{d_I^2 + d_J^2}, \tag{A.2}$$

$$\chi = [\frac{(l_I^2 - d_I^2)(l_J^2 - d_J^2)}{(l_I^2 + d_I^2)(l_J^2 + d_J^2)}]^{\frac{1}{2}}, \tag{A.3}$$

$$\alpha^2 = [\frac{(l_I^2 - d_I^2)(l_J^2 + d_I^2)}{(l_J^2 - d_J^2)(l_I^2 + d_J^2)}]^{\frac{1}{2}}, \tag{A.4}$$

and l and d denote the length and breadth of the GB particles, respectively, and $\chi\alpha^2$, $\chi\alpha^{-2}$ and χ^2 are given by

$$\chi\alpha^2 = \frac{(l_I^2 - d_I^2)}{(l_I^2 + d_J^2)}, \tag{A.5}$$

$$\chi\alpha^{-2} = \frac{(l_J^2 - d_J^2)}{(l_J^2 + d_I^2)}, \tag{A.6}$$

$$\chi^2 = [\frac{(l_I^2 - d_I^2)(l_J^2 - d_J^2)}{(l_I^2 + d_I^2)(l_J^2 + d_J^2)}], \tag{A.7}$$

The strength parameter $\epsilon(\mathbf{e}_{IJ}, \mathbf{u}_I, \mathbf{u}_J)$ is given by

$$\epsilon(\mathbf{e}_{IJ}, \mathbf{u}_I, \mathbf{u}_J) = \epsilon_0 \epsilon_1^{\nu}(\mathbf{u}_I, \mathbf{u}_J)\epsilon_2^{\mu}(\mathbf{e}_{IJ}, \mathbf{u}_I, \mathbf{u}_J), \tag{A.8}$$

where ϵ_1 and ϵ_2 are defined as

$$\epsilon_1(\mathbf{u}_I, \mathbf{u}_J) = [1 - \chi^2(\mathbf{u}_I, \mathbf{u}_J)^2]^{-\frac{\nu}{2}}, \tag{A.9}$$

$$\epsilon_2(\mathbf{e}_{IJ}, \mathbf{u}_I, \mathbf{u}_J) = 1 - \{\frac{\chi'\alpha'^2(\mathbf{u}_I \cdot \mathbf{e}_{IJ}) + \chi'\alpha'^{-2}(\mathbf{u}_J \cdot \mathbf{e}_{IJ}) - 2\chi'^2(\mathbf{u}_I \cdot \mathbf{e}_{IJ})(\mathbf{u}_J \cdot \mathbf{e}_{IJ})(\mathbf{u}_I \cdot \mathbf{u}_J)}{1 - \chi'^2(\mathbf{u}_I \cdot \mathbf{u}_J)^2}\}, \tag{A.10}$$

denote that

$$\chi' = [\frac{((\epsilon_{SI}^{1/\mu} - \epsilon_{FI}^{1/\mu})) \times (\epsilon_{SJ}^{1/\mu} + \epsilon_{FI}^{1/\mu}))}{((\epsilon_{SJ}^{1/\mu} - \epsilon_{FJ}^{1/\mu})) \times (\epsilon_{SI}^{1/\mu} + \epsilon_{FJ}^{1/\mu})}]^{\frac{1}{2}}, \tag{A.11}$$

$$\alpha'^2 = [\frac{((\epsilon_{SI}^{1/\mu} - \epsilon_{FI}^{1/\mu})) \times (\epsilon_{SJ}^{1/\mu} - \epsilon_{FJ}^{1/\mu}))}{((\epsilon_{SJ}^{1/\mu} + \epsilon_{FI}^{1/\mu})) \times (\epsilon_{SI}^{1/\mu} + \epsilon_{FJ}^{1/\mu})}]^{\frac{1}{2}}, \tag{A.12}$$

where ϵ_F is the well-depth of face-to-face configuration, and ϵ_S is the well-depth of side-to-side configuration. The parameters ν and μ are set to 1.0 and 2.0, respectively. And $\chi'\alpha'^2$, $\chi'\alpha'^{-2}$ and χ'^2 are given by

$$\chi'\alpha'^2 = \frac{(\epsilon_{SI}^{1/\mu} - \epsilon_{FI}^{1/\mu})}{((\epsilon_{SI}^{1/\mu} + \epsilon_{FJ}^{1/\mu})}, \tag{A.13}$$

$$\chi'\alpha'^{-2} = \frac{(\epsilon_{SJ}^{1/\mu} - \epsilon_{FJ}^{1/\mu})}{((\epsilon_{SJ}^{1/\mu} + \epsilon_{FI}^{1/\mu})}, \tag{A.14}$$

$$\chi'^2 = [\frac{((\epsilon_{SI}^{1/\mu} - \epsilon_{FI}^{1/\mu})) \times (\epsilon_{SJ}^{1/\mu} + \epsilon_{FI}^{1/\mu}))}{((\epsilon_{SJ}^{1/\mu} - \epsilon_{FJ}^{1/\mu})) \times (\epsilon_{SI}^{1/\mu} + \epsilon_{FJ}^{1/\mu})}]. \tag{A.15}$$

A.2. Components of frictional coefficient

The components of the frictional tensor are given by

$$\begin{aligned}\varphi_{IJ}^R = \Delta((|\mathbf{u}_I \cdot \mathbf{u}_J|^2 - 1)|\mathbf{\Phi}_{IJ}^R| + (|\mathbf{e}_{IJ} \cdot \mathbf{u}_I| - |\mathbf{u}_I \cdot \mathbf{u}_J||\mathbf{e}_{IJ} \cdot \mathbf{u}_J|)|\mathbf{\Phi}_{IJ}^{u_I}| \\ + (|\mathbf{e}_{IJ} \cdot \mathbf{u}_J| - |\mathbf{e}_{IJ} \cdot \mathbf{u}_I||\mathbf{u}_I \cdot \mathbf{u}_J|)|\mathbf{\Phi}_{IJ}^{u_J}|)),\end{aligned} \tag{A.16}$$

$$\varphi_{IJ}^{u_J} = \Delta((|\mathbf{e}_{IJ}\cdot\mathbf{u}_I| - |\mathbf{u}_I\cdot\mathbf{u}_J||\mathbf{e}_{IJ}\cdot\mathbf{u}_J|)|\mathbf{\Phi}_{IJ}^{R}| + (|\mathbf{e}_{IJ}\cdot\mathbf{u}_J|^2 - 1)|\mathbf{\Phi}_{IJ}^{u_I}| + (|\mathbf{u}_I\cdot\mathbf{u}_J| - |\mathbf{e}_{IJ}\cdot\mathbf{u}_I||\mathbf{e}_{IJ}\cdot\mathbf{u}_J|)|\mathbf{\Phi}_{IJ}^{u_J}|), \tag{A.17}$$

$$\varphi_{IJ}^{u_J} = \Delta((|\mathbf{e}_{IJ}\cdot\mathbf{u}_J| - |\mathbf{e}_{IJ}\cdot\mathbf{u}_I||\mathbf{u}_I\cdot\mathbf{u}_J|)|\mathbf{\Phi}_{IJ}^{R}| + (|\mathbf{u}_I\cdot\mathbf{u}_J| - |\mathbf{e}_{IJ}\cdot\mathbf{u}_I||\mathbf{e}_{IJ}\cdot\mathbf{u}_J|)|\mathbf{\Phi}_{IJ}^{u_I}| + (|\mathbf{e}_{IJ}\cdot\mathbf{u}_I|^2 - 1)|\mathbf{\Phi}_{IJ}^{u_J}|), \tag{A.18}$$

where $\Delta = -1/(1-|\mathbf{e}_{IJ}\cdot\mathbf{u}_I|^2-|\mathbf{e}_{IJ}\cdot\mathbf{u}_J|^2-|\mathbf{u}_I\cdot\mathbf{u}_J|^2+2|\mathbf{e}_{IJ}\cdot\mathbf{u}_I||\mathbf{e}_{IJ}\cdot\mathbf{u}_J||\mathbf{u}_I\cdot\mathbf{u}_J|)$.

A.3. Parameters for benzene in AMZDPD model

Table A.1.: Optimized parameters for benzene in the AMZDPD model

Force	Parameter	Value
Electric Multipole	a	0.49
	α	170
	β	0.710
	Q_{pp}	4.584
	Q_{zz}	-9.169
Gay-Berne	d_w	0.922
	l	2.288
	d	4.309
	ϵ_0	1.191
	ϵ_F/ϵ_S	2.675
Frictional kernel	d_w	0.384
	l	3.767
	d	4.493
	ϵ_0	1.550
	ϵ_F/ϵ_S	0.479

A.4. Parameters for pentacene in AMZDPD model

Table A.2.: Optimized parameters for pentacene molecules in the AMZDPD model

Force	Parameter	Value
Gay-Berne	ϵ	2.322
	σ	8.072
	γ	1.000
	L_a	2.784
	L_b	5.708
	L_c	1.596
	ϵ_a	1.097
	ϵ_b	0.060
	ϵ_c	3.617
Quadrupole	Q_{aa}	5.59
	Q_{bb}	7.34
	Q_{cc}	-12.93
Frictional kernel	ϵ	2.553
	σ	8.072
	γ	1.000
	L_a	2.784
	L_b	5.708
	L_c	1.596
	ϵ_a	1.888
	ϵ_b	0.260
	ϵ_c	3.607

A.5. Parameters of charge transport model for electrospinning

Table A.3.: The parameters of the charge transport model

Physical meaning	Parameter	Value
Distance	L	300μm
Voltage	Φ	187.5V
Height of the fiber	h	2μm
Charge constant	ρ_0	$1\times10^{12}\ \mu m^{-1}$
Width of the Gaussian	w	0.5μm
Standard deviation of the Gaussian	σ	0.2μm
Charge mobility in PEO	μ	$1\times10^{-5} cm^2V^{-2}s^{-1}$
Charge diffusivity in PEO	D	$5cm^2s^{-1}$
Permittivity of PEO	ϵ_{peo}	5
Transfer rate from mobile to trapped state	$R_{f\rightarrow t}$	$2\times10^{-3}\ ms^{-1}$
Transfer rate from trapped to mobile state	$R_{t\rightarrow f}$	$2\times10^{-3}\ ms^{-1}$
Density of the trapped state	N_t	$1\times10^{12}\ \mu m^{-1}$

List of publications

1. **Chan, K.C.**, Li, Z. & Wenzel, W. A Mori–Zwanzig Dissipative Particle Dynamics Approach for Anisotropic Coarse Grained Molecular Dynamics. *Journal of Chemical Theory and Computation* 19, 3, 910–923 (2023).
2. Eggeler, Y.M., **Chan, K.C.**, Sun, Q., Lantada, A.D., Mager, D., Schwaiger, R., Gumbsch, P., Schröder, R., Wenzel, W., Korvink, J.G. & Islam, M. A review on 3D architected pyrolytic carbon produced by additive micro/nanomanufacturing. (Submitted in *Advanced Functional Materials*)
3. Begum, S., Kutonova, K., Mauri, A., König-Edel, M., **Chan, K.C.**, Sprau, C., Dolle, C., Leonhard, T., Heißler, S., Eggeler, Y.M., Wenzel, W. , Kozlowska, M. & Bräse, S. Disulfide-bridged Dynamic Covalent Triazine Polymer Thin Films by Interface Polymerization. (Submitted in *Advanced Functional Materials*)
4. **Chan, K.C.**, Sadaf, A., Korvink, J.G. & Wenzel, W. Electromechanical analysis of electrospinning polymer fiber deposition. (In preparation)

Acknowledgements

I would like to express my deepest appreciation to my supervisor, Prof. Wolfgang Wenzel, for supervising and giving me the opportunity to work on these interesting projects. He does not only give me a lot of useful advice and suggestions, but also allow me to follow my own ideas. I would also express many thanks to Prof. Jörg Schmalian for being the second referee of this thesis and to Prof. Carsten Rockstuhl for being my second adviser.

Furthermore, I would like to deeply thank my collaborators for the experimental data and technical support, and especially to Dr. Zhen Li for his support in the AMZDPD model development.

I want to thank all my colleagues in the group during my phd period, especially to my office-mate Mersad Mostaghimi, and also to Modan Liu, Meysam Esmaeilpour, Mariana Kozlowska, Yohanes Pramudya, Anna Mauri, Srdan Pusara, Helmy Pacheco Hernández, Niklas Kappel, Deniz Özdemir ,Bahareh Bamdad, and more... for the great working atmosphere, interesting discussions, and both scientific and non-scientific support.

Last but not least, I would like to thank all my friends for their support. Also, I am very grateful to my family for their unlimited support and encouragement during all stages of my life. Finally, I would like to give a special thank to my girlfriend, Wenqing, for encouraging me and cooking numerous delicious food over the years.